NATIONAL TECHNICAL UNIVERSITY OF ATHENS, GREECE

Development of a novel active camber angle control system applied on prototype electric vehicle

24/07/2020

A thesis submitted in partial satisfaction of the
requirements for the degree
Master of Science

in

Automation Systems

by

Ioannis N. Tzortzis

Committee in charge:

Professor George Papalambrou
Professor Konstantinos Kyriakopoulos
Professor Evangelos Papadopoulos

"...niégame el pan, el aire, la luz, la primavera,
pero tu risa nunca porpue me moriría."

Pablo Neruda

List of Symbols		
Symbol	Description	Units
α_y	Lateral acceleration	g's
α	Tyre slip angle	rads
δ_F	Front wheel steering angle	rad
β	Vehicle body slip angle	rads
ΣM_A	The summation of the moments around point A	-
v	Vehicle body velocity vector	m/s
v_x	Vehicle longitudinal velocity	m/s
v_y	Vehicle lateral velocity	m/s
ψ	Vehicle yaw angle	rad
r	Vehicle yaw angle	rad
ϕ	Vehicle roll angle	rad
γ	Camber angle	rad
γ_g	Camber angle with respect to the ground	rad
γ_b	Camber angle with respect to the vehicle body	rad
$\dot{\psi}$	Vehicle yaw rate	rad/s
α_f	Front wheel slip angle	rad
α_r	Rear wheel slip angle	rad
$C_{\alpha f}$	Front wheel conering stiffness	N/rad
$C_{\alpha r}$	Rear wheel conering stiffness	N/rad
C_γ	Camber stiffness	N/rad
F_{yf}	Front tyre lateral force	N
F_{yr}	Rear tyre lateral force	N
L	Vehicle wheel base	m
L_f	Distance between front axle and COG	m
L_r	Distance between rear axle and COG	m
W	Vehicle weight	$kg\frac{m}{s^2}$
W_f	Weight of vehicle front axle	kg
W_r	Weight of vehicle rear axle	kg
T_f	Front axle track width	m
T_r	Rear axle track width	m
T_{ls}	Distance between vehicle left side and COG	m
T_{rs}	Distance between vehicle right side and COG	m
h_{COG}	Height of COG	m
R	Radius of vehicle wheels	m
m	Vehicle mass	kg
x	Longitudinal movement axis	-
y	Lateral movement axis	-
z	Vertical movement axis	-

List of Symbols		
Symbol	Description	Units
I_z	Yaw moment of inertia	kg m2
I_ϕ	Roll moment of inertia	kg m2
C_ϕ	Roll damping coefficient	-
$K_{\phi s}$	Roll stiffness	-
F_f	Ground reaction of front axle	N
F_r	Ground reaction of rear axle	N
F_{ls}	Ground reaction of left side	N
F_{rs}	Ground reaction of right side	N
F_r	Ground reaction of rear axle	N

List of Abbreviations	
Abbreviation	Description
ECU	Electronic Control Unit
CCM	Central Control Module
BCM	Body Control Module
CCS	Camber Control System
COG	Center Of Gravity
IMU	Inertial Measurement Unit
DRS	Drag Reduction System
FIA	Federation Internationale de l'Automobile

List of Figures

1 Line Departure Warning (LDW) System [9] . . . 2
2 Yaw Stability Control system [9] . . . 3
3 Porsche 911 GT3 . . . 4
4 Three dimensional coordinate system . . . 6
5 Tyre force and moment nomenclature Z-UP [4] . . . 7
6 Two common types of dependent suspension systems . . . 8
7 Common types of independent suspension systems . . . 9
8 Lateral force vs slip angle for a racing tyre [14] . . . 10
9 Camber thrust and camber roll-off at constant load [14] . . . 10
10 Total camber angle of the wheel with respect to the ground . . . 11
11 Negative camber configuration . . . 11
12 Positive camber configuration . . . 12
13 Neutral camber configuration . . . 12
14 Computational results [15] . . . 14
15 The prototype vehicles used for the experiments of research [15] . . . 15
16 Experimentation results of the research [15] . . . 15
17 Camber angle adjustment mechanism proposed in publication [1] . . . 16
18 Camber angle adjustment mechanism proposed in publication [1] . . . 17
19 Camber angle adjustment mechanism proposed in publication [1] . . . 17
20 Camber angle adjustment mechanism proposed in publication [1] . . . 18
21 Camber angle adjustment mechanism proposed in publication [1] . . . 18
22 Camber angle adjustment mechanism proposed in publication [5] . . . 19
23 Camber angle response of prototype [5] . . . 19
24 The prototype vehicle modules . . . 20
25 Specifying the longitudinal position of COG . . . 21
26 Specifying the lateral position of COG . . . 22
27 Specifying the height of COG . . . 23
28 The electronics structure . . . 25
29 Raspberry pi 3 model B+ - The Central Control Module (CCM) . . . 26
30 Arduino Mega 2560 Rev3 - The Body Control Module (CCM) . . . 27
32 . . . 29
33 . . . 29
34 The electronics schematic . . . 30
35 Front view - The default suspension system of the vehicle . . . 31
36 Top view - The default suspension system of the vehicle . . . 32
37 Negative camber angle configuration . . . 33
38 Front view of the camber angle control prototype mechanism . . . 34
39 Top view of the camber angle control prototype mechanism . . . 34
40 Front view - Analysis of the mechanism geometry . . . 35
41 The relation between servo angle and the wheel camber angle with respect to the vehicle body. . . . 35
42 The flowchart of the system algorithm . . . 36
43 The single track model - Bicycle model . . . 37

44 Successive circular maneuvers experiment 39
45 Successive circular maneuvers experiment - Vechicle movement 40
46 Comparison: experimental/simulated yaw rate 41
47 Sinusoidal maneuver experiment 42
48 Comparison: experimental/simulated yaw rate 43
49 Top view - The steering system structure 44
50 Relation between the steering servo angle and the wheel steering angle . . . 45
51 The Simulink model of the proposed system 46
52 The camber controller block 46
53 Simulated sinusoidal steering maneuver - CCS servo command and position signals 47
54 Simulated counterclockwise maneuver 48
55 Simulated clockwise maneuver 49
56 Simulated sinusoidal steering maneuver 50
57 Left circular maneuver 51
58 Right circular maneuver 52
59 Sinusoidal steering maneuver 53
60 Left circular maneuver - Vehicle movement 54
61 Left circular maneuver - Camber control signals 55
62 Clockwise circular maneuver - Vehicle dynamics 56
63 Clockwise circular maneuver - Camber control signals 57
64 Sinusoidal maneuver (scaling factor 1.2) - Vehicle dynamics 58
65 Sinusoidal maneuver (scaling factor 1.2) - Camber control signals 59
66 Sinusoidal maneuver (scaling factor 1.4) - Vehicle dynamics 60
67 Sinusoidal maneuver (scaling factor 1.4) - Camber control signals 61
68 Left circular maneuver - Comparison CCS enbled - CCS disabled 62
69 Right circular maneuver - Comparison CCS enbled - CCS disabled 63
70 CCS control signals - Scaling factor 0.0 66
71 CCS control signals - Scaling factor 0.0 67
72 Counterclockwise circular maneuver simulation - Vehicle movement 68
73 Counterclockwise circular maneuver simulation - CCS control signals 69
74 Clockwise circular maneuver simulation - Vehicle movement 70
75 Clockwise circular maneuver simulation - CCS control signals 71
76 Sinusoidal steering maneuver simulation - Vehicle movement 72
77 Clockwise circular maneuver simulation - CCS control signals 73
78 Side view of the CCS mechanism 74
79 Rear view of the CCS mechanism 75
80 Top view of the CCS mechanism 75
81 Preparation of the vehicle wiring harness 76
82 CCS configuration before testing 76
83 The prototype vehicle before testing 77

Contents

1 Introduction **1**
- 1.1 Lane Departure Warning (LDW) system . . . 1
- 1.2 Yaw Stability Control system . . . 1
- 1.3 Rear-axle steering . . . 2
- 1.4 Drag reduction system . . . 3
- 1.5 The objective . . . 3

2 Literature study **5**
- 2.1 Lumped mass . . . 5
- 2.2 Coordinate system . . . 5
- 2.3 Tyres forces . . . 5
- 2.4 Suspension systems . . . 7
  - 2.4.1 Dependent suspension . . . 7
  - 2.4.2 Independent suspension . . . 8
- 2.5 Camber angle definition . . . 8
- 2.6 Negative camber angle configuration . . . 9
- 2.7 Study on the effects of camber control on vehicle dynamics . . . 13
- 2.8 Prototype hydraylic mechanism for camber angle adjustment . . . 15
- 2.9 Wheel suspension with automatic camber adjustment . . . 15
- 2.10 Active camber and toe control strategy for the double wishbone suspension system . . . 17

3 The proposed system **20**
- 3.1 The prototype vehicle . . . 20
- 3.2 Specifying the position of vehicle's center of gravity . . . 21
  - 3.2.1 The COG longitudinal position . . . 21
  - 3.2.2 The COG lateral position . . . 22
  - 3.2.3 The COG height from the ground . . . 23
- 3.3 The vehicle electronics . . . 25
  - 3.3.1 The electronics structure . . . 25
  - 3.3.2 The primary ECU - Central Control Module (CCM) . . . 26
  - 3.3.3 The secondary ECU - Body Control Module (BCM) . . . 26
  - 3.3.4 The vehicle Inertial Measerement Unit(IMU) . . . 27
  - 3.3.5 The vehicle electric motor . . . 27
  - 3.3.6 The electric motor controller . . . 28
  - 3.3.7 The step down DC-DC converter . . . 28
  - 3.3.8 The servo mechanism . . . 28
  - 3.3.9 The vehicle longitudinal velocity sensor . . . 29
  - 3.3.10 The electronics schematic . . . 29
- 3.4 The camber angle control mechanism . . . 31
  - 3.4.1 The vehicle suspension system . . . 31
  - 3.4.2 An alternative suspension system configuration . . . 31
  - 3.4.3 The proposed mechanism . . . 32

3.4.4 Calculating the camber angle mechanism ratio . . . 32
3.5 The control algorithm . . . 36
3.6 The vehicle model . . . 37
3.6.1 The linear single track model . . . 37
3.6.2 The validation of the model . . . 39
3.6.3 Calculating the steering system ratio . . . 44
3.7 The Matlab/Simulink model . . . 46

4 Experimental results **51**
4.1 Experimentation with CCS disabled . . . 51
4.1.1 Counterclockwise circular maneuver with ccs disabled . . . 51
4.1.2 Clockwise circular maneuver with ccs disabled . . . 52
4.1.3 Sinusoidal steering maneuver - CCS disabled . . . 53
4.2 Experimentation with CCS enabled . . . 54
4.2.1 Counterclockwise circular maneuver with CCS enabled . . . 54
4.2.2 Clockwise circular maneuver with CCS enabled . . . 56
4.2.3 Sinusoidal steering maneuver 1 with CCS enabled . . . 58
4.2.4 Sinusoidal steering maneuver 2 with CCS enabled . . . 60
4.3 Comparison . . . 62

5 Conclusion **64**

6 Appendix **66**
6.1 Simulation results . . . 66
6.2 Prototype vehicle assembly . . . 74

Acknowledgements

I would like to express my gratitude to some people who contributed to this work in various ways. I would like to thank

My supervisor Prof. George Papalambrou for his guidance and our flawless collaboration through the developement of this study.

The members of the commitee in charge, Prof. Konstantinos Kyriakopoulos and Prof. Evangelos Papadopoulos, for reviewing and evaluating this thesis.

My parents, Nikos and Maria, for their overall support, guidance and patience through life.

My siblings, George, Athena, Manos and their families including Maria, Nikos and Marilena for their help and support.

My closest relatives and friends for their loyalty in life and their faith in my potentials.

Abstract

In this thesis, the design and the development of a novel camber angle control system (CCS), applied on an electric prototype vehicle, is presented. The vehicle has a simple indepedent suspension structure. Thus, each wheel is attached to the vehicle body through an upper and a lower arm. After the installation of the CCS mechanism, the upper arms of the front wheels could be translated horizontally, adjusting the camber angle of the front wheels. The Body Control Module (BCM) collects data from the several vehicle sensors, applies appropriate filters and sends essential information to the Central Control Module (CCM) of the vehicle. In the CCM, the major controller of the system is being excecuted. The controller reads the yaw rate and according to its current value, the desired camber angle is being calculated. The value of the desired camber angle is being forwarded to the CCS servo through the BCM. Conforming to the theory, the proper camber angle adjustment could cause higher lateral forces. Accordingly, an increase to lateral acceleration should occur. Based on that hypothesis, simple circular maneuvers with constant longitudinal velocity and steering angle were designed for the mathematical proof of concept. In addition, a sinusoidal steering maneuver was designed as experiment for a more qualitative validation of the hypothesis.

1 Introduction

Nowadays, the cars are being designed and developed in a more sophisticated way from the perspective of safety and optimized driving quality. The exponential technological development has introduced a plethora of automations in the automotive industry. Several active mechatronic systems has been proposed and developed for automotive applications, from ostensibly simple ones like the Lane Departure Warning (LDW) system, to more complicated like Yaw Stability Control systems [9], four wheel steering systems, etc.

Generally, electronic systems function to control, measure, or communicate [10]. The major categories of automotive electronic systems include

1. Engine/power train control
2. Ride/handling control
3. Cruise control
4. Braking/traction control
5. Instrumentation (instrument panel)
6. Power steering control
7. Occupant protection
8. Entertainment
9. Comfort control
10. Cellular phones

1.1 Lane Departure Warning (LDW) system

The lane departure warning (LDW) system uses a camera to monitor the vehicle position with respect to the road lanes (Figure 1). When the vehicle is about to leave the recognized lane, a warning is provided to the driver. A commercial product of this system has been developed by Iteris Inc and it is called AutoVue. Using image recognition software the computer of the AutoVue unit can predict when the vehicle drifts towards an unintented lane change and emits a specific sound, alerting the driver for the situation.

1.2 Yaw Stability Control system

The response of the vehicle on the driver inputs could be different in relation with the friction provided by the road surface. A wet road with low friction coefficient could make a vehicle follow a trajectory with larger radius than the desired one (upper curve in Figure 2). The same result could be occured on a dry road, if the driver accelerates the vehicle in high speed. On the other hand, a dry road with high friction coefficient in combination with normal driver inputs, could provide high lateral force that keep the vehicle in the desired

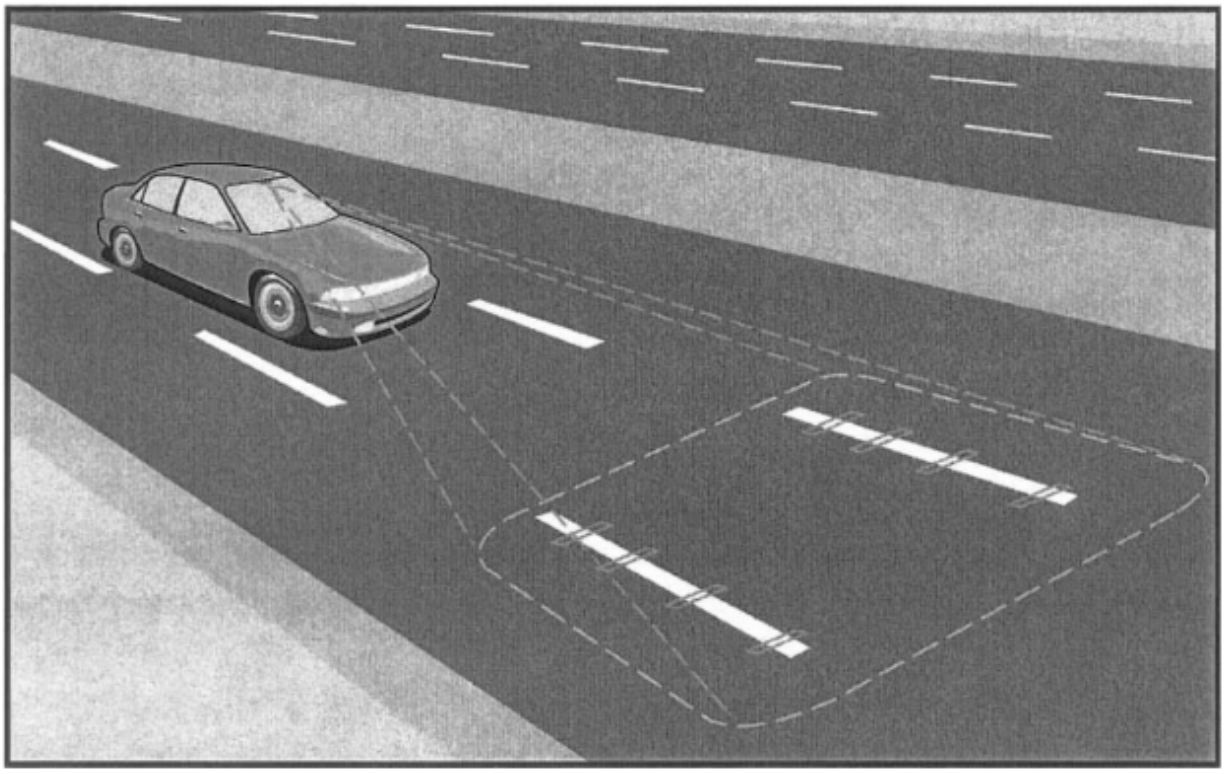

Figure 1: Line Departure Warning (LDW) System [9]

trajectory (lower curve in Figure 2). The function of the yaw stability system is to restore the yaw velocity of the vehicle as much as as possible to the nominal expected by the driver. If the friction coefficient is extremely small, then the yaw stability control may not be able to fully restore the motion, but in some cases it will make it partially (curve in the middle of Figure 2). Known types of yaw stability control are the differential braking, which utilizes the ABS system of the vehicle to restore the yaw moment, the steer-by-wire system, which applies corrections to the driver's steering commands, the active torque distribution, which utilizes the active differentials and all wheel drive technology to independently control the torque transmitted to each wheel in order to restore the yaw moment.

1.3 Rear-axle steering

Active control systems are also popular in commercial sports cars. An innovative four wheel steering [8] system has been introduced by Porsche and is applied on the commercial model 911 GT3 (Figure 3). At low speeds, the system steers the rear wheels in the opposite direction to that of the front wheels. Such steering command offers higher flexibility in negotiating tight corners due to the turning circle reduction. At higher speeds, the system steers the rear wheels in the same direction as that of the front wheels. Thanks to this virtual extension of the wheelbase, driving stability and agility are increased.

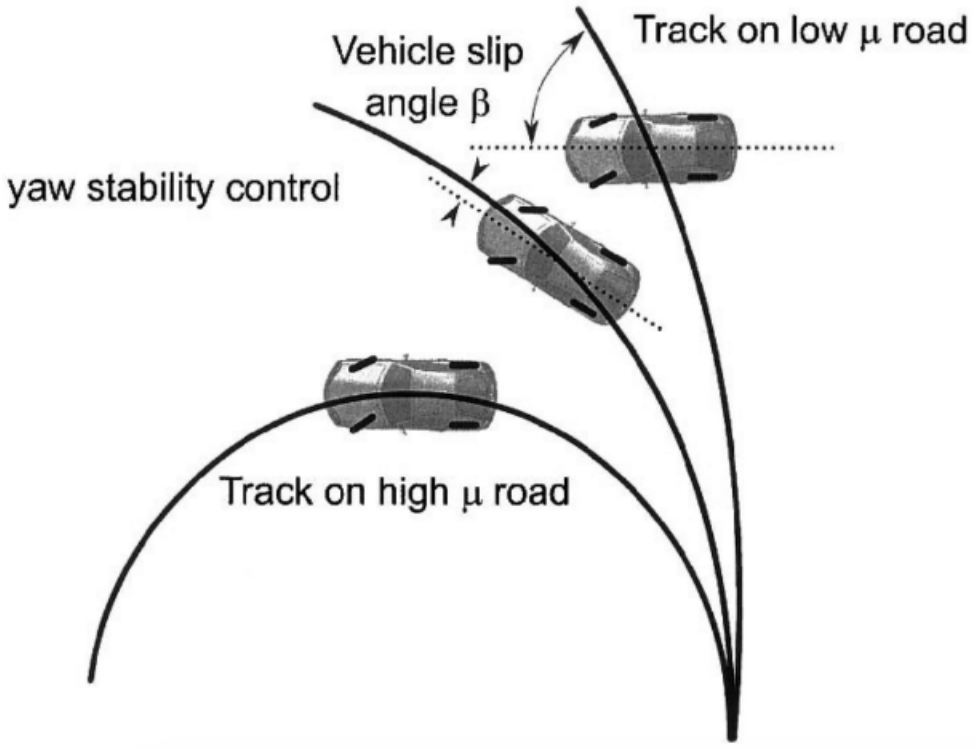

Figure 2: Yaw Stability Control system [9]

1.4 Drag reduction system

Formula 1 teams are pioneers in the fields of prototyping and innovation regarding the active control systems. The Drag Reduction System (DRS) is a popular system that was allowed by FIA in 2011. The DRS allows a F1 car to travel in higher speeds during acceleration and increases downforce during braking by adjusting the rear wing angle. In slower Formula cars, like the Formula SAE vehicle, the DRS can be used for the cooling system, as described in [13].

1.5 The objective

The systems described above are only few of an enormous list of control systems developed in automotive industry. A plethora of active systems in this list are not intended to be applied only on human driven cars. They would be essential control systems for the industry of self driving cars.

In this thesis, the design and the development of an active control mechanism as part of a prototype vehicle suspension system is studied. Generally, the objective of the system is the improvement of car behaviour while travelling through corners. This has been achieved by actively adjusting the camber angle of the front wheels. The desired camber angle is defined by using the yaw rate measurement from the vehicle sensors. The major goals of this thesis are:

Figure 3: Porsche 911 GT3

- the construction of the designed camber angle control mechanism,
- the mathematical modelling of the prototype vehicle lateral dynamics,
- the characterization of the prototype vehicle by performing appropriate experiments,
- the validation of the mathematical model using experimental data,
- the proof of concept, assuming that the proposed system will increase the lateral acceleration in cornering maneuvers.

2 Literature study

For a better understanding of the vehicle lateral dynamics mathematical modelling, some essential definitions regarding the vehicle body, the chosen coordinate systems, the tyre forces, the suspension system and the camber angle, should be given.

2.1 Lumped mass

A vehicle consists of several different components distributed within the area defined by its body. For many of the elementary analyses, all the components are assumed to be moved together during the car maneuvering. Thus, according to [2], the vehicle could be considered to behave as a lumped mass located at its center of gravity (COG) position. The point mass at the COG point is considered to be dynamically equivalent to the vehicle itself for all motions in which it is reasonable to assume the vehicle to be rigid. There are some cases, in which the wheels should be treated separately. In those cases, the lumped mass representing the body is the "sprung mass", and the wheels are denoted as "unsprung mass".

2.2 Coordinate system

For the analysis of the vehicle movement, or in general the study of vehicle dynamics, a proper coordinate system should be used. Such a system is presented in Figure 4. The longitudinal movement is taking place across the x-axis, the lateral movement across the y-axis, and the vertical one across the z-axis. The rotation of the vehicle body around the x-axis is called roll angle. The rotation of the vehicle body around the y-axis is called pitch angle. The rotation of the vehicle body around the z-axis is called yaw angle.

2.3 Tyres forces

One of the most important components in the study of the vehicle lateral dynamics is the tyres. The forces for accelerating a car in horizontal plane originate principally at the tyres. In addition, tyres are the source of the forces which are necessary to handle the car on a desired trajectory during cornering maneuvers. For the purposes of this thesis, only the lateral behaviour of the tyres will be studied and analyzed.

In accordance with SAE J670 [4] terminology, regarding the tyre section, the total force and moment exerted on the tyre by the road can be represented by three force components and three moment components. The components for both force and moment are depicted in Figure 5, in which the Z-UP coordinate system is presented. As shown, all the forces originate at the center of the tyre contact with the road. Each force follows the direction of the related axis, while each moment direction can be defined by using the right hand thumb rule around the related axis.

As shown in Figure 8, there is a non linear relation between the slip angle and the lateral force of the tyre. Though, if the slip angle is small enough, then the relation could be considered as linear. All the slip angle values, for which the lateral force curve has constant slope, create a region which is called elastic or linear [14]. In that region, the relation between the lateral force and the slip angle is expressed by the Equation 1.

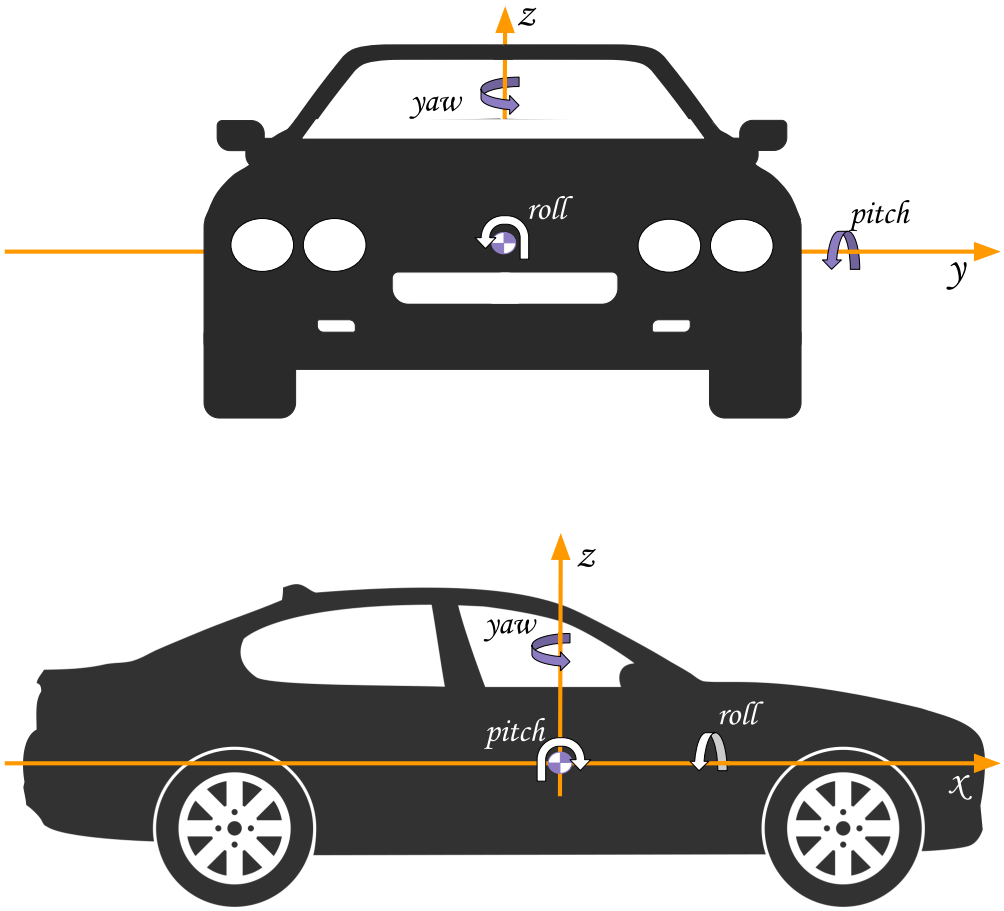

Figure 4: Three dimensional coordinate system

$$F_y = C_a \alpha \tag{1}$$

Where F_y is the lateral force, α is the slip angle and C_α expresses the tyre cornering stiffness, which mathematically represents the slope of the lateral force curve in the linear region.

A negative cambered wheel can provide greater lateral force through its tyre. As presented in Figure 9, this additive lateral foce is not linear in the transitional region. On the other hand, as described in [7], the cambered tyre additive lateral force occurs from the Equation 2.

$$F_{y\gamma} = C_\gamma \gamma \tag{2}$$

Where $F_{y\gamma}$ is the lateral force due to the camber angle of the wheel, γ is the camber angle of the wheel and C_γ represents the camber stiffness of the tyre. Finally, the total latera force of the tyre in the elastic/linear region equals to the summation of the lateral force due to the tyre slip angle and the lateral force occured due to the camber angle of the wheel (Equation 3).

$$F_y = C_\alpha \alpha + C_\gamma \gamma \tag{3}$$

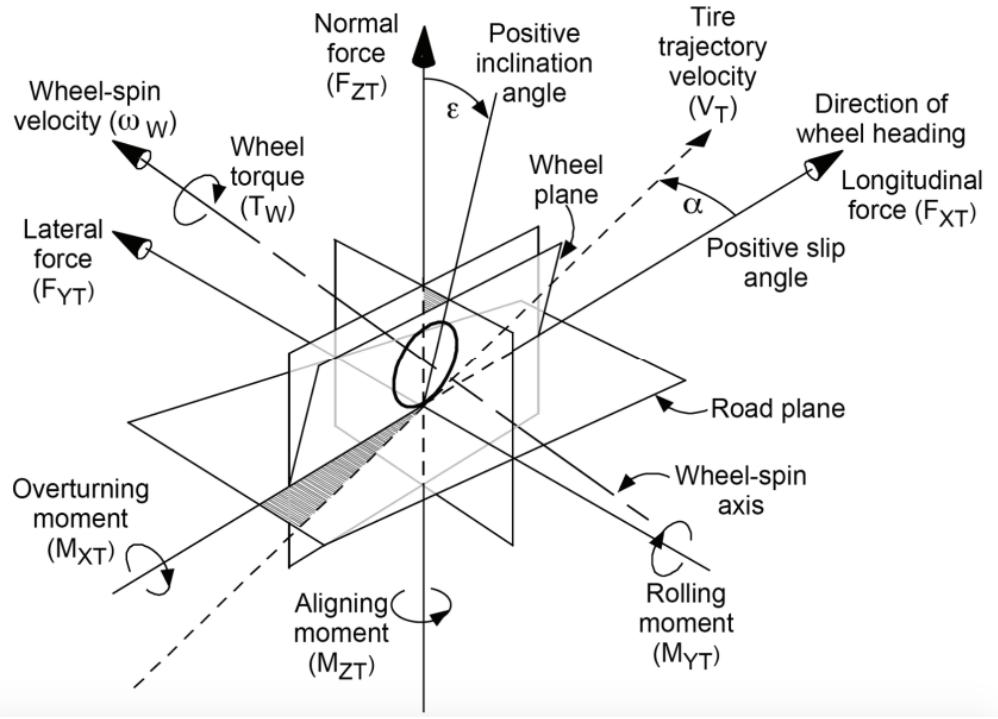

Figure 5: Tyre force and moment nomenclature Z-UP [4]

2.4 Suspension systems

A suspension system allows the wheels movement with respect to the vehicle body. Thus, a good suspension system can provide better handling to the car and at the same time, it can offer a more comfortable ride to the passengers of the vehicle. A generic classification of the suspension systems introduces two major categories, the dependent and the independent suspensions [3].

Using a dependent suspension, the motion of a wheel on one side is related to the motion of its partner on the other side. Thus, if the wheel on one side travels vertically due to a bump or a pot-hole, then the effect of that movement gets transmitted directly to the wheel partner on the other side. Using an independent suspension, each wheel behaves independently from its pair. So, a disturbance at a wheel on one side is not transmitted to its partner on the other side.

2.4.1 Dependent suspension

The dependent suspension system is not so commonly used on passenger cars anymore because especially nowdays automotive industry tends to equip cars with more sophisticated structures based on the safety and comfort. Though, this suspension type is simple in construction and almost completely eliminates the camber change thereby reducing tyre wear. That is the reason they are still in use and they are more common at the rear of front-wheel drive light commercial and off-road vehicles. The most known dependent suspension systems are the *Hotchkiss rear suspension* (Figure 6a) and the *Trailing arm - rigid axle*

suspension (Figure 6b).

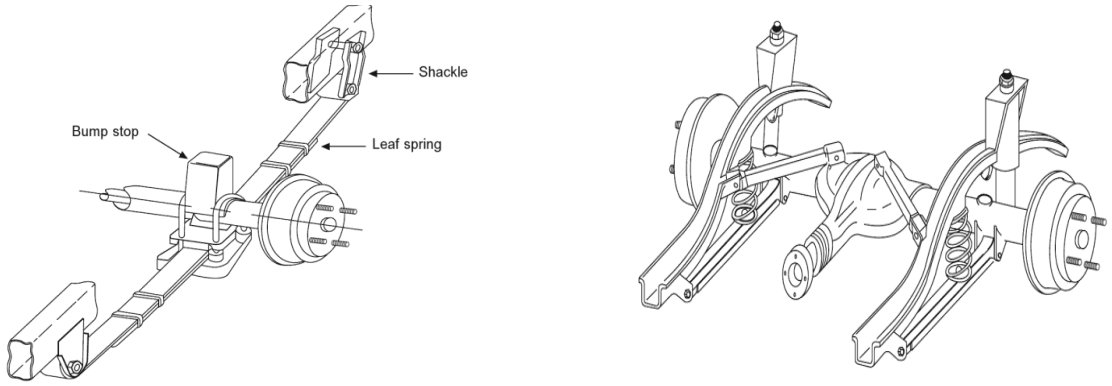

(a) The hotchkiss rear suspension [3] (b) The trailing arm - rigid axle suspension [3]

Figure 6: Two common types of dependent suspension systems

2.4.2 Independent suspension

On the other hand, independent systems are the most common type of suspensions used in all types of cars, including racing cars. They have benefits in packaging ang give greater design freedom, when compared to dependent systems. Due to their independency, they are more suitable for active system applications, which is a trend in automotive industry nowadays.

The most popular independent suspension systems are the *MacPherson strut* (Figure 7a), the *Double wishbones*(Figure 7b), and the *Multi-link suspension*(Figure 7c). All of them are used for both the front and the rear wheels of a car. Other independent suspension systems are the *Trailing arms*(Figure 7d), the *Swing axles*(Figure 7e) and the *Semi-trailing arms*(Figure 7f). Those suspension systems are commonly used for the rear wheels of a car.

The suspension system of the prototype vehicle used for the purposes of the thesis is mostly similar to the independent double wishbone structure. The only difference is that instead of the upper wishbone, there is a single arm that keeps the upper part of the wheel attached to the vehicle body. A more detailed analysis of the prototype vehicle suspension system is presented in Chapter 4.

2.5 Camber angle definition

As described in [2], camber angle is defined to be the inclination of a wheel outward from the vehicle body. A wheel could have non zero camber angle (with respect to the vehicle body) due to the configuration of the suspension system. Furthermore, a wheel may gain camber angle (with respect to the ground) when the vehicle travels through a corner and the body has non zero roll angle. Finally, the total wheel camber angle with respect to the ground is given by the Equation 4.

$$\gamma_g = \gamma_b + \phi \tag{4}$$

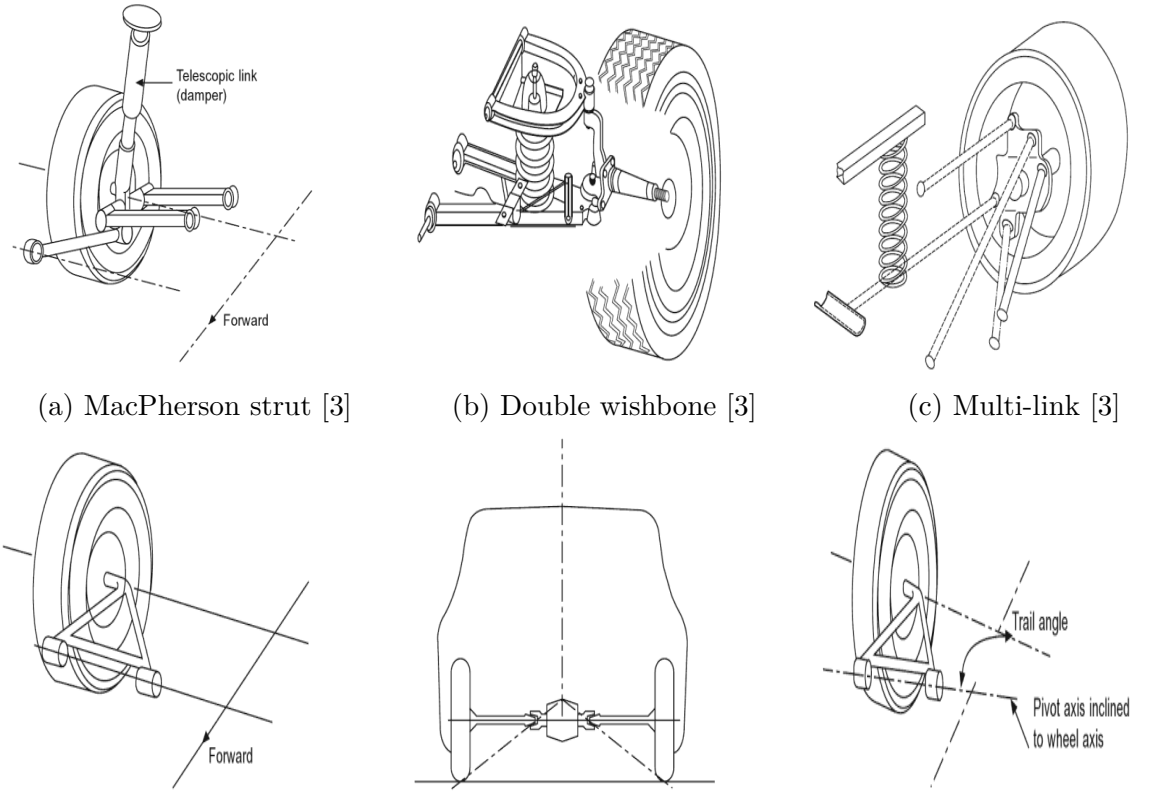

(a) MacPherson strut [3] (b) Double wishbone [3] (c) Multi-link [3]

(d) Trailing arms [3] (e) Swing axles [3] (f) Semi-trailing arms [3]

Figure 7: Common types of independent suspension systems

where:

- γ_g = Camber angle with respect to the ground
- γ_b = Camber angle of the wheel with respect to the vehicle body
- ϕ = Roll angle of the vehicle

2.6 Negative camber angle configuration

Since camber angle is defined to be the inclination of a wheel outward from the vehicle body, it is following that this inclination is considered as positive. On the other hand, if the inclination of the wheel is inward to the vehicle body, then the inclination is considered to be negative. Thus, the suspension system configuration in Figure 11 is known as Negative Camber. While the the suspension system configuration in Figure 12 is known as Positive Camber. Of course, there is also the Neutral Camber configuration shown in Figure 13, when the wheels are in parallel with the vehicle body.

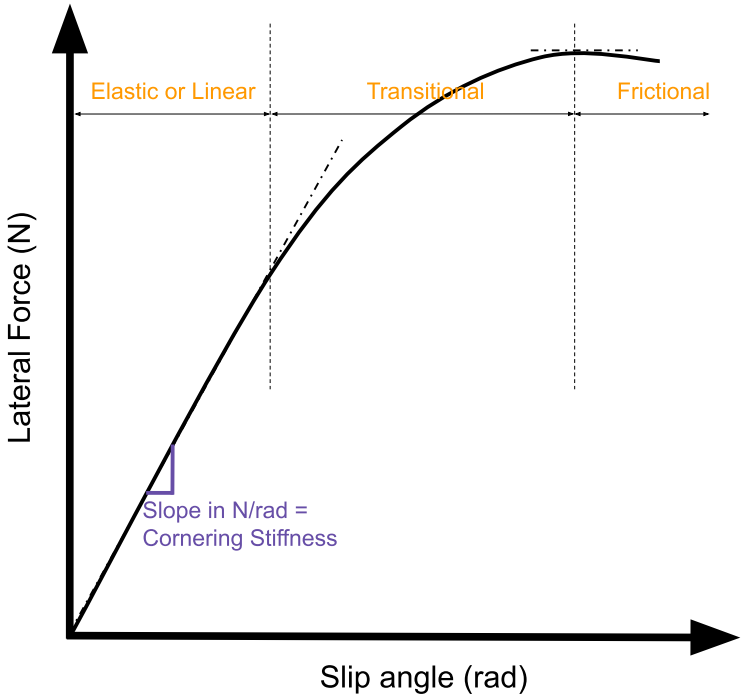

Figure 8: Lateral force vs slip angle for a racing tyre [14]

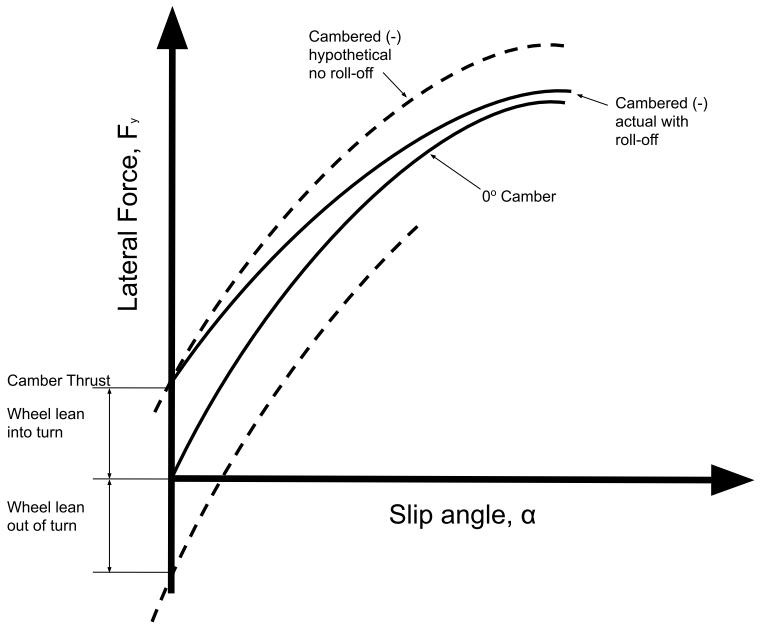

Figure 9: Camber thrust and camber roll-off at constant load [14]

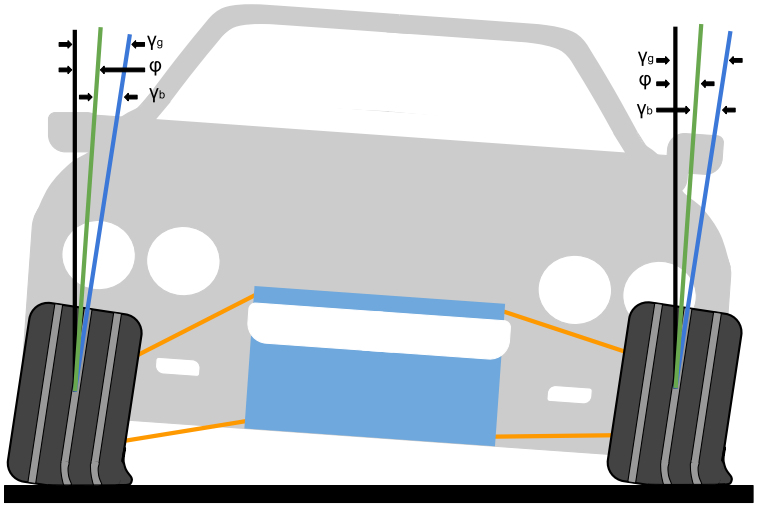

Figure 10: Total camber angle of the wheel with respect to the ground

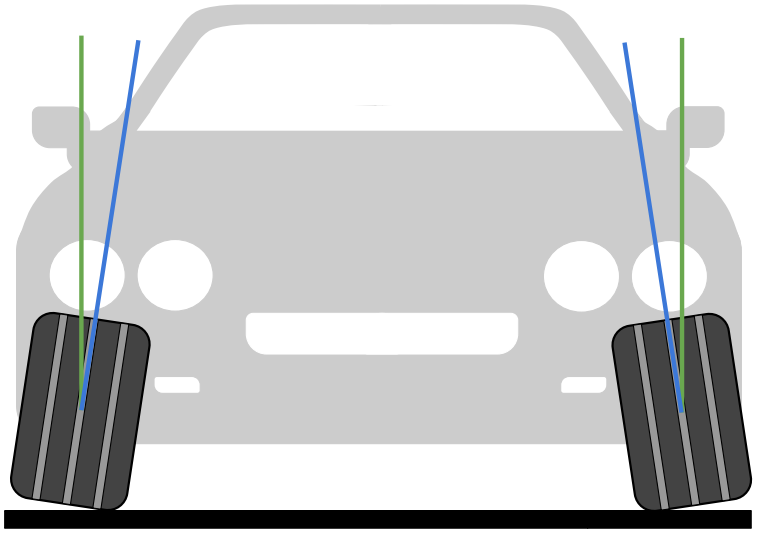

Figure 11: Negative camber configuration

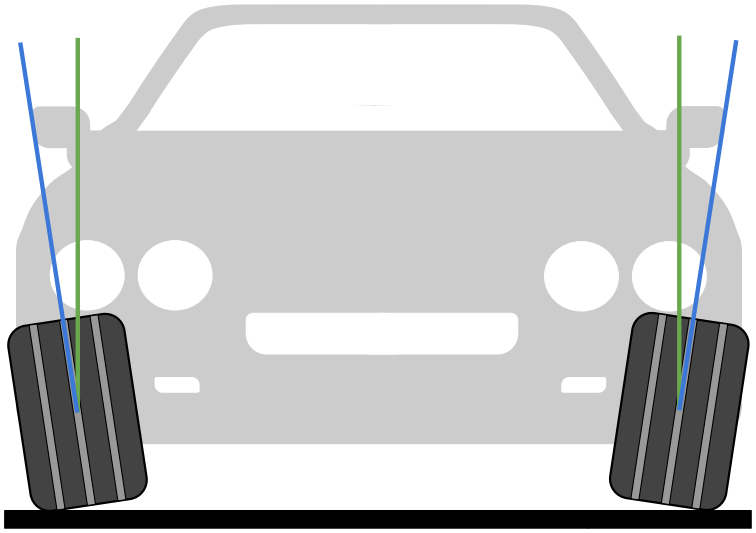

Figure 12: Positive camber configuration

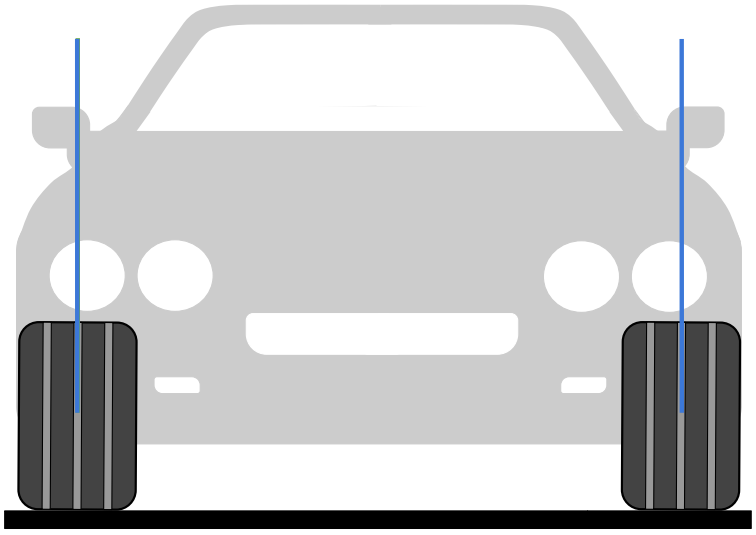

Figure 13: Neutral camber configuration

A lot of research is related to the camber angle control. In the majority of the publicated research the effects of the camber angle adjustment on car handling or the effectiveness of camber angle adjsutment mechanism are studied. Thus, in the related publications, the control algorithm has not been explored extensively.

2.7 Study on the effects of camber control on vehicle dynamics

In publication [15], the effects of camber control on vehicle dynamics have been studied. Two prototype vehicles were used for experimentation, a remote control model car (right image in Figure 15) and a one seater car (left image in Figure 15). During the experimentation, camber angle were being adjusted for all four wheels of the cars proportionally to the steering angle, according to the relation of the Equation 5.

$$\delta_c = \frac{1}{n_c}\delta_H \tag{5}$$

Where δ_c is the camber angle of the model car, δ_H is the steering angle and n_c expresses the camber angle gear ratio of the mechanism. For the mathematical modelling of the vehicle, a nonlinear two-track model along with a nonlinear tyre model were used. The two track model is governed by the Equations 6-8.

$$mv(\dot{\beta} + r) - m_s h_s \ddot{\phi} = F_{1i} + F_{1o} + F2i + F_{2o} \tag{6}$$

$$I_z \dot{r} = a(F_{1i} + F_{1o}) - b(F_{2i} + F_{2o}) \tag{7}$$

$$I_\phi \ddot{\phi} + C_\phi \dot{\phi} + K_{\phi s}\phi = m_s h_s v(\dot{\beta} + r) \tag{8}$$

Where:

- I_z, I_ϕ represent the yaw and roll moment of intertia respectively,
- m, m_s is the vehicle total mass and the spring mass respectively,
- β is the slip angle,
- ϕ, r express the roll and yaw angle respectively,
- h_s is the center of gravity height of spring mass,
- F_{mn} is the side force of each wheel (m=i,o is inner or outer wheels. n=1,2 is front or rear wheels),
- C_ϕ is the roll damping coefficient,
- $K_{\phi s}$ is the roll stifness,
- v is the vehicle velocity vector

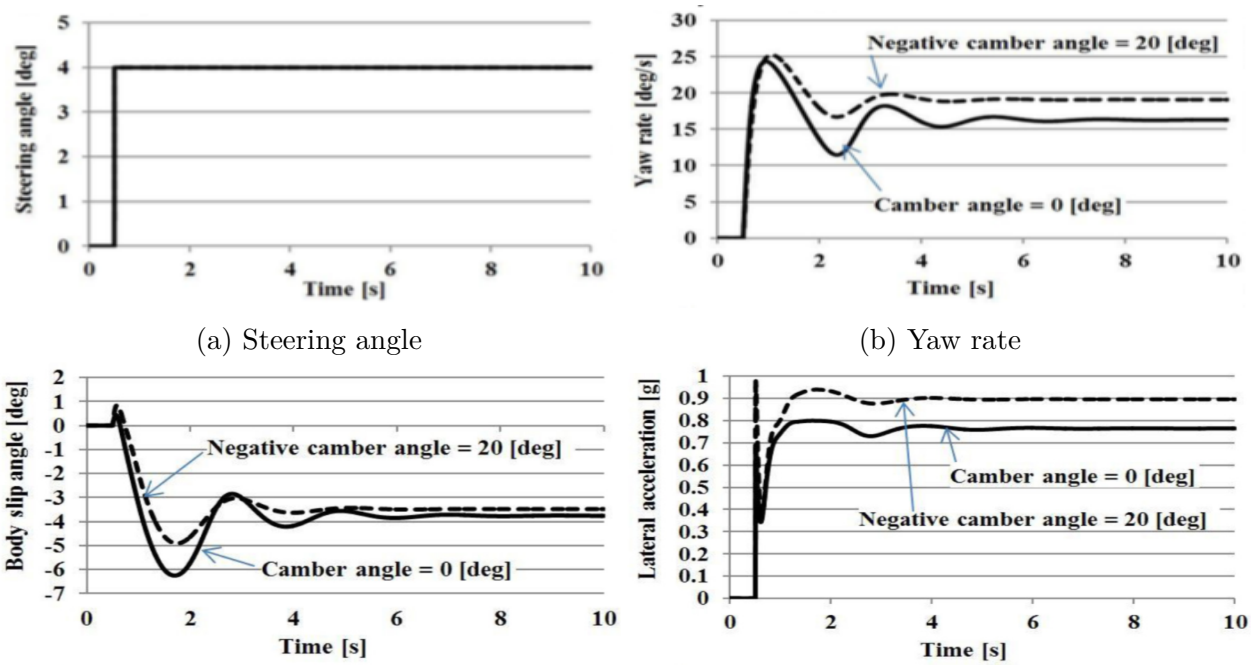

(a) Steering angle

(b) Yaw rate

(c) Slip angle

(d) Lateral acceleration

Figure 14: Computational results [15]

According to the commentary of the computation results in [15], when the proposed camber angle system is disabled, with a step steering as input 14a, the body slip angle and lateral acceleration curves 14c, 14b are nearly the same as the threshold limit value at which a steady circular turn can be maintained through moment method analysis, when the vehicle has settled into a steady state. From this, it is evident that the cornering limit is simulated. When ground negative camber angle control that is proportional to the steering angle is implemented, convergence of the yaw rate and body slip angle is improved compared to when it is not implemented, and the vehicle swiftly settles into a steady state. From the lateral acceleration circular maneuver results, when the camber angle control system was disabled, the lateral acceleration limit at the steady state was 0.8 g. On the other hand, when ground negative camber angle control that is proportional to the steering angle was implemented, this limit at the steady state improved to 0.9 g. Thus, cornering limit performance is significantly improved with the camber angle adjustment system enabled.

According to the experiments results, where negative camber control proportional to steering ($+-20^o$) was implemented, lateral acceleration improved by approximately 0.10-015 g (Figure 16), as compared to the case in which no control was implemented. Moreover, when camber angle control was implemented, the speed was 2.3 m/s, whereas the speed was 2.1 m/s for the case in which no camber angle control was implemented, indicating an improved potential cruising speed during cornering.

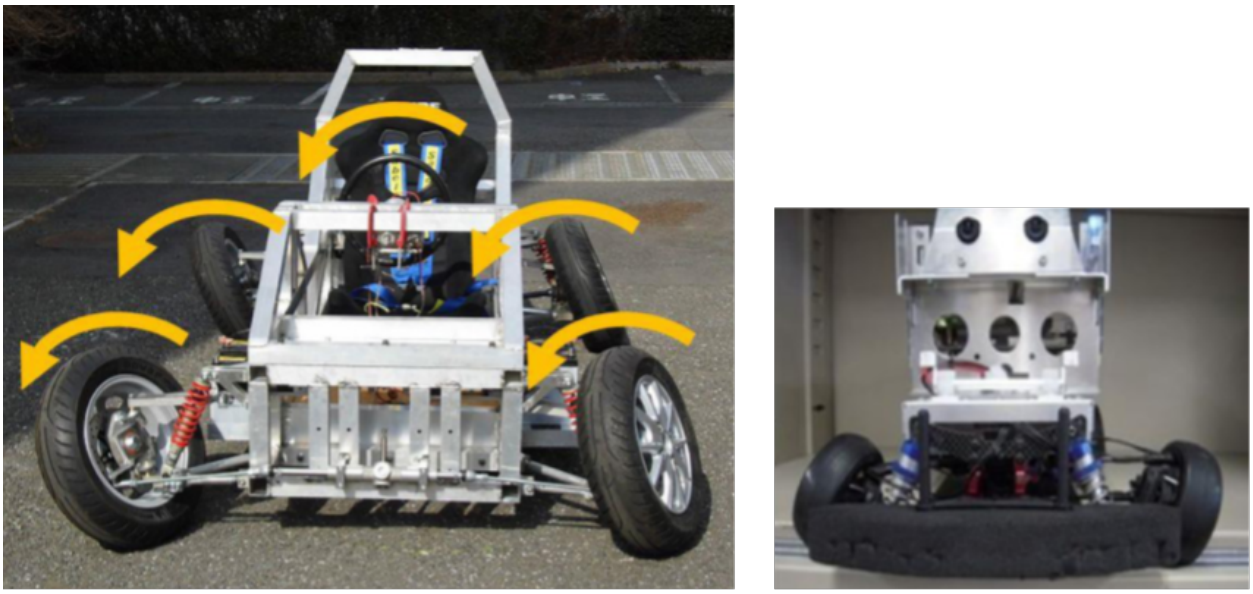

Figure 15: The prototype vehicles used for the experiments of research [15]

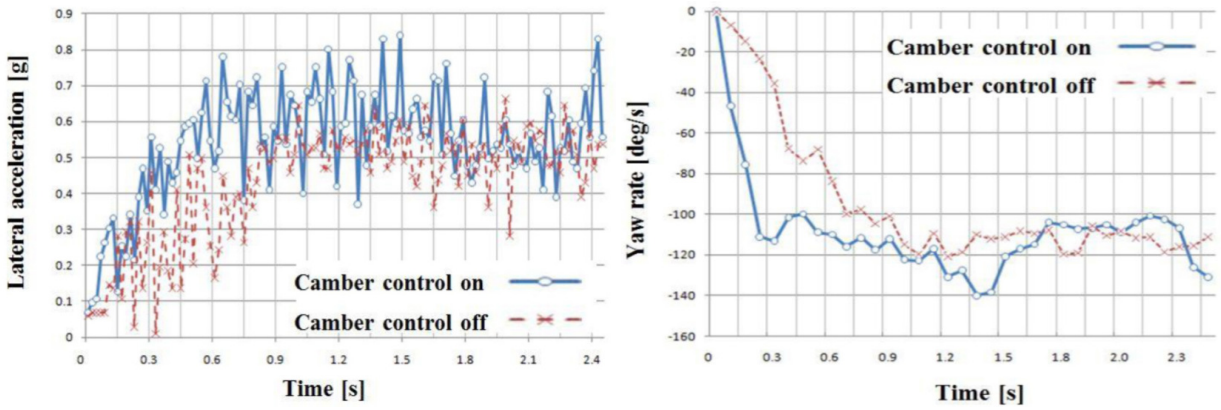

Figure 16: Experimentation results of the research [15]

2.8 Prototype hydraylic mechanism for camber angle adjustment

In publication [1], a prototype hydraylic mechanism for the camber angle adjustment is proposed. The mechanism is applied on a typical double wishbone suspension. The crankshaft is jointed to the vehicle body while its sides are attached to the upper wishbone. Two hydraulic cylinders adjsust the camber angle by rotating the crankshaft as shown in Figure 21.

2.9 Wheel suspension with automatic camber adjustment

In patent [11], a pure hydraulic system is presented for controlling the camber angle of the wheels. In accordance with the invention, provision is made, for example, that hydraulic master cylinders be arranged between the chassis and the oscillating or swinging wheel uprights or suspension elements (suspension arms), the working spaces of these cylinders being

mutually cross-coupled and the cylinders controlling slave cylinders on the upper suspension arms thereby producing a compensating effect for any alteration in the wheel camber in dependence on the rolling movement of the chassis.

Two alternative configurations are presented. According to the first proposed configuration, a slave cylinder is placed on the upper arm of each wheel. In this way, each master cylinder controls its paired slave cylinder, adjusting the camber angle of the wheel related to. In Figure 17, the descripted configuration is presented from the rear view of the vehicle, while it is in a steady state. In Figure 18, the descripted configuration is presented from the rear view of the vehicle, while its body has a non negative roll angle. As expected, the wheels have zero camber angle in both cases, so the grip is maximized.

According to the second alternative configuration, presented in patent [11], there is no cylinder on the upper arm of the wheel. There is a single slave cylinder connected to vertical rotating tie rods, on which the upper arms of the wheels are attached. Both master cylinders control the slave one, adjusting the camber angle of the wheels. In Figure 19, the descripted configuration is presented from the rear view of the vehicle, while it is in a steady state. In Figure 20, the descripted configuration is presented from the rear view of the vehicle, while its body has a non negative roll angle. As expected, the wheels have zero camber angle in both cases, so the grip is maximized.

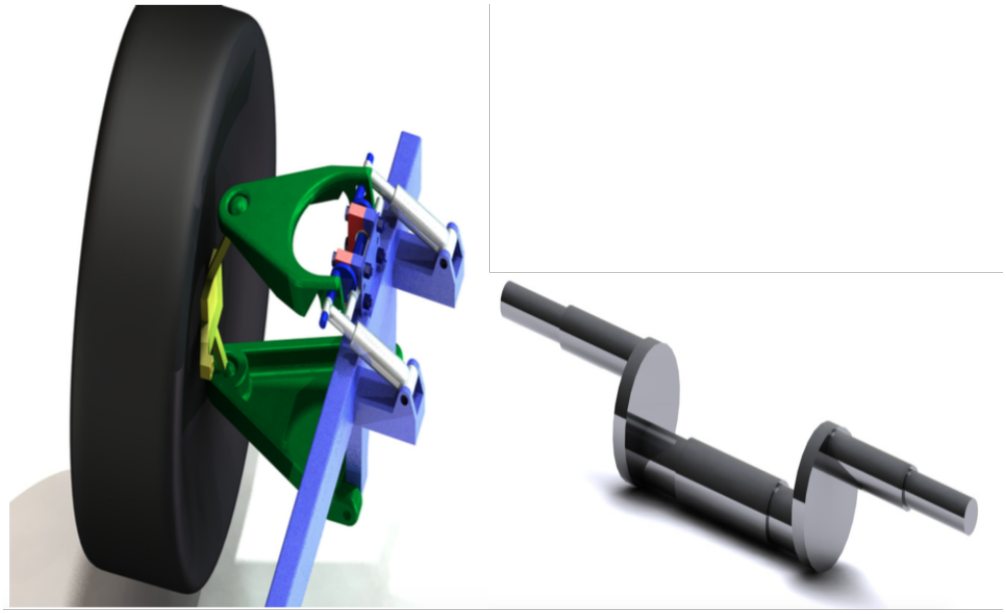

Figure 17: Camber angle adjustment mechanism proposed in publication [1]

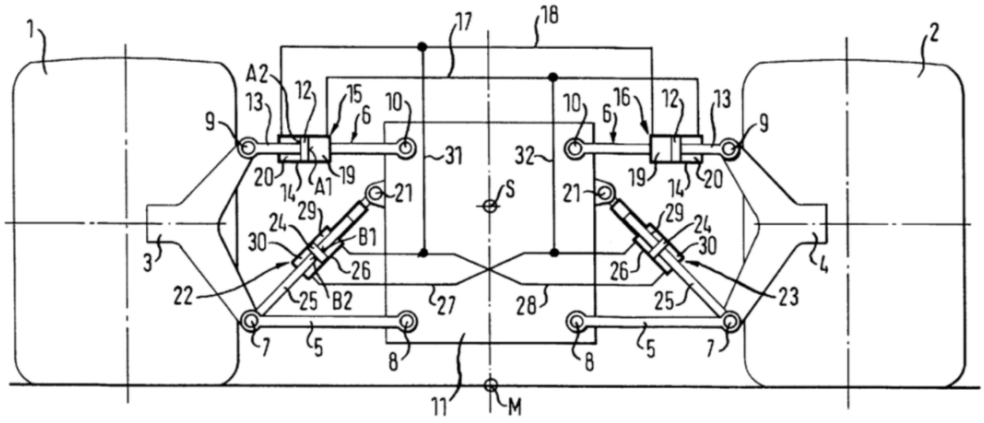

Figure 18: Camber angle adjustment mechanism proposed in publication [1]

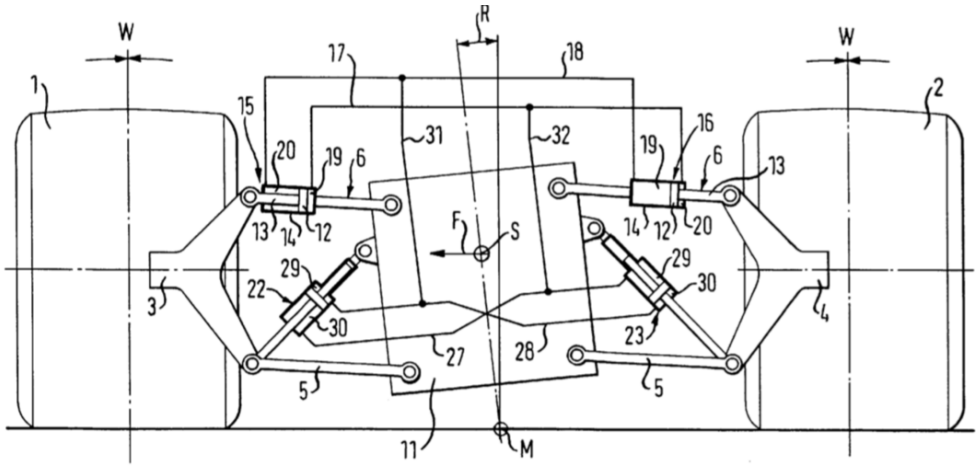

Figure 19: Camber angle adjustment mechanism proposed in publication [1]

2.10 Active camber and toe control strategy for the double wishbone suspension system

In this paper [5], a control mechanism is presented for camber angle adjusting when a car travels over bumps and potholes. A quarter car physical model was used for the experimentation and simulation of the system. The simulation result shows an improvement of 58% in camber and 96% improvement of toe characteristics. A prototype of the proposed system is developed and subjected to the same test as the simulation system. The prototype achieved an improvement of 46.34% in camber and a 93.35% in the toe variation of the active system over the passive system. Further, the prototype was able to achieve 89% of camber reduction and 45% of toe reduction with respect to the simulation. The testbed of the system is presented in Figure 22. As shown in Figure 23, the control system significantly inproved the camber angle curve in relation to the passive system response, while 0 degrees of constant camber angle is the desired curve (blue line in Figure 23).

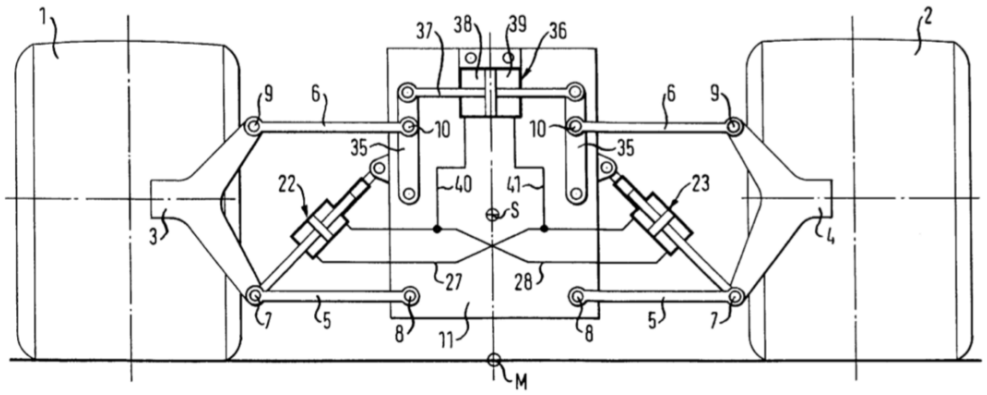

Figure 20: Camber angle adjustment mechanism proposed in publication [1]

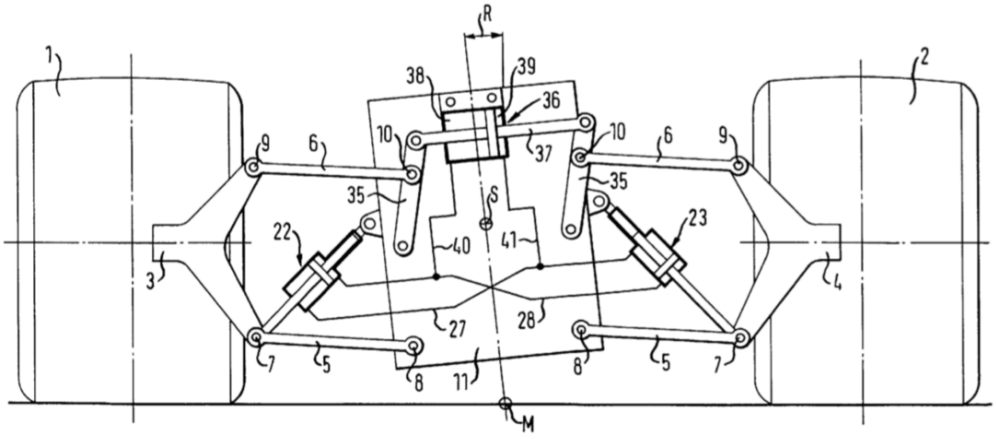

Figure 21: Camber angle adjustment mechanism proposed in publication [1]

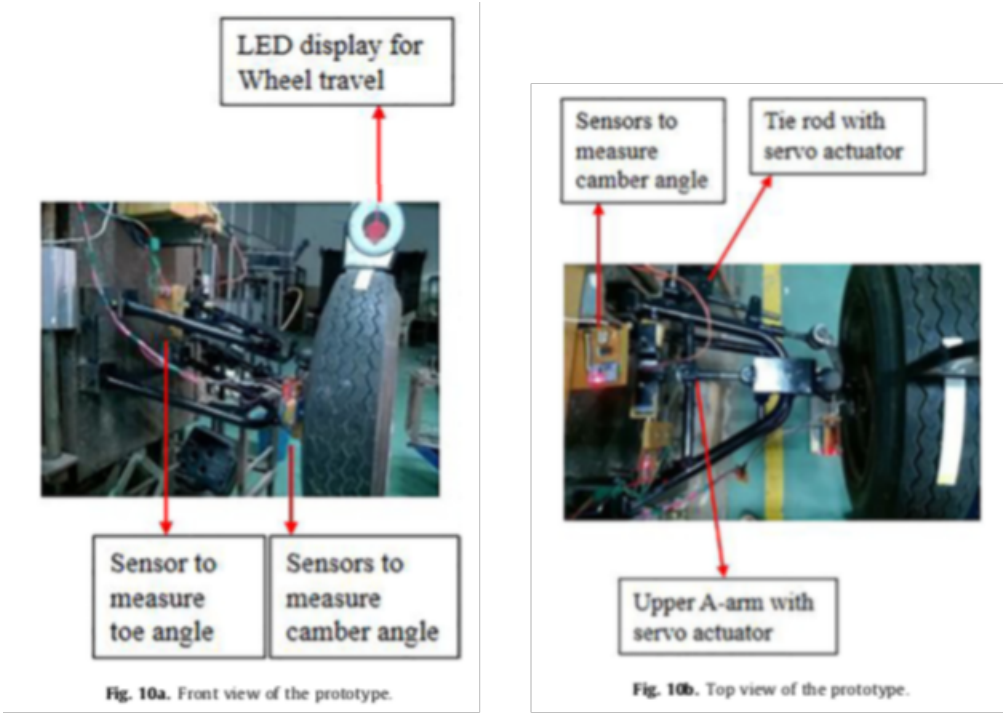

Figure 22: Camber angle adjustment mechanism proposed in publication [5]

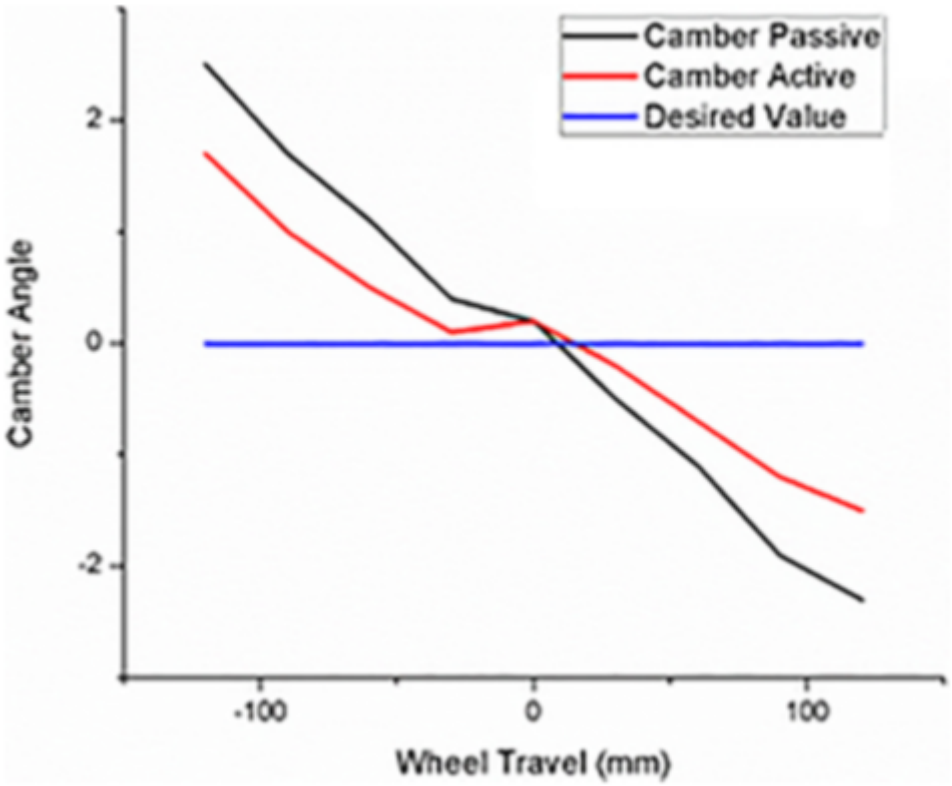

Figure 23: Camber angle response of prototype [5]

3 The proposed system

3.1 The prototype vehicle

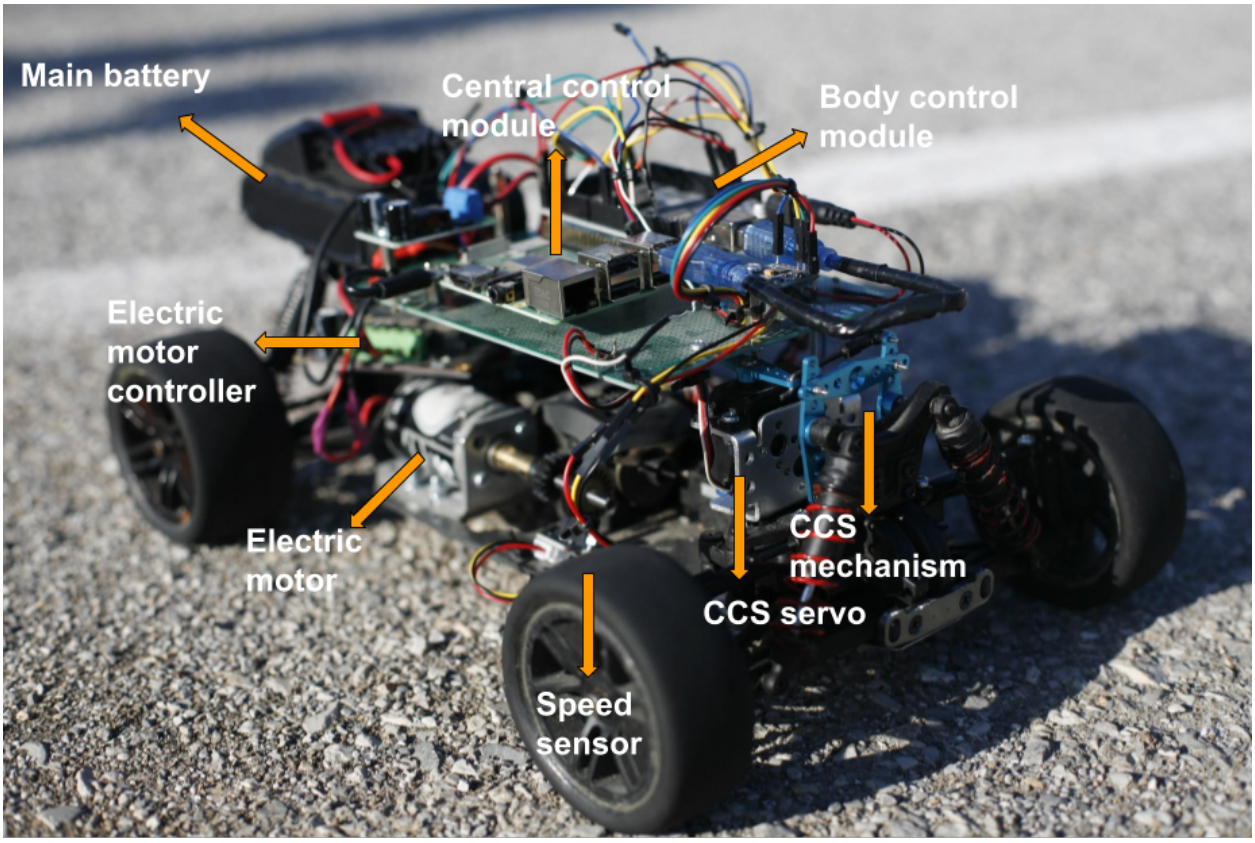

Figure 24: The prototype vehicle modules

The prototype vehicle used for the purposes of this thesis, consists of many modules as shown in Figure 24. A short description of the vehicle main parts follows:

- the main battery of the system is located on top of the rear suspension system,
- the electric motor the vehicle propulsion system is located on the right side of the chassis,
- the electric motor controller is right above the motor,
- the speed sensor with its rotary wheel is located in front of the electric motor,
- the camber angle control mechanism is installed on the rear side of the vehicle front suspension,
- the camber angle control servo is located right behind the vehicle front suspension,
- both the central control module and the body control module are attached on top of the vehicle

3.2 Specifying the position of vehicle's center of gravity

The vehicle's center of gravity (COG) position is an essential part of the vehicle dynamics study. It is considered to be the point of the vehicle where all the forces are applied to. Thus, the specification of the exact COG position is crucial for modelling and simulating the vehicle behaviour.

3.2.1 The COG longitudinal position

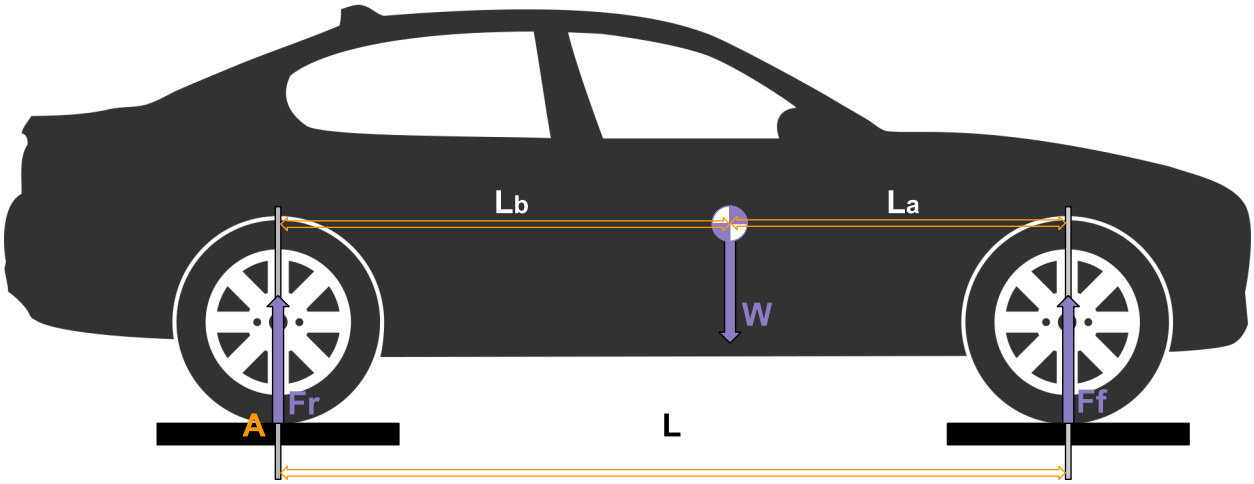

Figure 25: Specifying the longitudinal position of COG

For the specification of the COG longitudinal position, it is necessary the front axle weight (W_f) as much as the rear axle weight (W_r) to be measured. Each axle weight causes a ground reaction. As shown in Figure 25, W_f causes the ground reaction F_f and W_r causes the ground reaction F_r. W is the total weight of the vehicle, it is the summation of W_f and W_r and is applied to the COG point.

Since the vehicle is being on a steady state, the summation of the forces, in the vertical direction, equals to zero. Moreover, the summation of the moments around any point (i.e point A, Figure 25) should be zero. Thus

$$\Sigma M_A = 0$$

$$\Rightarrow F_f * L - W * L_b = 0$$

$$\Rightarrow L_b = \frac{F_f * L}{W} \tag{9}$$

Also

$$|F_f| = |W_f|$$

$$L = L_a + L_b \tag{10}$$

Where, L is the wheelbase of the vehicle, L_a is the distance between front axle center and COG position, and L_b is the distance between rear axle center and COG position. Finally, using Equation 9 and Equation 10, the quantities L_a and L_b could be specified.

3.2.2 The COG lateral position

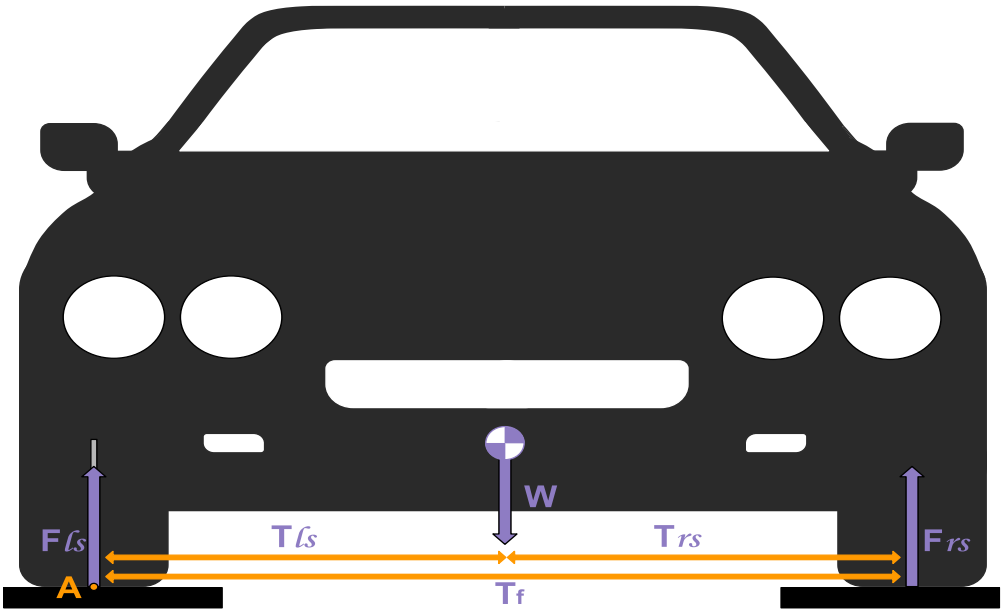

Figure 26: Specifying the lateral position of COG

For the specification of the COG lateral position, it is necessary the vehicle left side weight (W_{ls}) as much as the vehicle right side weight (W_{rs}) to be measured. Each side weight causes a ground reaction. As shown in Figure 26, W_{ls} causes the ground reaction F_{ls} and W_{rs} causes the ground reaction F_{rs}. W is the total weight of the vehicle, it is the summation of W_{ls} and W_{rs} and is applied to the COG point.

Since the vehicle is being on a steady state, the summation of the forces, in the vertical direction, equals to zero. Moreover, the summation of the moments arount any point (i.e point A, Figure 26) should be zero. Thus

$$\begin{aligned} \Sigma M_A &= 0 \\ \Rightarrow F_{ls} * T_f - W * T_{ls} &= 0 \\ \Rightarrow b &= \frac{F_{ls} * T_{ls}}{W} \end{aligned} \tag{11}$$

Also

$$\begin{aligned} |F_{ls}| &= |W_{ls}| \\ L &= T_{ls} + T_{rs} \end{aligned} \tag{12}$$

Where, Tf is the front wheels tread, T_{ls} is the lateral distance between the front left wheel and COG position, and T_{rs} is the lateral distance between front right wheel and COG position. Finally, using Equation 11 and Equation 12, the quantities T_{ls} and T_{rs} could be specified.

3.2.3 The COG height from the ground

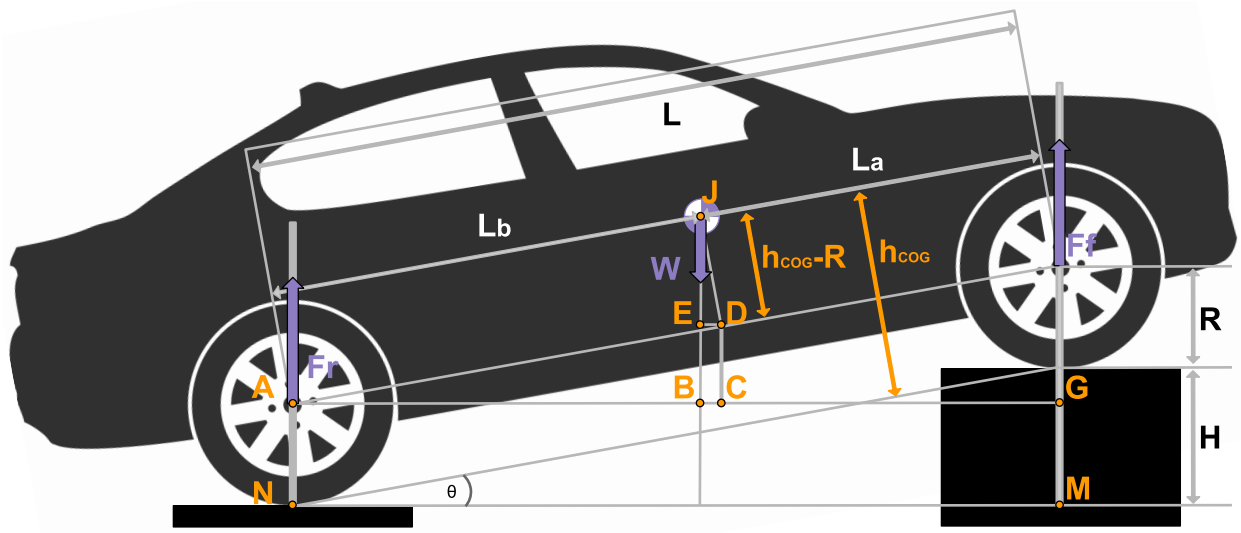

Figure 27: Specifying the height of COG

For the calculation of the COG heigth (h_{COG}) from the ground, it is necessary the front or the rear axle of the car to be lifted to a known height (H), as shown in Figure 27. Again, the vehicle is set on a steeady state with the front axle lifted. Therefore, the summation of forces ($\Sigma F_{vertical}$) in the vetical direction equals to zero. Also, the summation of moments (i.e around point A ΣM_A) around any point equals to zero.

$$\Sigma F_{vertical} = 0 \Rightarrow F_f + F_r - W = 0 \Rightarrow F_f = W - F_r \tag{13}$$

$$\Sigma M_A = 0 \Rightarrow F_f * AG - W * AB = 0 \tag{14}$$

$$\left.\begin{array}{l} AG = L * cos(E\hat{A}B) \\ E\hat{A}B = \theta \end{array}\right\} \Rightarrow AG = L * cos\theta \tag{15}$$

$$(14) \overset{(15)}{\Longrightarrow} F_f * L * cos\theta - W * AB = 0 \tag{16}$$

$$\left.\begin{array}{l} ED = BC \\ ED = (h_{cog} - R) * sin(E\hat{J}D) \\ E\hat{J}D = \theta \end{array}\right\} \Rightarrow BC = (h_{cog} - R) * sin\theta \tag{17}$$

$$\left.\begin{array}{l} AC = L_b * cos(E\hat{A}B) \\ E\hat{A}B = \theta \end{array}\right\} \Rightarrow AC = L_b * cos\theta \tag{18}$$

$$\left.\begin{array}{l} AB = AC - BC \\ (17) \\ (18) \end{array}\right\} \Rightarrow AB = L_b * cos\theta - (h_{cog} - R) * sin\theta \tag{19}$$

$$(16) \overset{(19)}{\Longrightarrow} F_f * L * cos\theta - W * (L_b * cos\theta - (h_{cog} - R) * sin\theta) = 0$$

$$\Rightarrow h_{cog} = (\frac{F_f}{W} * L - L_b) * cot\theta + R \tag{20}$$

Using Equation 20, the height of COG position from the ground could be calculated.

3.3 The vehicle electronics

For the development of the proposed active control system, several electronic components were necessary. Sensors were used to collect essential measurements like the vehicle velocity, yaw rate, steering angle, throttle command etc. In addition, some actuators were needed as much for the normal movement of the vehicle like steering and acceleration as for the extended functionality of the camber angle adjustment. Moreover, two electronic control units were chosen for the sensors data processing and the manipulation of the actuators.

3.3.1 The electronics structure

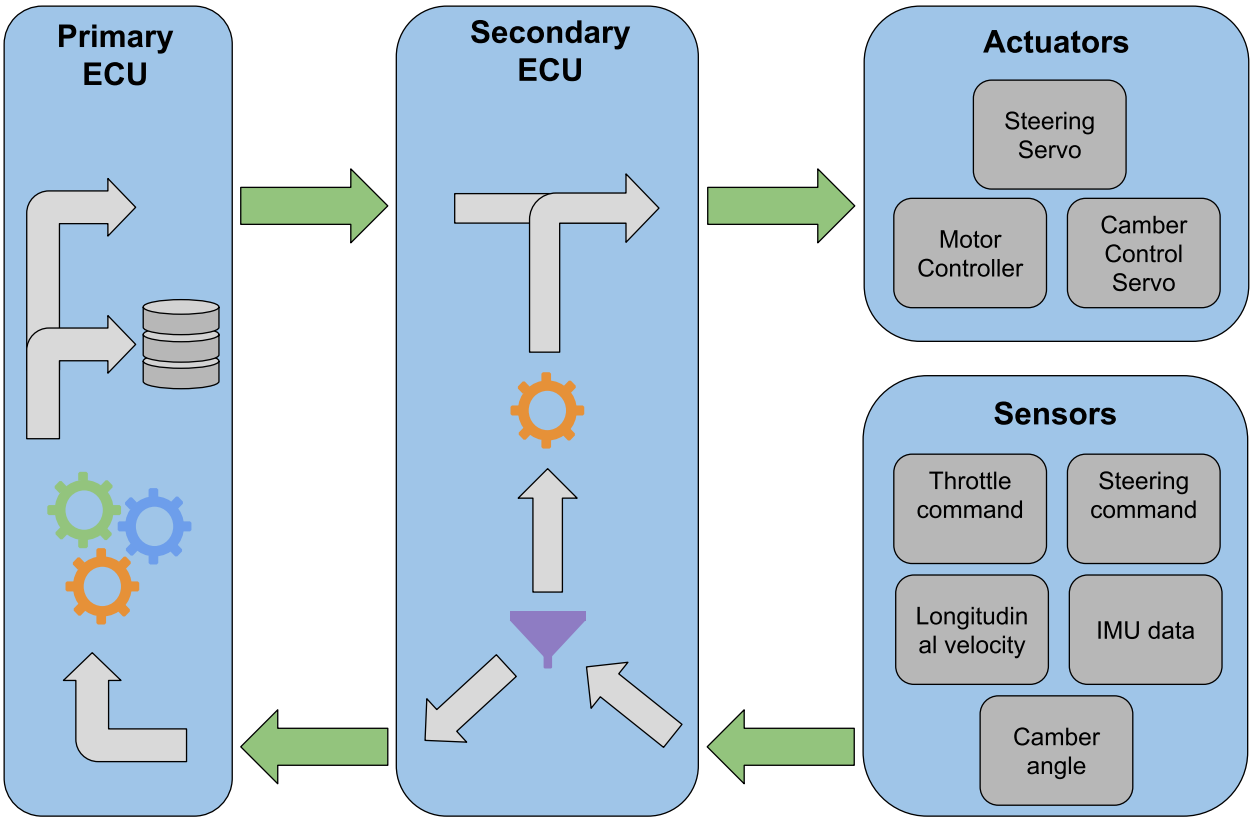

Figure 28: The electronics structure

In Figure 28, the structure and the data flow of the electronic system are depicted. As shown, the system consists of two Electronic Control Units (ECUs), the actuators and the sensors. The primary ECU is called Central Control Unit (CCM), while the secondary one is called Body Control Module (BCM).

The sensors raw data are being received by the BCM, which applies filters to them and creates some necessary data structures. Furthermore, in the BCM, simple controlling software is being excecuted for some basic functionalities like predefined automated maneuvers.

The structured data from the BCM is being passed to the CCM, in which the main controller of the system exists. The data is being processed by the main controller and when a desired body camber angle is calculated, it is being passed as a command to the camber

angle control servo through the BCM. At the same time, all the filtered/structured data, including the output of the main controller, is being saved to the storage of the CCM.

3.3.2 The primary ECU - Central Control Module (CCM)

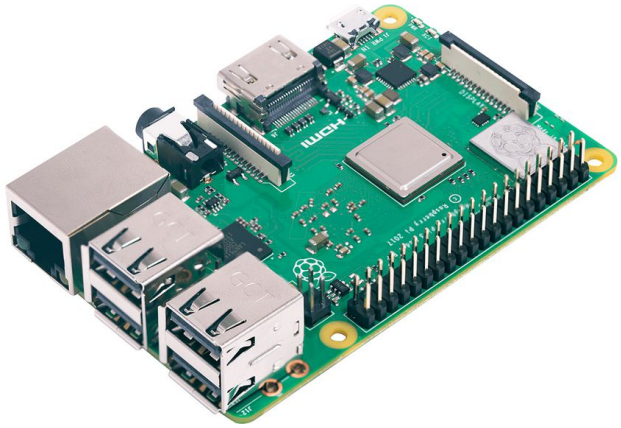

Figure 29: Raspberry pi 3 model B+ - The Central Control Module (CCM)

For the implementation of the Central Control Module, the micro-computer Raspberry pi 3 model B+ (Figure 29) was used. The main charasteristics of the Raspberry Pi are:

- processor Broadcom BCM2837B0, Cortex-A53 (ARMv8) 64-bit SoC @ 1.4GHz,
- main memory 1GB LPDDR2 SDRAM,
- power input 5V/2.5A DC,
- 4 USB 2.0 ports,
- Micro SD port for loading the operating system and storing data

Raspberry pi was selected as the primary ECU because it is a reliable product, it has a powerfull processor for the needs of the project and it can log a big amount of data in its external micro SD card.

3.3.3 The secondary ECU - Body Control Module (BCM)

For the implementation of the Body Control Module, the micro-controller Arduino Mega 2560 Rev3 (Figure 30) was used. The main charasteristics of the Arduino are the following:

- microcontroller ATmega2560,
- input Voltage (recommended) 7-12V,
- input Voltage (limit) 6-20V,
- digital I/O Pins 54 (of which 15 provide PWM output),

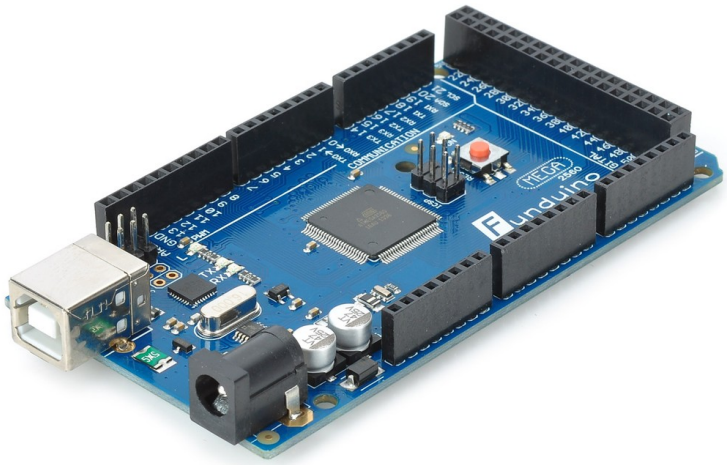

Figure 30: Arduino Mega 2560 Rev3 - The Body Control Module (CCM)

- analog Input Pins 16,
- interrupt pins 4

The Arduino Mega 2560 Rev3 was mainly selected because it has many digital I/O pins and also because it has 4 interrupt pins.

3.3.4 The vehicle Inertial Measerement Unit(IMU)

The inertial measurement unit (IMU) (Figure 33c is the most essential part of the vehicle, since the camber angle control is mostly based on data coming from the IMU gyroscope and accelerometer. The MPU 6050 was used as the IMU of the car and its specifications follow:

- power supply: 4.3 - 9V,
- communication protocol: I2C,
- gyroscope range: +/-250, +/-500, +/-1000, +/-2000 degs/s,
- acceleration range: +/-2g, +/-4g, +/-8g, +/-16g

3.3.5 The vehicle electric motor

For the vehicle movement, the electric dc motor of Figure 31b was used, mostly because of its simplicity and the low cost.

3.3.6 The electric motor controller

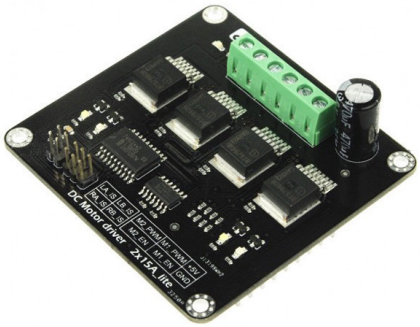

(a) The electric motor controller

(b) The electric motor of vehicle propulsion system

The motor controller used is shown in Figure 31a. It contains a simple H-Bridge driver, it has a wide input voltage range and is fully compatible with Arduino microcontroller. The controller specifications follow;

- input voltage range: 4.8 - 35V,
- max output current: 15A@13.8V max output current,
- peak output current: 20A @ 13.8V per channel,
- galvanic isolation to protect the microcontroller

3.3.7 The step down DC-DC converter

The step down DC-DC converter shown in Figure 32a, was used to supply power to the Raspberry Pi microcomputer and the camber angle control servo mechanism. The converter specifications follow:

- input voltage range: 9 - 35V,
- constant output voltage: 5V,
- maximum output current: 5A

3.3.8 The servo mechanism

Two servo motors Futaba S3003 were used for the steering and camber angle adjustment mechanisms. The specifications follow:

- Torque: 4.8V $\Rightarrow$ 44.00 oz-in (3.17 kg-cm), 6.0V $\Rightarrow$ 57.00 oz-in (4.10 kg-cm)

- Speed: 4.8V $\Rightarrow$ 0.23 sec/60^o, 6.0V $\Rightarrow$ 0.19 sec/60^o
- rotational range: 60^o,
- pulse cycle: 30 ms,
- pulse width: 500-3000 μs

3.3.9 The vehicle longitudinal velocity sensor

For the vehicle longitudinal velocity measurement, the combination of the photo interrupter sensor shown in Figure 33a and the encoder wheel shown in Figure 33b was used.

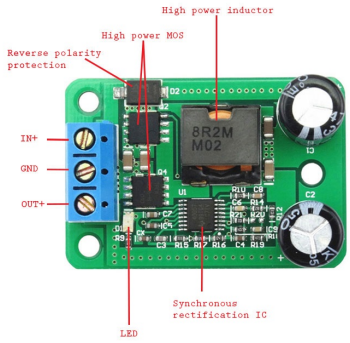

(a) The DC-DC converter

(b) The servo mechanism

Figure 32

(a) Photo Interrupter Sensor

(b) Encoder Wheel - 24mm

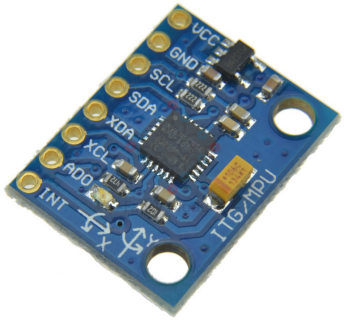

(c) The vehicle IMU

Figure 33

3.3.10 The electronics schematic

In Figure 34, the detailed electronics schematic of the proposed active control system is presented.

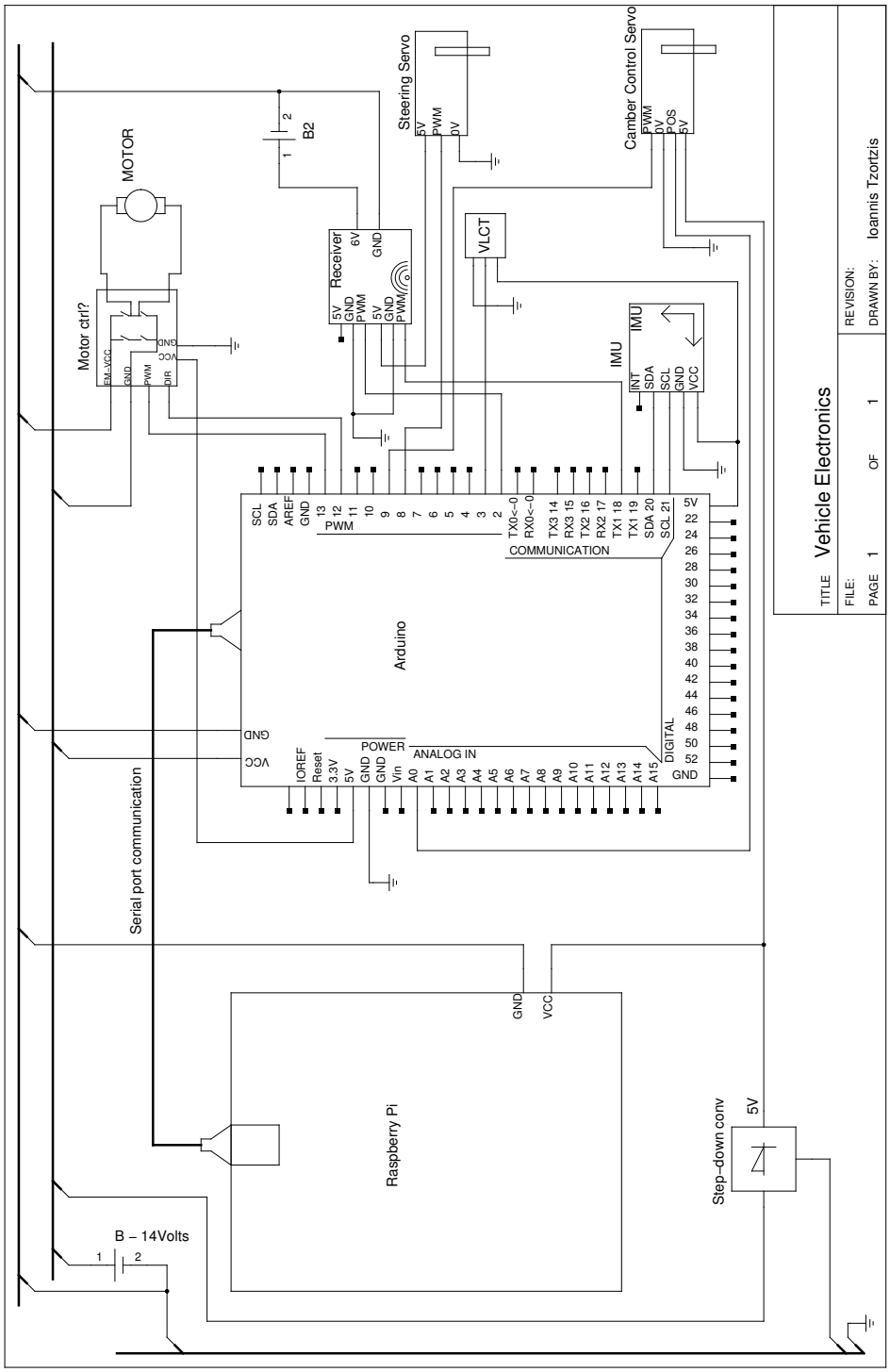

Figure 34: The electronics schematic

3.4 The camber angle control mechanism

3.4.1 The vehicle suspension system

In Figure 35, the front view of the vehicle suspension system is presented, while in Figure 36 the top view is shown. Each wheel is attached to the body with two arms, the upper and the lower. The lower arm has a wishbone structure, while the upper one is a simple tie rod. In Figure 35, the front wheels are set to have 0^o camber angle with respect to the body.

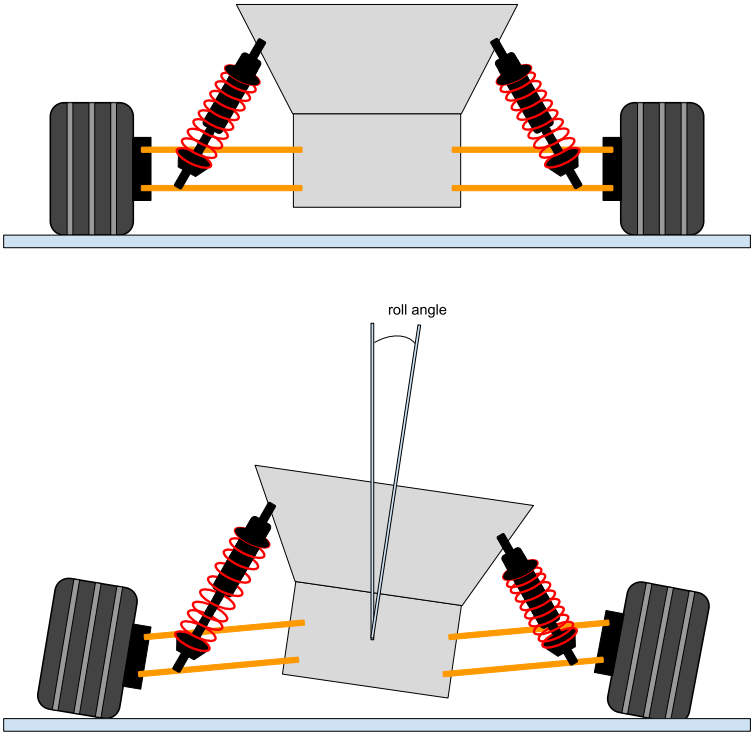

Figure 35: Front view - The default suspension system of the vehicle

Thus, when the vehicle travels through a corner in high speed, the body acquires roll angle and respectively the wheels gain non zero camber angle with respect to the ground. As a result, the grip is being reduced, especially to the outer wheel (in this case the outer wheel is the one on the right).

3.4.2 An alternative suspension system configuration

As already descibed, a common, alternative configuration which is also allowed by the structure of the prototype vehicle suspension system structure, is the positioning of the wheels in a negative camber angle configuration. This alternative configuration is presented in Figure 37. As shown, the benefit is that the outer wheel gains full contact with the ground, so the grip is being maximized. In contrast, the inner wheel grip is being reduced, even more than the default 0^o camber angle configuration. Moreover, this configuration has negative effects during acceleration and braking conditions of the vehicle.

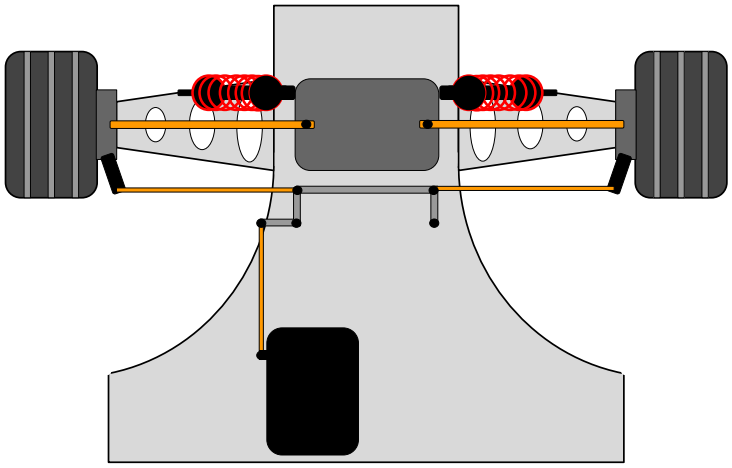

Figure 36: Top view - The default suspension system of the vehicle

3.4.3 The proposed mechanism

For the implementation of the proposed system, an appropriate mechanism should be installed for the adjustment of the camber angle of the front wheels. The prototype mechanism is presented in Figure 39. The concept of the new mechanism follows.

- two vertical rotating rods added to the body of the prototype vehicle,
- the vertical rods are connected with a horizontal rod installed on their upper side,
- the wheels tie rods are not attached statically to the vehicle body any more. They are now connected to the lower side of the newly installed, vertical, rotating rods.
- the rotation of the vertical rods is small, between -15^o and $+15^o$, so the movement of the wheels tie rods is considered to be linear.

3.4.4 Calculating the camber angle mechanism ratio

Due to the geometry of the proposed mechanism (Figure 40), there is a ratio between the angle of the actuating servo mechanism and the actual camber angle of the wheel with respect to the vehicle body. The determination of the relation between the two angles is necessary for both the mathematical modelling of the vehicle and the control algorithm developement. This relation is important because the system algorithm should control the wheel camber angle with respect to the vehicle body. Though, it controls and gets feedback directly from the servo mechanism. According to the proposed mechanism geometry, the following equations occur.

$$sin(\phi) = \frac{x_1}{l_c} \Rightarrow x_1 = l_c sin(\phi) \tag{21}$$

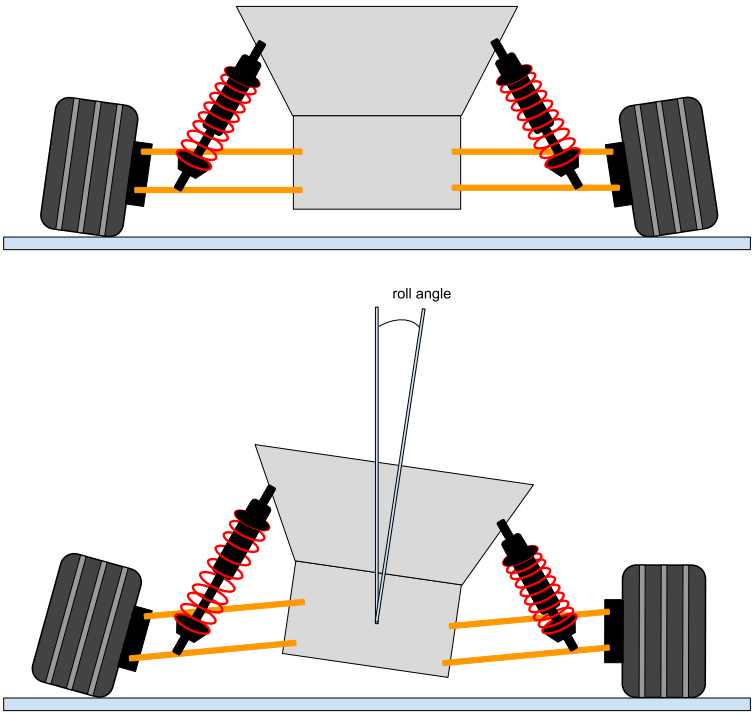

Figure 37: Negative camber angle configuration

$$sin(\phi_1) = \frac{x_2}{l_{cs}} \overset{x_1=x_2}{\Rightarrow} sin(\phi_1) = \frac{x_1}{l_{cs}} \Rightarrow \phi_1 = sin^{-1}(\frac{x_1}{l_{cs}}) \tag{22}$$

$$sin(\phi_1) = \frac{x_3}{l_c} \Rightarrow x_3 = l_c sin(\phi_1) \tag{23}$$

$$tan(\gamma_b) = \frac{x_3}{l_w} \Rightarrow \gamma_b = tan^{-1}(\frac{x_3}{l_w}) \tag{24}$$

Finally, by combining all the related equations ((21),(22),(23), (24)), the relation between the angles ϕ and γ_b is represented by the Equation 25.

$$\gamma_b = tan^{-1}(\frac{l_c sin(sin^{-1}(\frac{l_c sin(\phi)}{l_{cs}})}{l_w}) \tag{25}$$

The final relation between the CCS servo angle and the wheel steering angle is presented in Figure 41. The relation is not linear due to the several rotating links shown in Figure 40. Though, the relation is considered to be linear in the effective range from -0.25 rad to 0.25 rad.

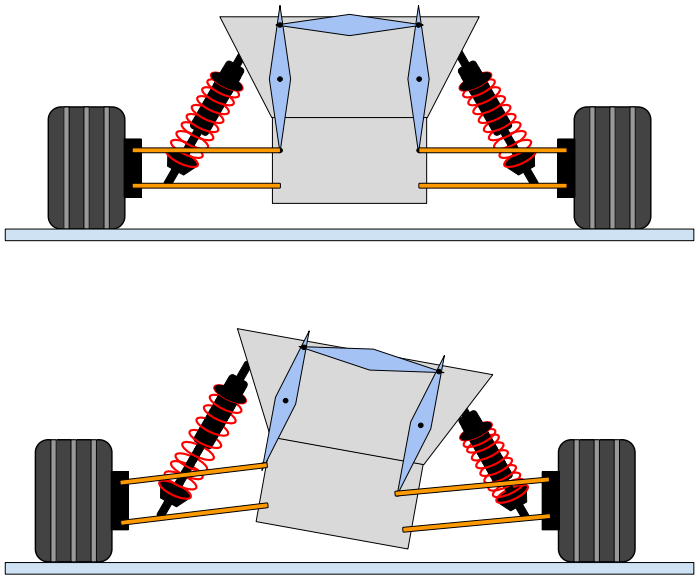

Figure 38: Front view of the camber angle control prototype mechanism

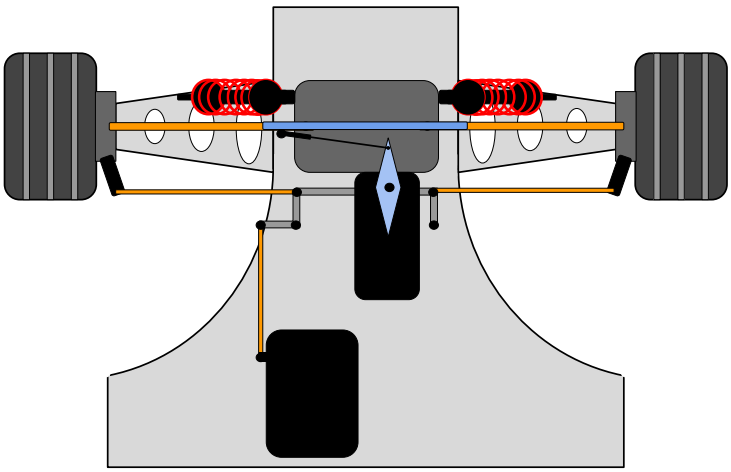

Figure 39: Top view of the camber angle control prototype mechanism

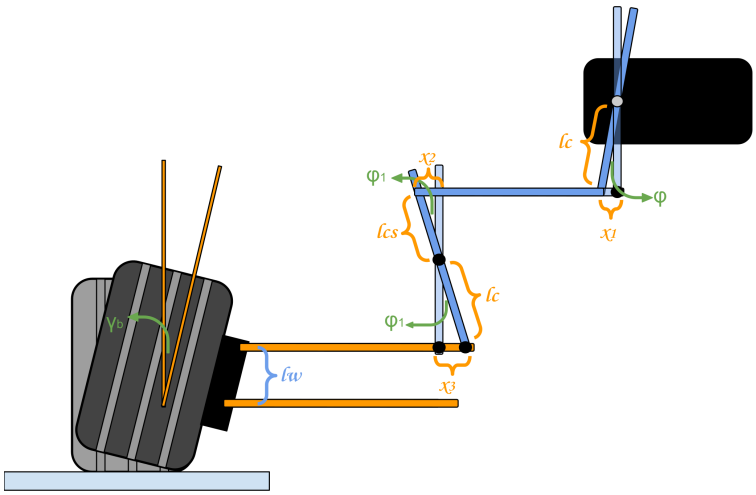

Figure 40: Front view - Analysis of the mechanism geometry

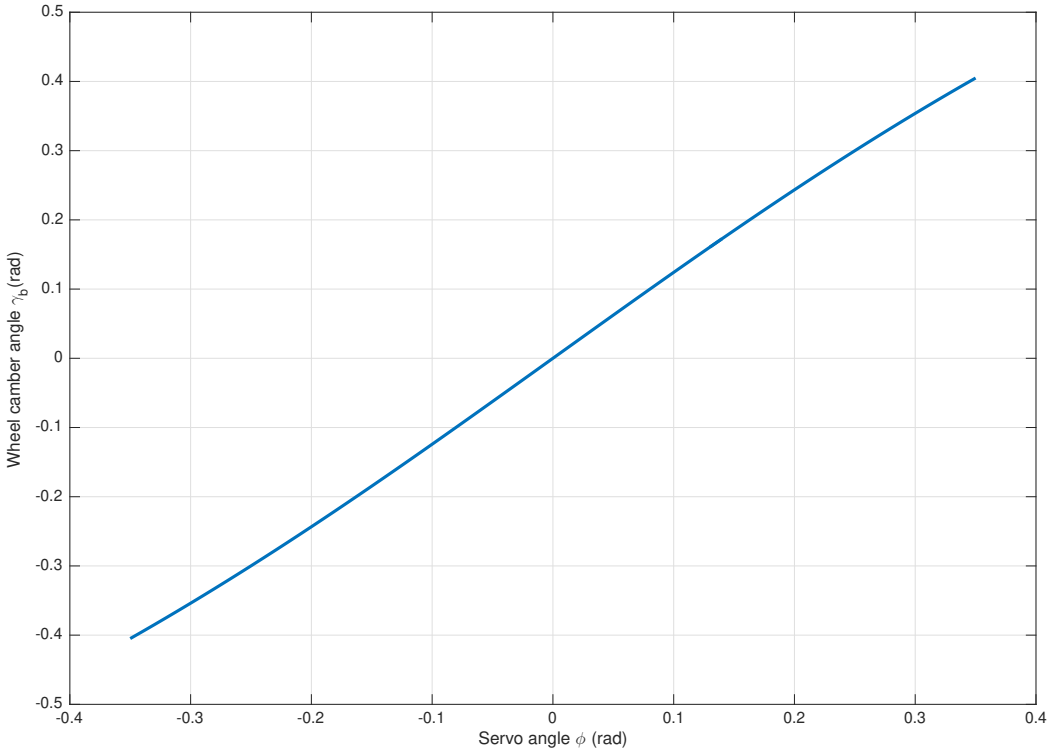

Figure 41: The relation between servo angle and the wheel camber angle with respect to the vehicle body.

3.5 The control algorithm

A simple concept was designed for the algorithm that feeds the CCS servo with the desired angle. It was decided that the CCS would control the servo mechanism only when the yaw rate exceeds a predefined limit (50 degs/s). The system reads the yaw rate in real time and checks if it is higher than 50 degs/s. If that is true, then the algorithm applies a scaling factor (0.1 to 0.2) to calculate the CCS servo angle. Moreover, the algorithm sets a limit to the desired camber angle, so it cannot exceed the absolute value of 15 degrees. If the yaw rate is lower than 50 degs/s, the algorithm sets the desired camber angle to zero. The flowchart of the algorithm concept is presented in Figure 42.

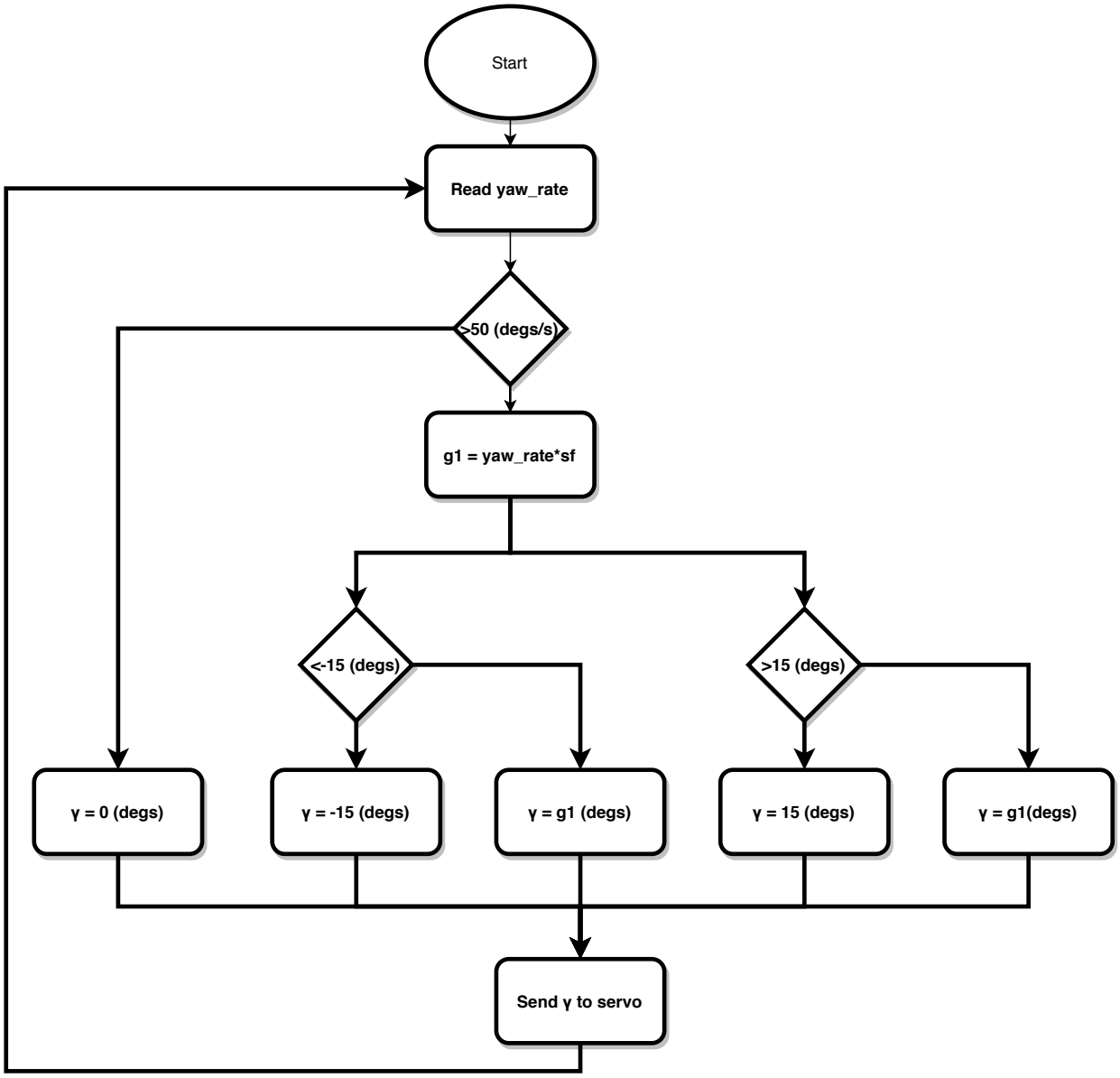

Figure 42: The flowchart of the system algorithm

3.6 The vehicle model

3.6.1 The linear single track model

For the mathematical modelling of the vehicle lateral dynamics, the simple linear single track model [12] was chosen. According to the principle of this model, also known as bicycle model, the car is assumed to behave as a single track vehicle (Figure 43). So, the outer and the inner wheel are merged to one, for both the front and rear axles.

As shown in Figure 43, F_{yr} and F_{yf} are the lateral forces exerting on the rear and front wheel respectively. The vector v represents the velocity of the vehicle body, and it consists of the longitudinal v_x and lateral velocity v_y. The angle formed by the velocity vector v and the horizontal x-axis, is called slip angle and its symbol is β. The slip angle is defined as the difference between the direction of the vehicle body heading and the direction of the vehicle body travel. The angles α_r and α_f are the slip angles of the rear and front wheel respectively.

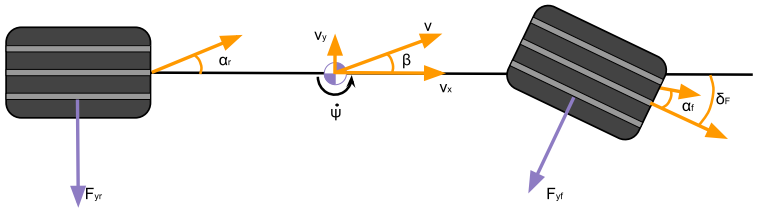

Figure 43: The single track model - Bicycle model

At low slip angles, the relationship between lateral forces and wheel slip angles is linear as described in [2]. The

$$\begin{cases} F_{yr} = C_{ar}\alpha_r \\ F_{yf} = C_{af}\alpha_f \end{cases} \tag{26}$$

Where C_{af} and C_{ar} represent the cornering stifness on the front and rear axis respectively. The Newton's second law yields the equations of motion for the vehicle lateral movement.

$$\left.\begin{array}{l} ma_y = \Sigma F_y \\ T_z = I_z\dot{\psi} \end{array}\right\} \Rightarrow \left.\begin{array}{l} m(v_x\dot{\psi} + \dot{v_y}) = F_{yf}cos(\delta_F) + F_{yr} \\ I_z\ddot{\psi} = l_f F_{yf}cos(\delta_F) + l_r F_{yr} \end{array}\right\} \tag{27}$$

From the single track model geometry analysis, the following relations occur.

$$\left.\begin{array}{l} tan(\delta_F - \alpha_f) = \dfrac{v_y + l_f\dot{\psi}}{v_x} \\ tan(\alpha_r) = \dfrac{-v_y + l_r\dot{\psi}}{v_x} \\ tan(\beta) = \dfrac{v_y}{v_x} \end{array}\right\} \tag{28}$$

Assuming small slip angle β, the equality $tan(\beta) = \beta$ could be considered as valid. As a result:

$$(28) \Rightarrow \begin{cases} \alpha_f = \delta_F - \beta - \frac{l_f \dot{\psi}}{v_x} \\ \alpha_r = -\beta + \frac{l_r \dot{\psi}}{v_x} \\ \beta = \frac{v_y}{v_x} \end{cases} \tag{29}$$

Due to the nature of the experiments held for the proof of concept, the slip angle was so small that was considered to be equal to zero for the purpose of the modelling ($\beta = 0$). Additionally

$$\beta = \frac{v_y}{v_x} \Rightarrow v_y = \beta v_x \Rightarrow \dot{v}_y = \frac{d}{dt}(\beta v_x) = \dot{\beta} v_x + \beta \dot{v}_x \tag{30}$$

So

$$(27) \overset{(26)}{\Rightarrow} \left.\begin{array}{l} m(v_x \dot{\psi} + \dot{v}_y) = C_{af}\alpha_f cos(\delta_F) + C_{ar}\alpha_r \\ I_z \ddot{\psi} = l_f F_{yf} + l_r F_{yr} \end{array}\right\} \overset{(30)}{\Rightarrow}$$

$$\left.\begin{array}{l} m(v_x \dot{\psi} + \dot{\beta} v_x + \beta \dot{v}_x) = C_{af}\alpha_f + C_{ar}\alpha_r \\ I_z \ddot{\psi} = l_f C_{af}\alpha_f + l_r C_{ar}\alpha_r \end{array}\right\} \overset{(29)}{\Rightarrow}$$

$$\left.\begin{array}{l} m(v_x \dot{\psi} + \dot{\beta} v_x + \beta \dot{v}_x) = C_{af}(\delta_F - \beta - \frac{l_f \dot{\psi}}{v_x}) + C_{ar}(-\beta + \frac{l_r \dot{\psi}}{v_x}) \\ I_z \ddot{\psi} = l_f C_{af}(\delta_F - \beta - \frac{l_f \dot{\psi}}{v_x}) + l_r C_{ar}(-\beta + \frac{l_r \dot{\psi}}{v_x}) \end{array}\right\} \overset{\beta=0}{\Rightarrow}$$

$$\left.\begin{array}{l} m v_x \dot{\psi} = C_{af}(\delta_F - \frac{l_f \dot{\psi}}{v_x}) + C_{ar}\frac{l_r \dot{\psi}}{v_x} \\ I_z \ddot{\psi} = l_f C_{af}(\delta_F - \frac{l_f \dot{\psi}}{v_x}) + l_r C_{ar}\frac{l_r \dot{\psi}}{v_x} \end{array}\right\} \tag{31}$$

The basic equation that was used for the modelling of the vehicle lateral dynamics is the Equation 32. This equation is a relation between the driver inputs, accelerating and steering commands (v_x and δ_F), and the vehicle behavior (yaw rate $\dot{\psi}$).

According to the [14], camber angle on a wheel will produce a lateral force known as "camber thrust". This lateral force has the form of the Equation 33, where C_γ represents the camber angle changing stifness of the wheel and γ is the camber angle of the wheel with respect to the ground. The influence of this lateral force should be added to the Equation 32. The final equation used for the simulation of the vehicle lateral dynamics is the Equation 34.

$$m u_x \dot{\psi} = C_{af}\delta_F - \frac{C_{af} l_f}{v_x}\dot{\psi} + \frac{C_{ar} l_r}{v_x}\dot{\psi}$$

$$\dot{\psi} = \frac{C_{af}\delta_F}{m v_x + \frac{C_{af} l_f}{v_x} - \frac{C_{ar} l_r}{v_x}} \tag{32}$$

$$F_{y\gamma} = C_\gamma \gamma \tag{33}$$

$$\dot{\psi} = \frac{C_{af}\delta_F + C_\gamma \gamma}{m v_x + \frac{C_{af} l_f}{v_x} - \frac{C_{ar} l_r}{v_x}} \tag{34}$$

3.6.2 The validation of the model

For the validation of the vehicle lateral dynamics model, experimental results from the vehicle testing were used. During the basic experiment, the prototype vehicle starts a counterclockwise circular maneuver (green circle in Figure 44) with constant longitudinal velocity and constant steering. After some spins, the vehicle escapes the former maneuver (orange route in Figure 44) and follows a clockwise circular maneuver (blue circle in Figure 44) with constant longitudinal velocity and constant steering.

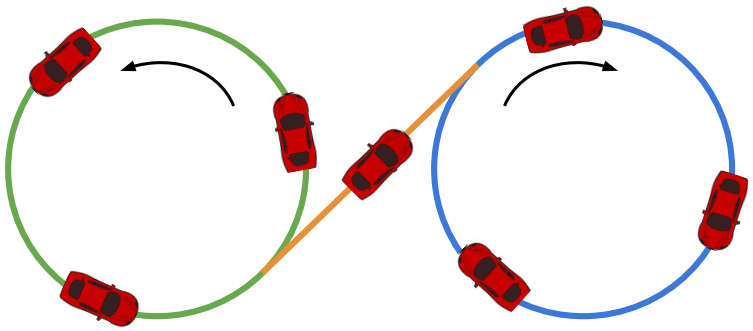

Figure 44: Successive circular maneuvers experiment

In Figure 45, the first two graphs present the results from the driver's inputs, the longitudinal velocity profile and the front wheels steering profile. The third graph shows the lateral behaviour of the vehicle expressed by the yaw rate. The velocity is measured by the photo interrupter sensor shown in Figure 33a. The front wheels steering angle is calculated by using the driver steering command and the ratio between steering servo mechanism and the wheel. The yaw rate is being measured by the vehicle inertial measurement unit (IMU) (Figure 33c).

In the first graph of Figure 46, the comparison of the experimental yaw rate curve along with the simulated one is presented. Even though the bicycle model is a linear approach, the final approximation of the yaw rate curve is satisfactory and fully suitable for the purposes of this thesis. The validity of the model was also confirmed using the results of the alternative type of experiment shown in Figures 47, 48. During this experiment, the vehicle follows an automated sinusoidal steering command.

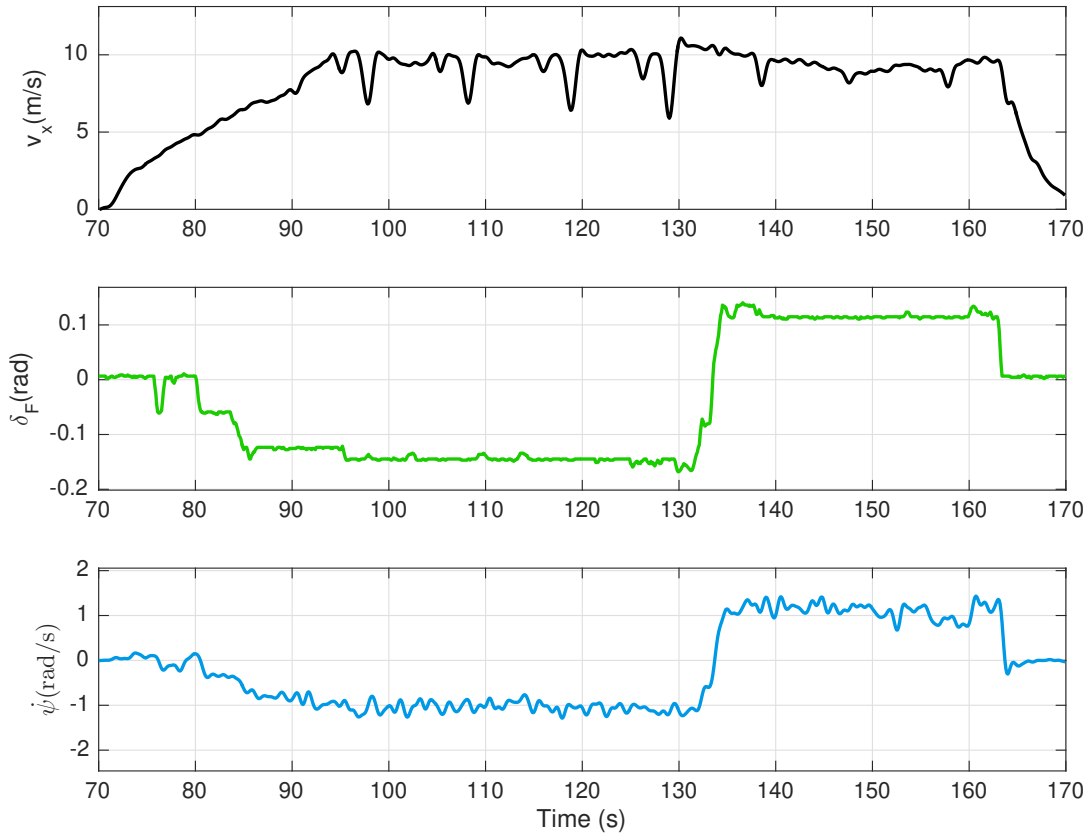

Figure 45: Successive circular maneuvers experiment - Vechicle movement

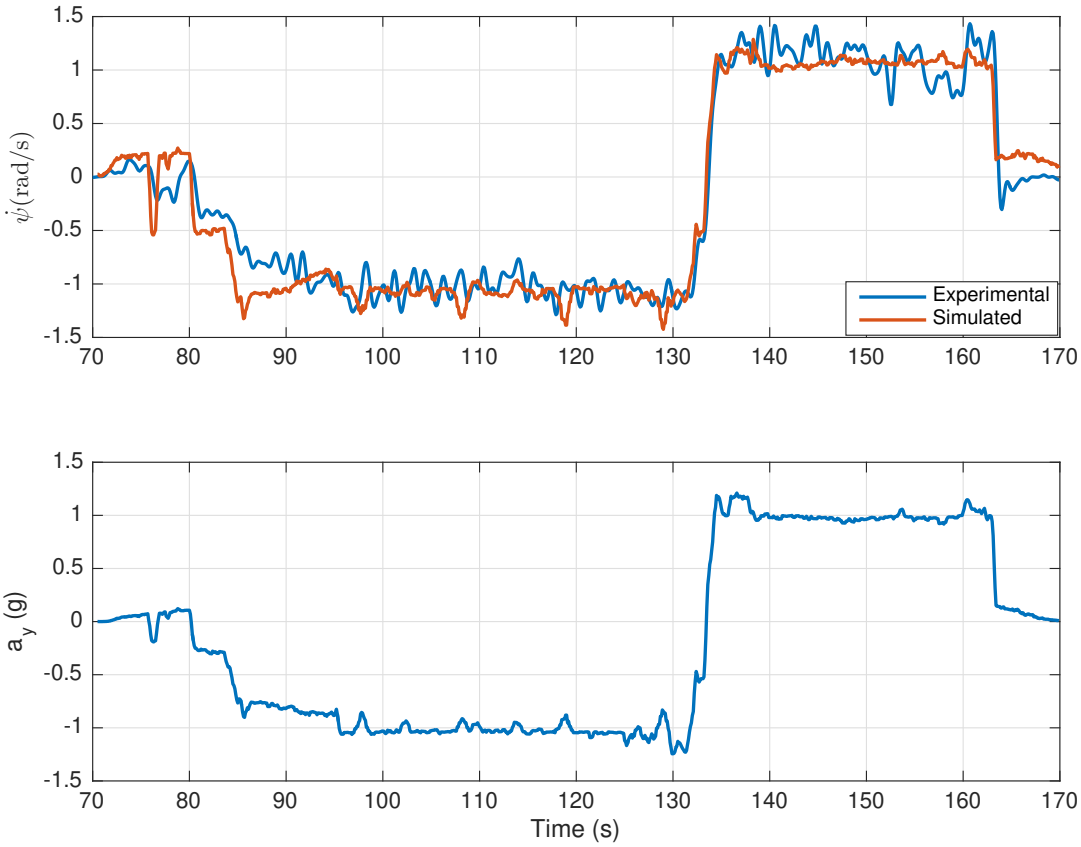

Figure 46: Comparison: experimental/simulated yaw rate

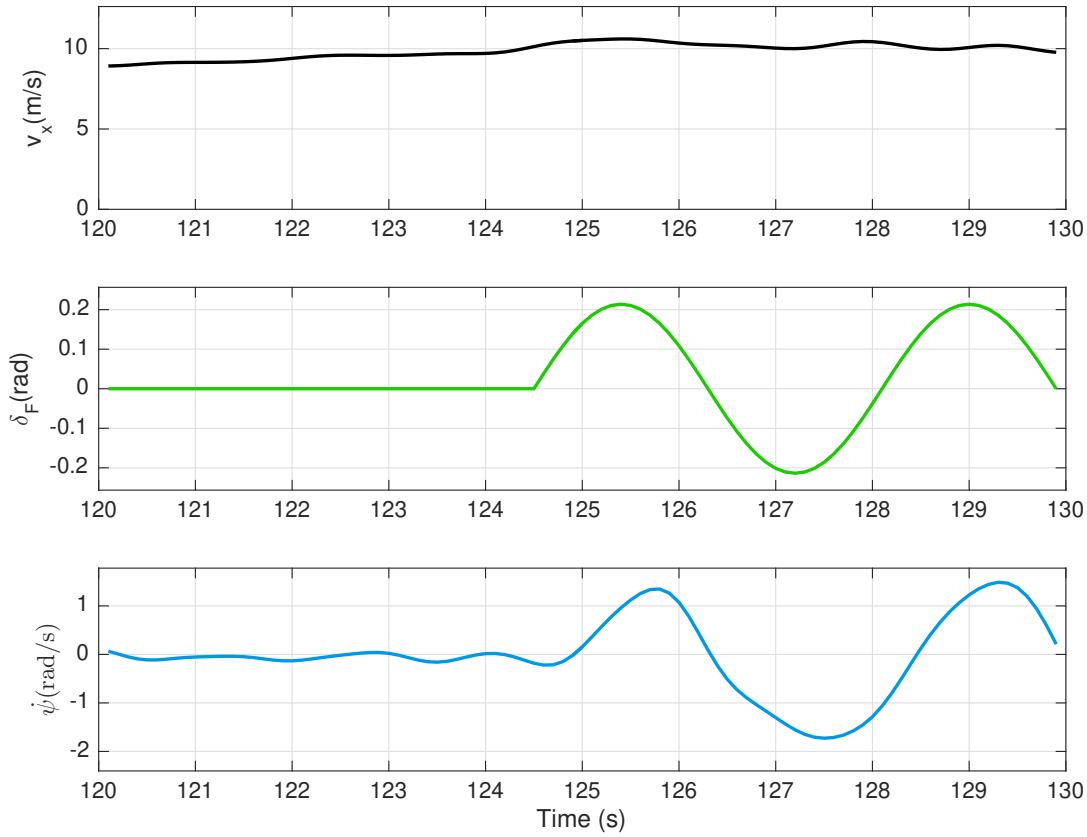

Figure 47: Sinusoidal maneuver experiment

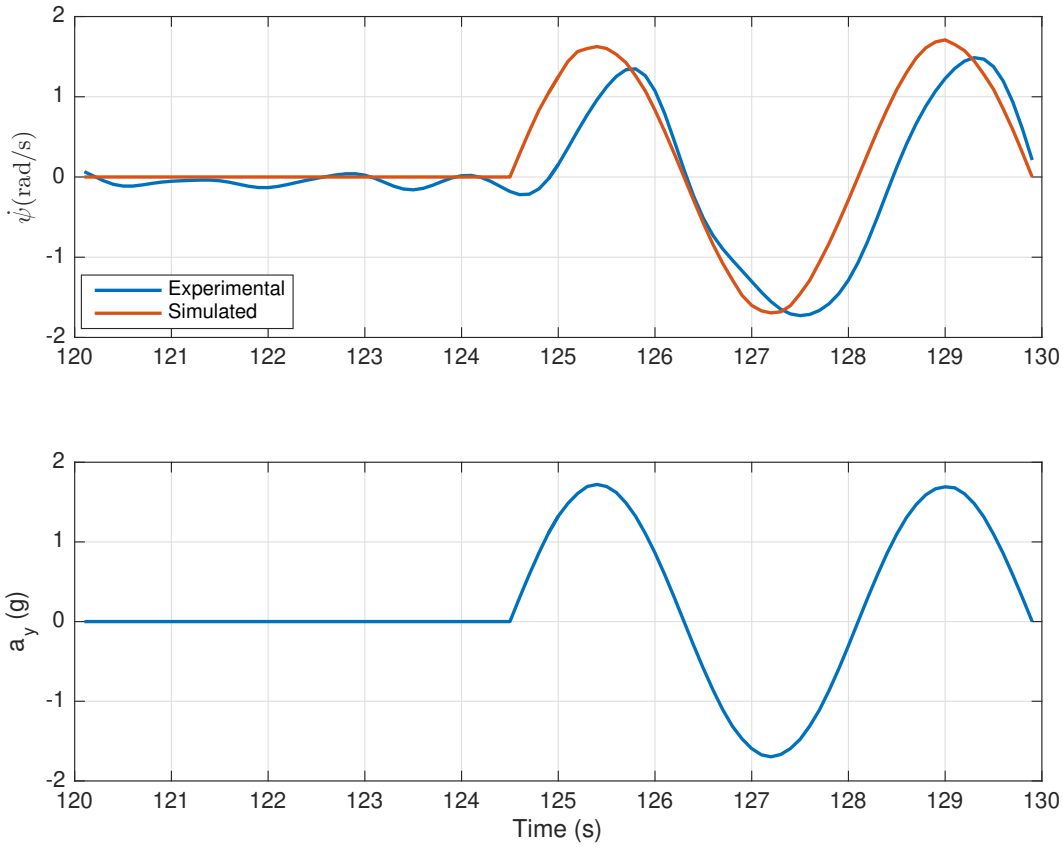

Figure 48: Comparison: experimental/simulated yaw rate

3.6.3 Calculating the steering system ratio

For the exact calculation of the wheel steering angle δ_F using the steering servo angle, the ratio of the steering system should be defined. The structure of the steering system is presented in Figure 49.

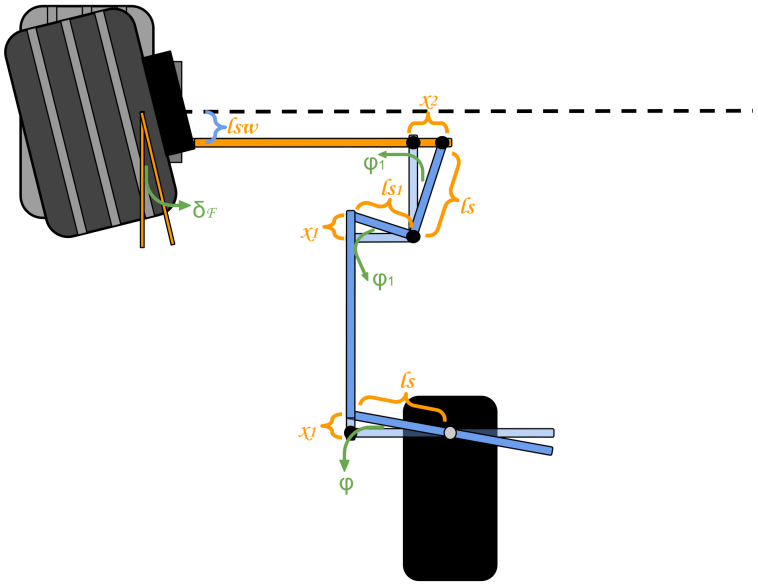

Figure 49: Top view - The steering system structure

By analyzing the geometry of the steering system, the following relations occur.

$$sin(\phi) = \frac{x_1}{l_s} \Rightarrow x_1 = l_s sin(\phi) \tag{35}$$

$$sin(\phi_1) = \frac{x_1}{l_{s1}} \Rightarrow \phi_1 = sin^{-1}(\frac{x_1}{l_{s1}}) \tag{36}$$

$$sin(\phi_1) = \frac{x_2}{l_s} \Rightarrow x_s = l_s sin(\phi_1) \tag{37}$$

$$tan(\delta_F) = \frac{x_2}{l_{sw}} \Rightarrow \delta_F = tan^{-1}(\frac{x_2}{l_{sw}}) \tag{38}$$

Finally, by combining all the related equations ((35),(36),(37), (38)), the relation between the angles ϕ and δ_F is represented by the Equation 39.

$$\delta_F = tan^{-1}(\frac{l_s sin(sin^{-1}(\frac{l_s sin(\phi)}{l_{s1}})}{l_{sw}}) \tag{39}$$

The final relation between the steering servo angle and the wheel steering angle is presented in Figure 50. The relation is not linear due to the several rotating links shown in Figure 49. Though, the relation is considered to be linear in the effective range from -0.25 rad to 0.25 rad.

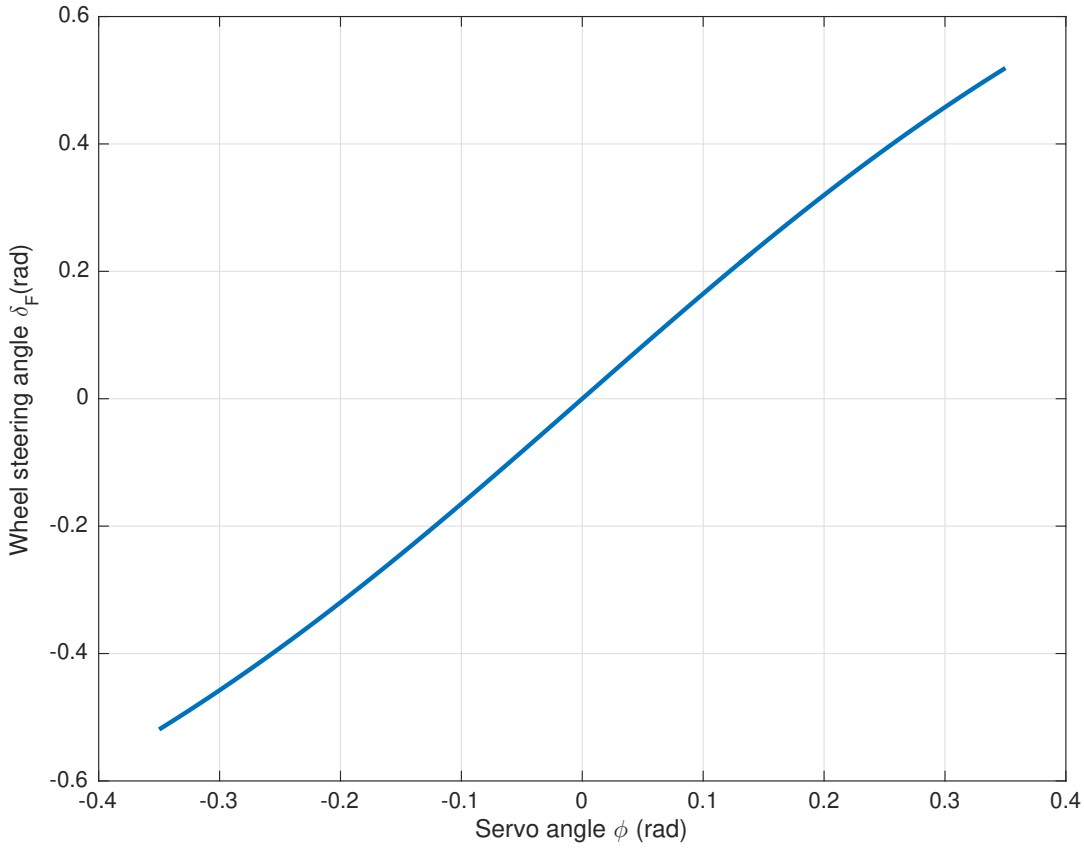

Figure 50: Relation between the steering servo angle and the wheel steering angle

3.7 The Matlab/Simulink model

The software Matlab/Simulink [6] was used for the modelling and simulation of the control system. The big block in Figure 51 represents the vehicle lateral dynamics, that is the single track linear model described in previous subsection. The vehicle characteristics block reads data from the Matlab workspace refering to several constants like chassis mass, cornering stifness coefficients, COG position etc. In camber control block lives the algorithm of the system that takes as imput the yaw rate of the vehicle and gives as output the reference angle of the CCS servo.

As shown in Figure 52, the servo mechanism is modelled as a first order transfer function, which practically ouputs a delayed version of the imput. A simple PD (only proportional and derivative parts were used) controller were used for the manipulation of the servo mechanism. After several trial and error testing the PD controller was successfully set.

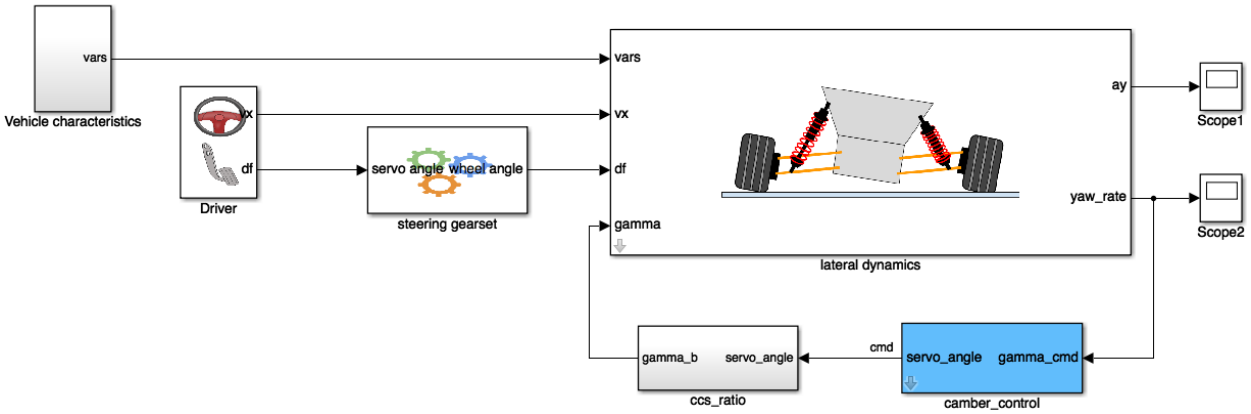

Figure 51: The Simulink model of the proposed system

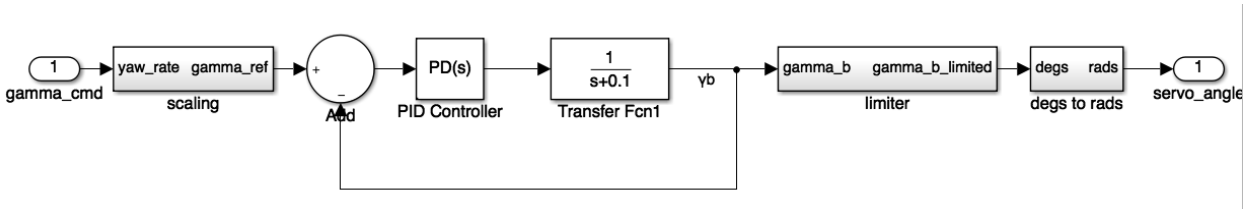

Figure 52: The camber controller block

Using the simlulink model, several simulations were performed. Based on the chosen experiments for the proof of concept, the counterclockwise circular test, the clockwise circular test and the sinusoidal steering test, the critical comparison between the passive and the active system is presented in Figure **??**.

For the circular tests (Figures 54, 55), the longitudinal velocity v_x and the steering angle δ_F are constant in the time period between the $3^r d$ and the $8^t h$ second, in which it is observed that there is an improvement in the yaw rate $\dot{\psi}$ and the lateral acceleration α_y curves. This observation is sufficient for the proof of concept, that the camber angle adjustment can provide better handling.

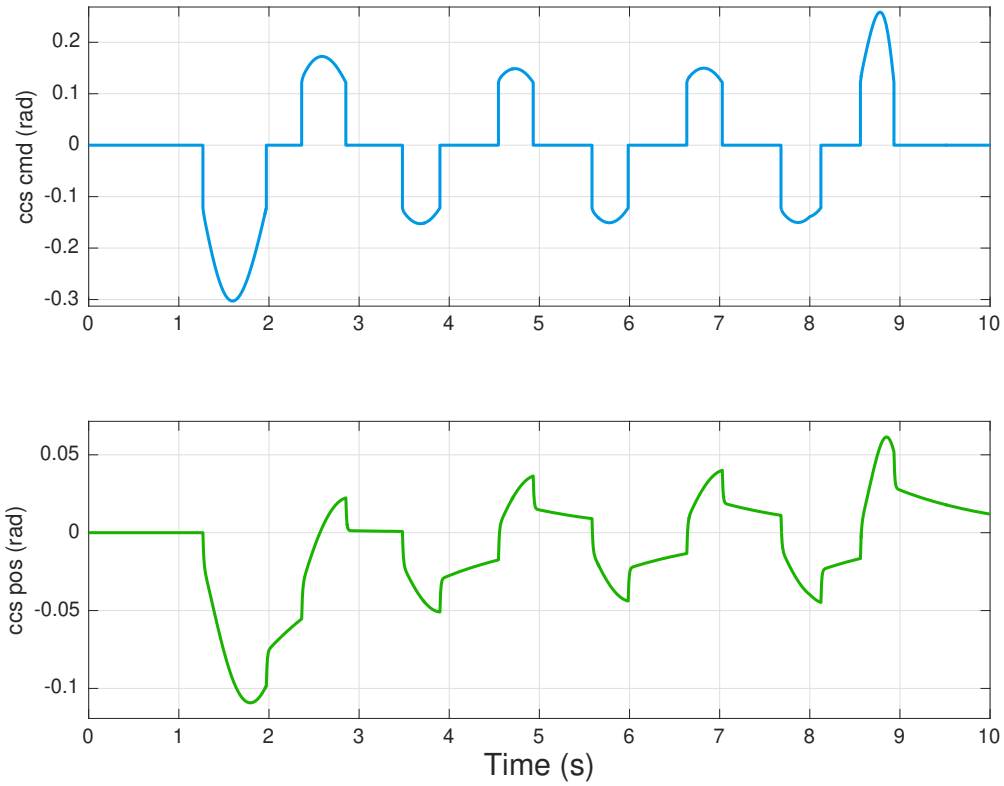

Figure 53: Simulated sinusoidal steering maneuver - CCS servo command and position signals

However, the results are different in the sinusoidal steering test shown in Figure 56. For this test, the longitudinal velocity is constant in the time interval from $3^r d$ to $8^t h$ second, while the steering angle follows a sinusoidal curve. There is an improvement in the yaw rate $\dot{\psi}$ and the lateral acceleration α_y curves, though it is slightly observable. This behaviour seems to be non reasonable but it can be explained using the CCS servo command and position signals presented in Figure 53. The high frequency of the sinusoidal steering signal in combination with delayed CCS servo response, do not allow the full scale camber angle adjustment. Thus, the camber angle is being changed slightly, so it does not influence effectively the lateral acceleration of the vehicle. Similar results occured from the real world experimentation and are presented in the following chapter. Several simulation results with different camber angle ratio can be found in the Appendix of this thesis.

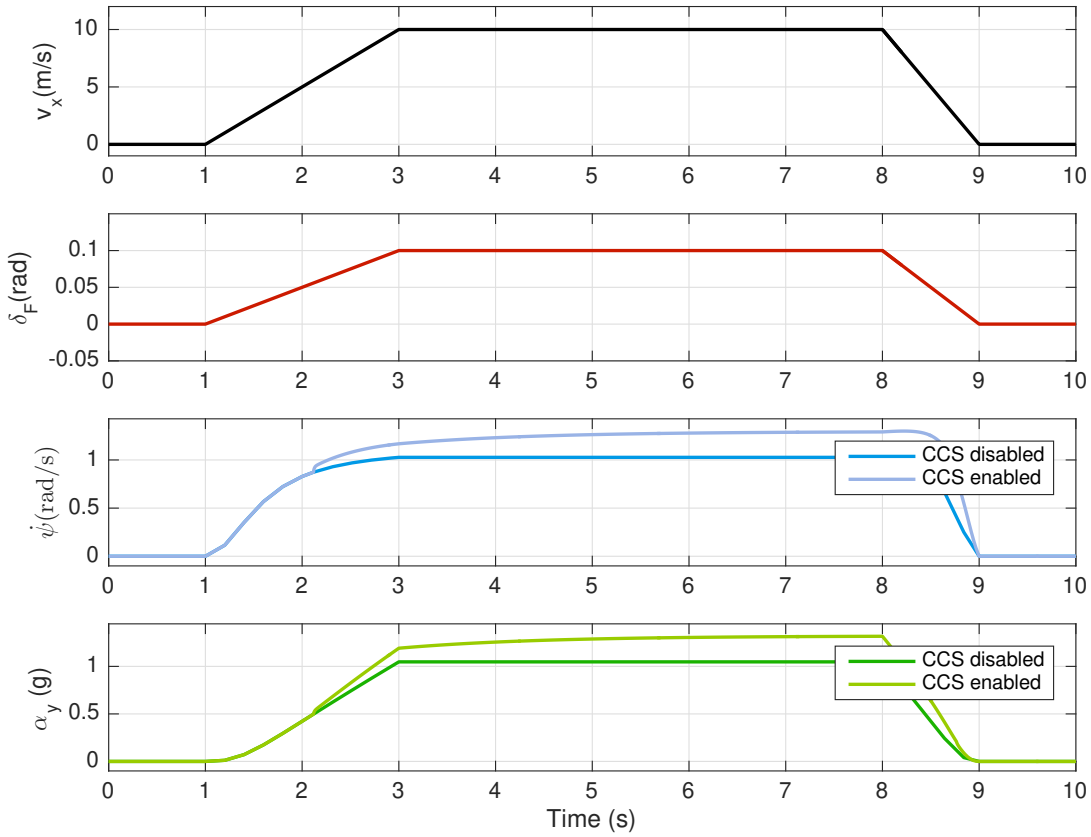

Figure 54: Simulated counterclockwise maneuver

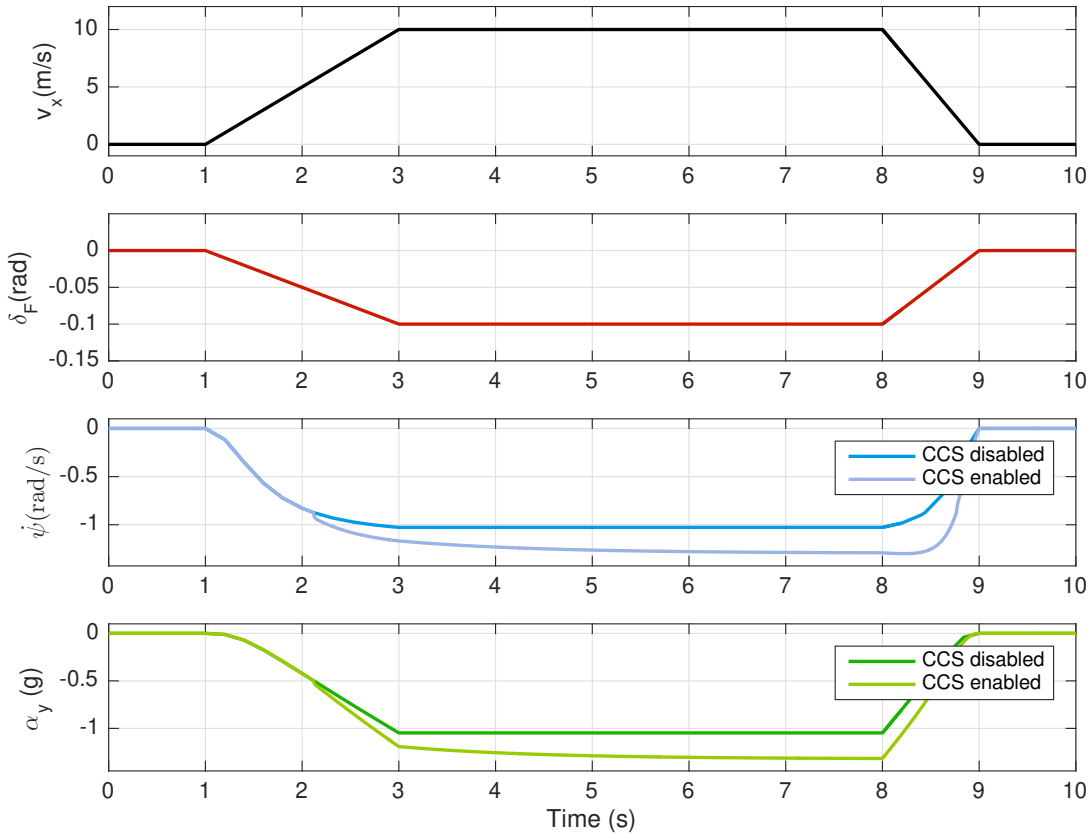

Figure 55: Simulated clockwise maneuver

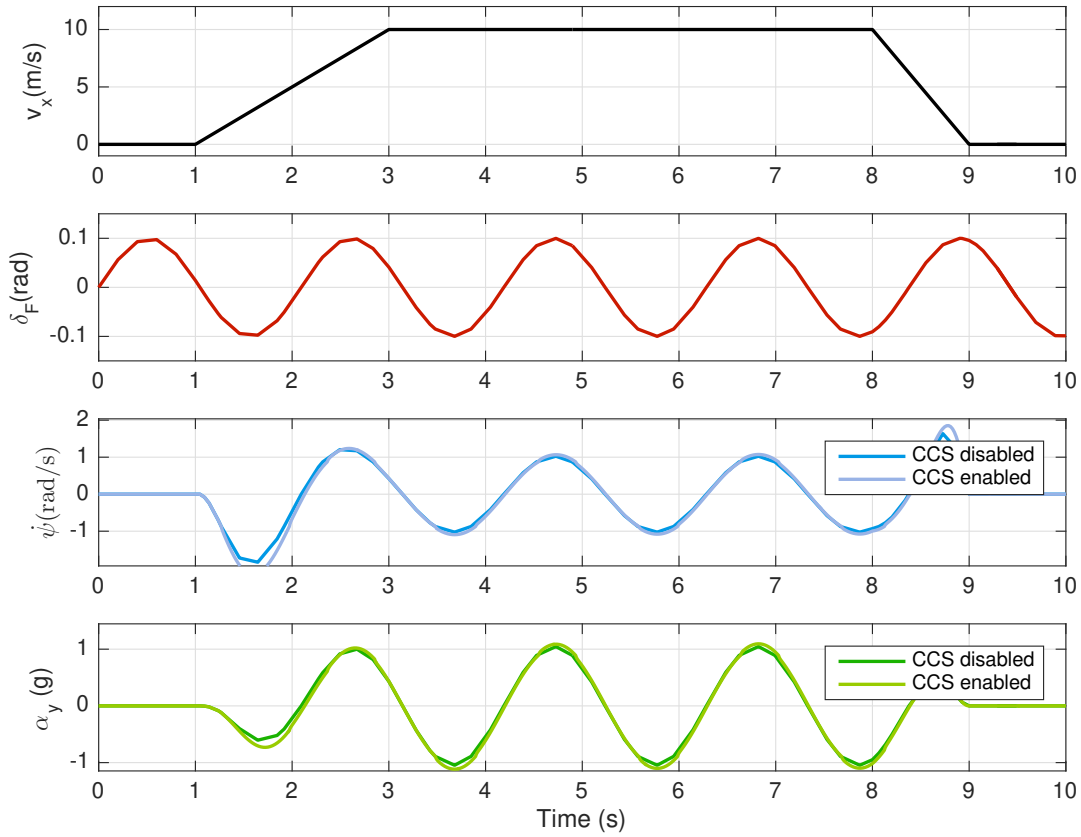

Figure 56: Simulated sinusoidal steering maneuver

4 Experimental results

4.1 Experimentation with CCS disabled

4.1.1 Counterclockwise circular maneuver with ccs disabled

In this experiment, the vehicle travels on a counterclockwise circular trajectory with the Camber Control System (CCS) disabled. The longitudinal velocity is constant and its value is almost 12m/s in the time interval from 10^{th} to 58^{th} second. In the same time period, the front wheels steering angle is constant and is almost equal to 0.18 rads. In Figure 57, longitudinal velocity v_x, wheel steering angle δ_F, vehicle yaw rate $\dot{\psi}$ and the lateral acceleration α_y are shown. As expected, the yaw rate and the lateral acceleration curves have similar shape, with the former to be around $1.1 rad/s$ and later in a range from 0.6 to 1g.

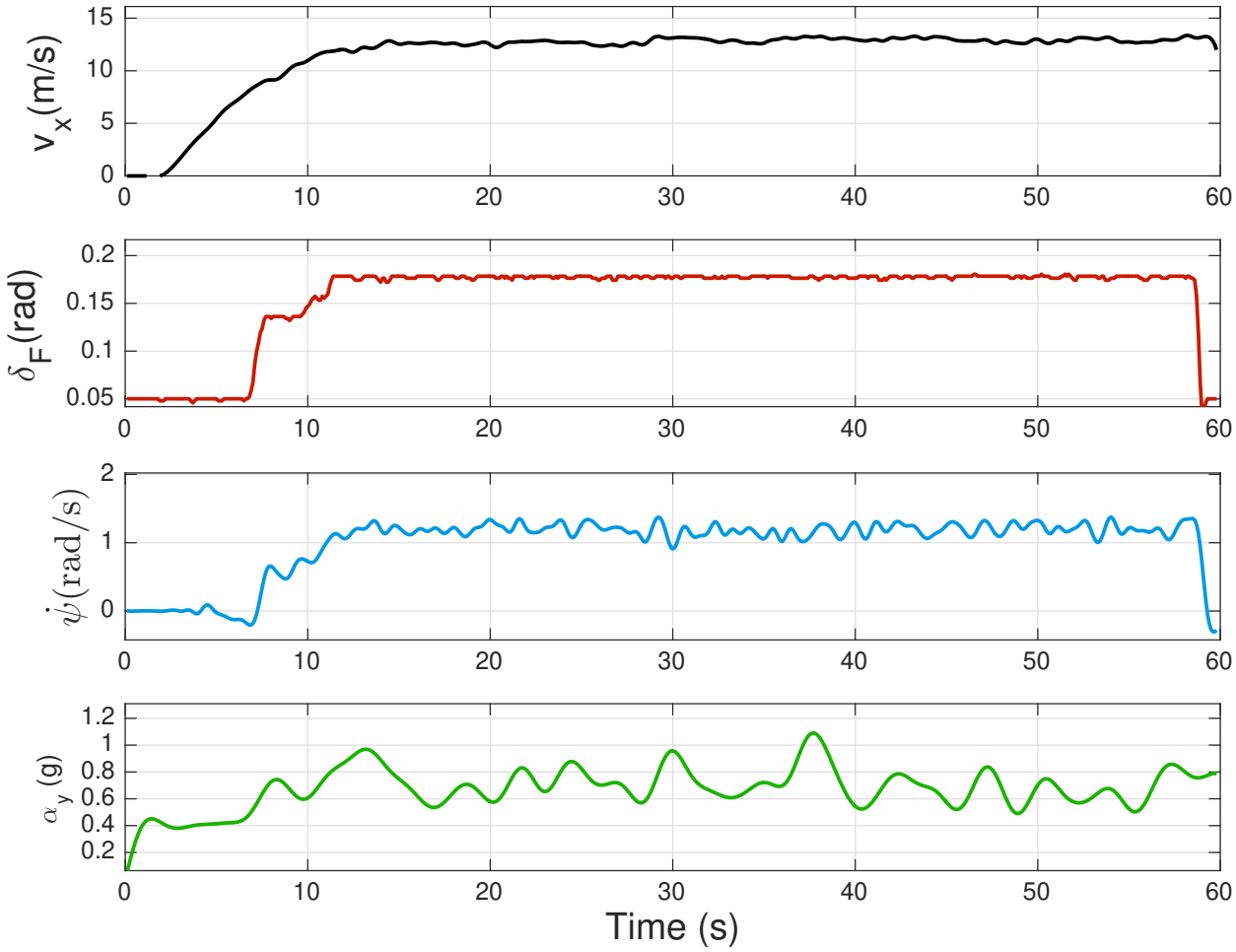

Figure 57: Left circular maneuver

4.1.2 Clockwise circular maneuver with ccs disabled

In this experiment, the vehicle travels on a clockwise circular trajectory with the Camber Control System (CCS) disabled. The longitudinal velocity is constant and its value is almost 12m/s in the time interval from 20^{th} to 78^{th} second. In the same interval, the front wheels steering angle is constant and is almost equal to -0.18 rads. The minus (-) sign expresses the clockwise direction of the steering. In Figure 58, longitudinal velocity v_x, wheel steering angle δ_F, vehicle yaw rate $\dot{\psi}$ and the lateral acceleration α_y are shown. As expected, the yaw rate and the lateral acceleration curves have similar shape, with the former to be around $1.1 rad/s$ and later in a range from 0.6 to 0.8g.

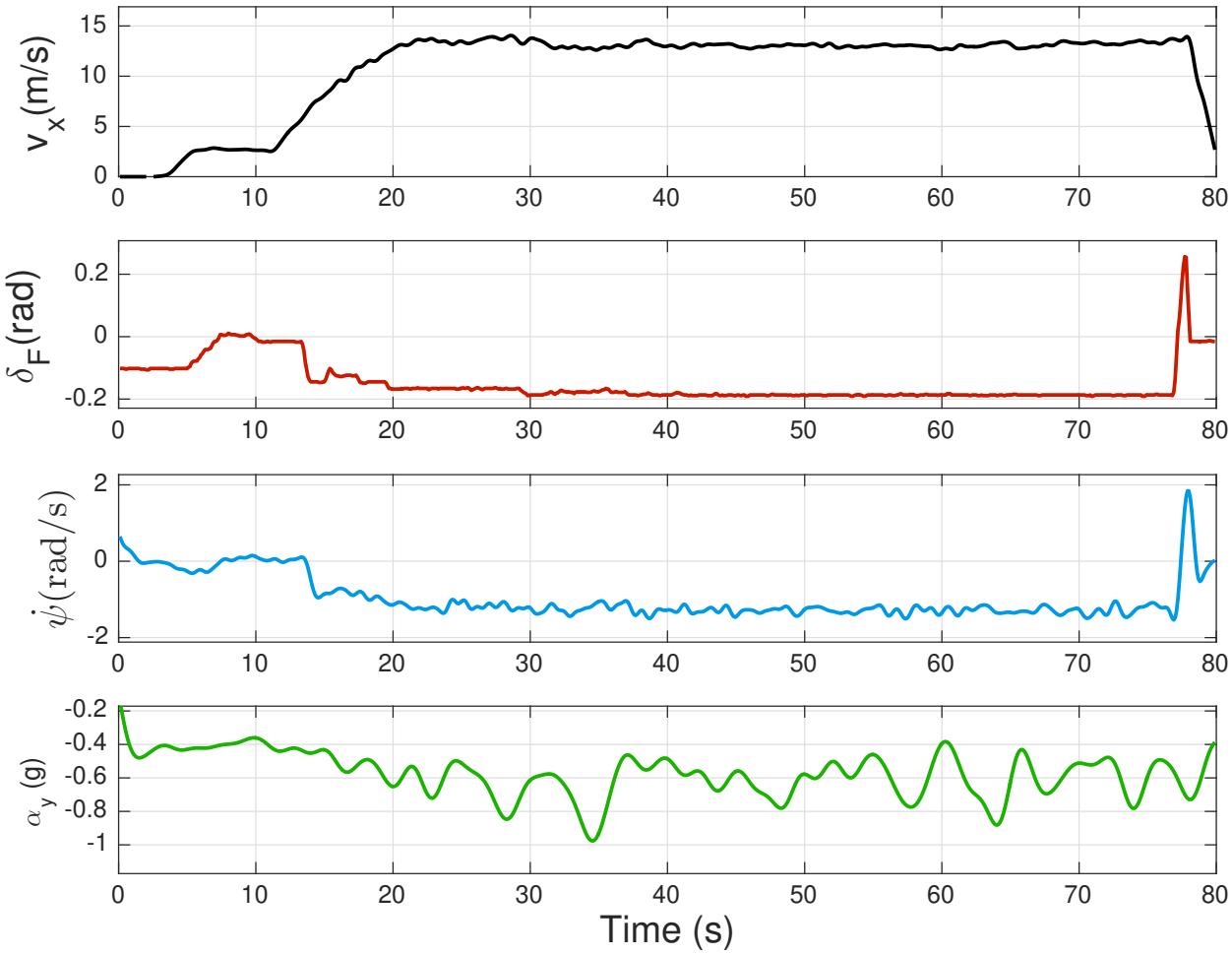

Figure 58: Right circular maneuver

4.1.3 Sinusoidal steering maneuver - CCS disabled

During this experiment, the vehicle travels on a sinusoidal trajectory with the Camber Control System (CCS) disabled. The longitudinal velocity is constant and its value almost equals to 12m/s. The front wheels steering angle follows a sinusoidal wave with aplitude almost equal to 0.18 rads (The minus (-) sign expresses the clockwise direction of the steering). In Figure 59, longitudinal velocity v_x, wheel steering angle δ_F, vehicle yaw rate $\dot{\psi}$ and the lateral acceleration α_y are shown. The absolute value of the lateral acceleration is not as high as in the circular experiments described before. That is due to the fact that the sinusoidal steering signal has high frequency and the CSS servo delayed response cannot adjust camber angle sufficiently.

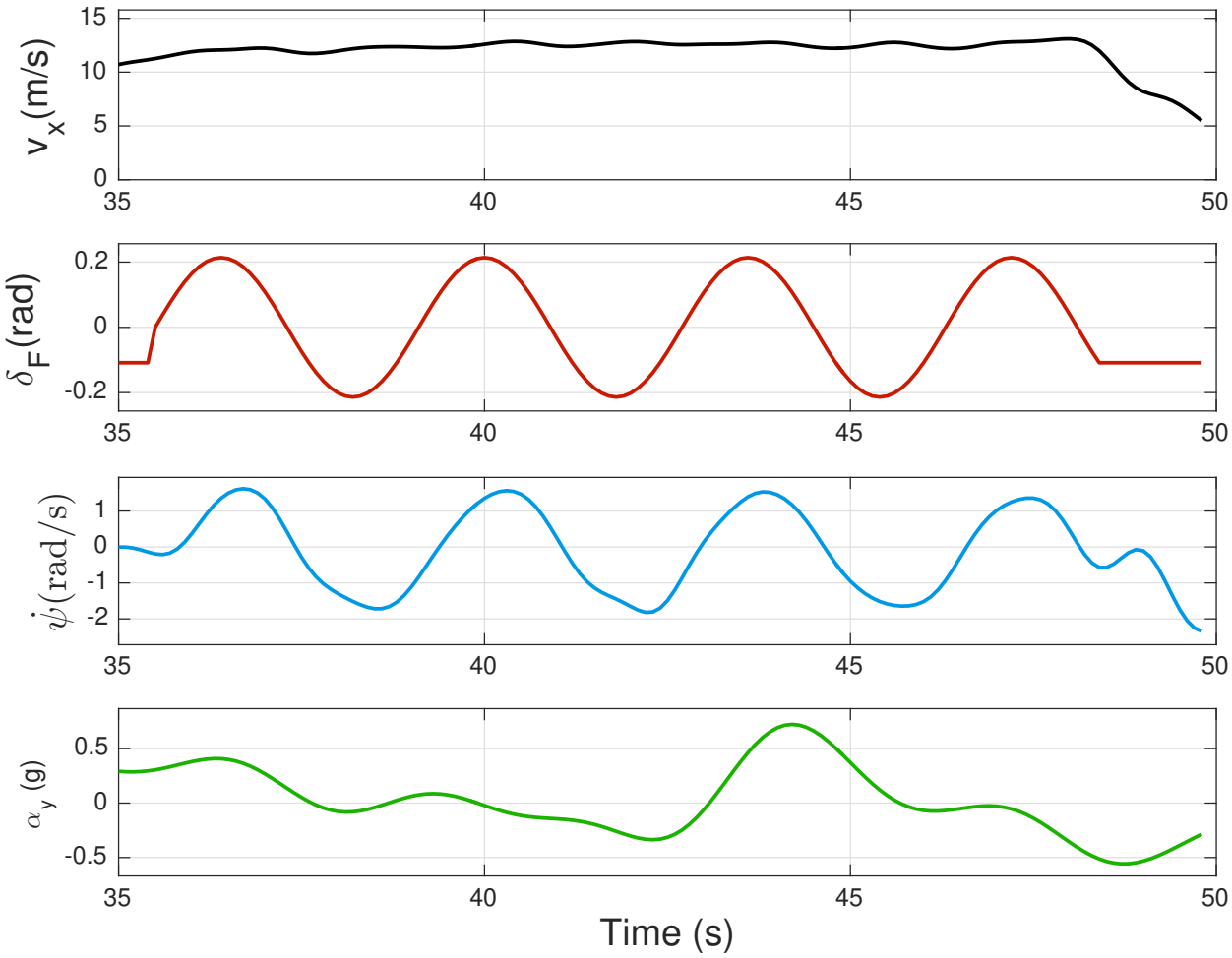

Figure 59: Sinusoidal steering maneuver

4.2 Experimentation with CCS enabled

4.2.1 Counterclockwise circular maneuver with CCS enabled

During this experiment, the prototype vehicle travels on a counterclockwise, circular maneuver with the Camber Control System (CCS) enabled. The longitudinal velocity of the vehicle is almost constant and equals $9m/s$ in the time interval from 10^{th} to 55^{th} second, as shown in first graph of Figure 60. Additionally, the front wheels steering angle δ_F is constant and almost equal to -0.2 rad in the same time period (second graph of Figure 60). As expected, the yaw rate $\dot{\psi}$ graph follows the curve shape of the steering angle δ_F. Thus, it almost equals to zero for the time interval from 0^{th} to 10^{th} second, is non zero (mean value $1.2rad/s$) between the 10^{th} and 55^{th} second, zero between 58^{th} and 60^{th} second. The lateral acceleration a_y curve is similar to the yaw rate, with an average value of 1g.

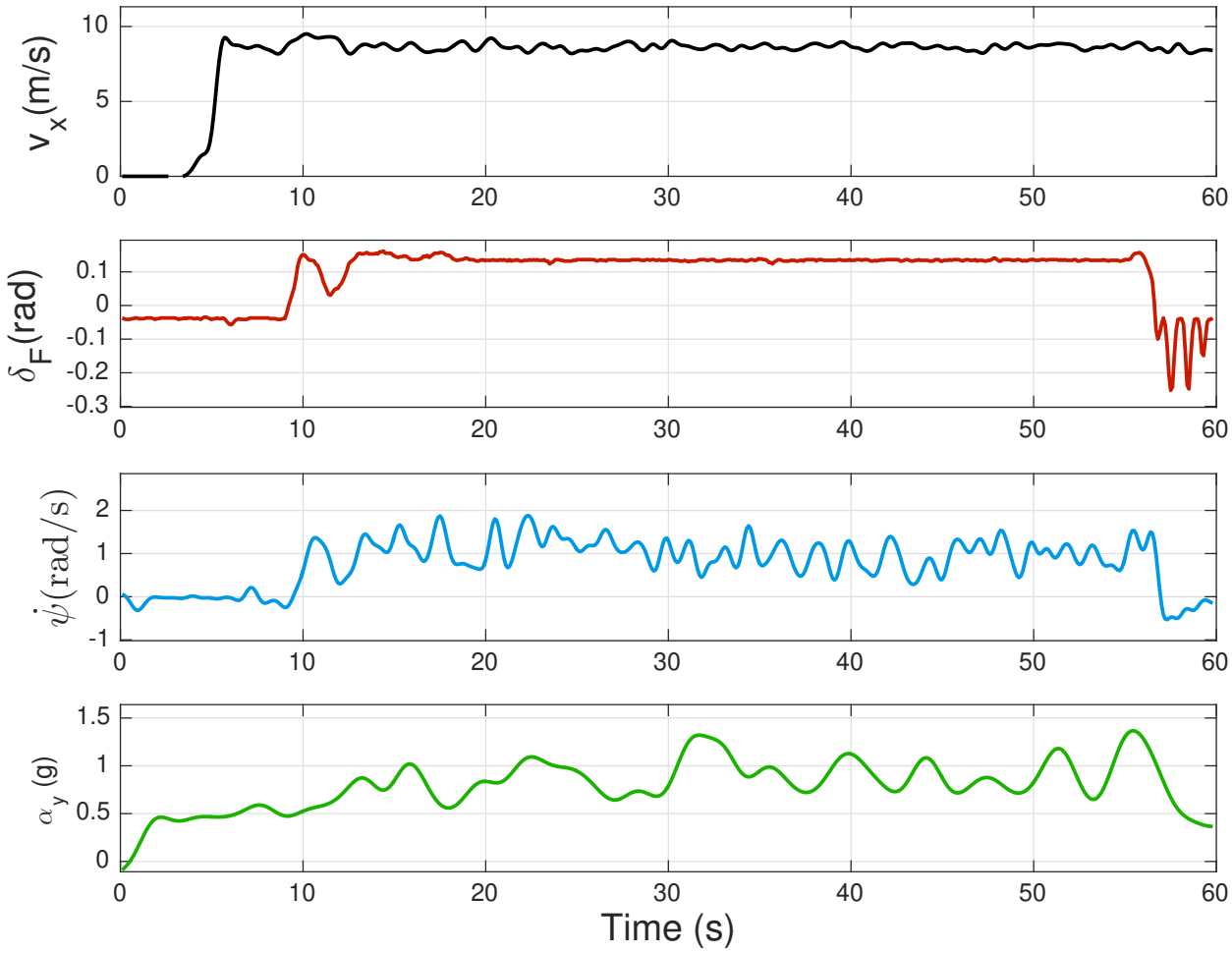

Figure 60: Left circular maneuver - Vehicle movement

In the first graph of Figure 61, the command signal to the CCS servo is depicted. The signal curve follows the yaw rate shape, which is reasonable according to the CCS algorithm design. The algorithm receives the yaw rate as imput, scales it to create a range from -0.26 ($\simeq -15degs$) to 0.26 rad ($\simeq 15degs$), and sends it as output to the CCS servo, only if the

yaw rate absolute value is greater than the predefined threshold of 0.9 rad/s.

The threshold existense explains the spikes appeared in the command signal curve. Since the yaw rate is noisy and the car movement cause yaw rate values right above the predefined threshold, the algorithm disables the ccs servo instantanously multiple times. However, those spikes did not practically affect that much the CCS servo behaviour. This is shown by the ccs_pos signal of the Figure 61, which represents the actual rotation of the CCS servo mechanism. It contains abrupt peaks, nevertheless the curve is smoother than the command signal curve.

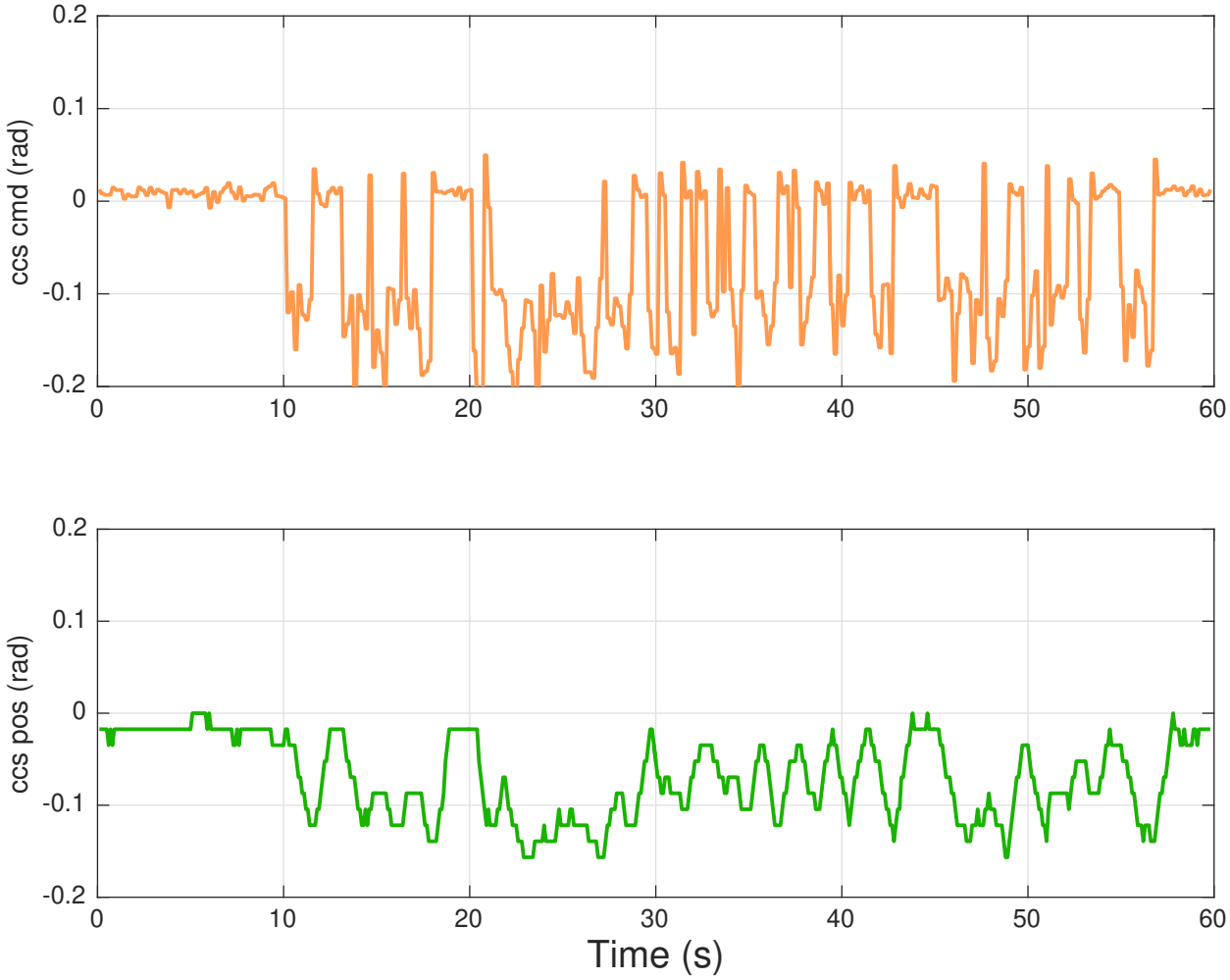

Figure 61: Left circular maneuver - Camber control signals

4.2.2 Clockwise circular maneuver with CCS enabled

During this experiment, the prototype vehicle travels on a clockwise, circular maneuver with the Camber Control System (CCS) enabled. The longitudinal velocity of the vehicle is almost constant and equals $10m/s$ in the time interval from 10^{th} to 55^{th} second, as shown in first graph of Figure 62. In addition, the front wheels steering angle δ_F is constant and almost equal to -0.2 rad in the same time period (second graph of Figure 62). The minus sign defines the clockwise steering. Just like in the previous experiment, the yaw rate $\dot{\psi}$ graph follows the curve shape of the steering angle δ_F. Thus, it almost equals to zero for the time interval from 0^{th} to 10^{th} second, is negative (mean value $-1.3rad/s$) between the 10^{th} and 60^{th} second, zero between 65^{th} and 70^{th} second. The lateral acceleration a_y curve is similar to the yaw rate, with an average value of 0.8g.

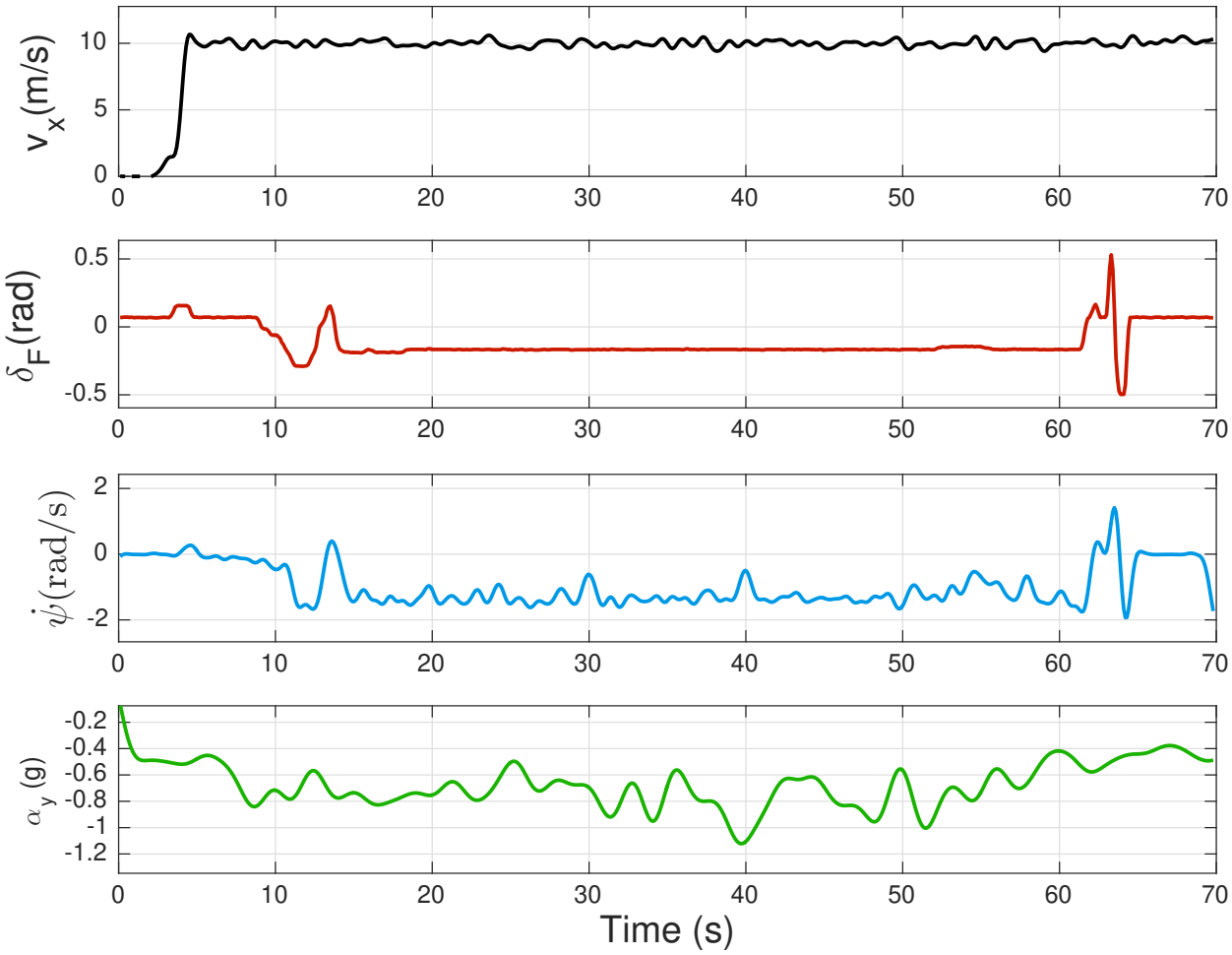

Figure 62: Clockwise circular maneuver - Vehicle dynamics

During this experiment, the yaw rate curve is less noisy, resulting in a more clear CCS servo command profile as shown in the first plot of Figure 63. Thus, even though there are a lot of spikes, the actual positioning of the CCS servo is not being affected negatively and the camber adjustment is smooth.

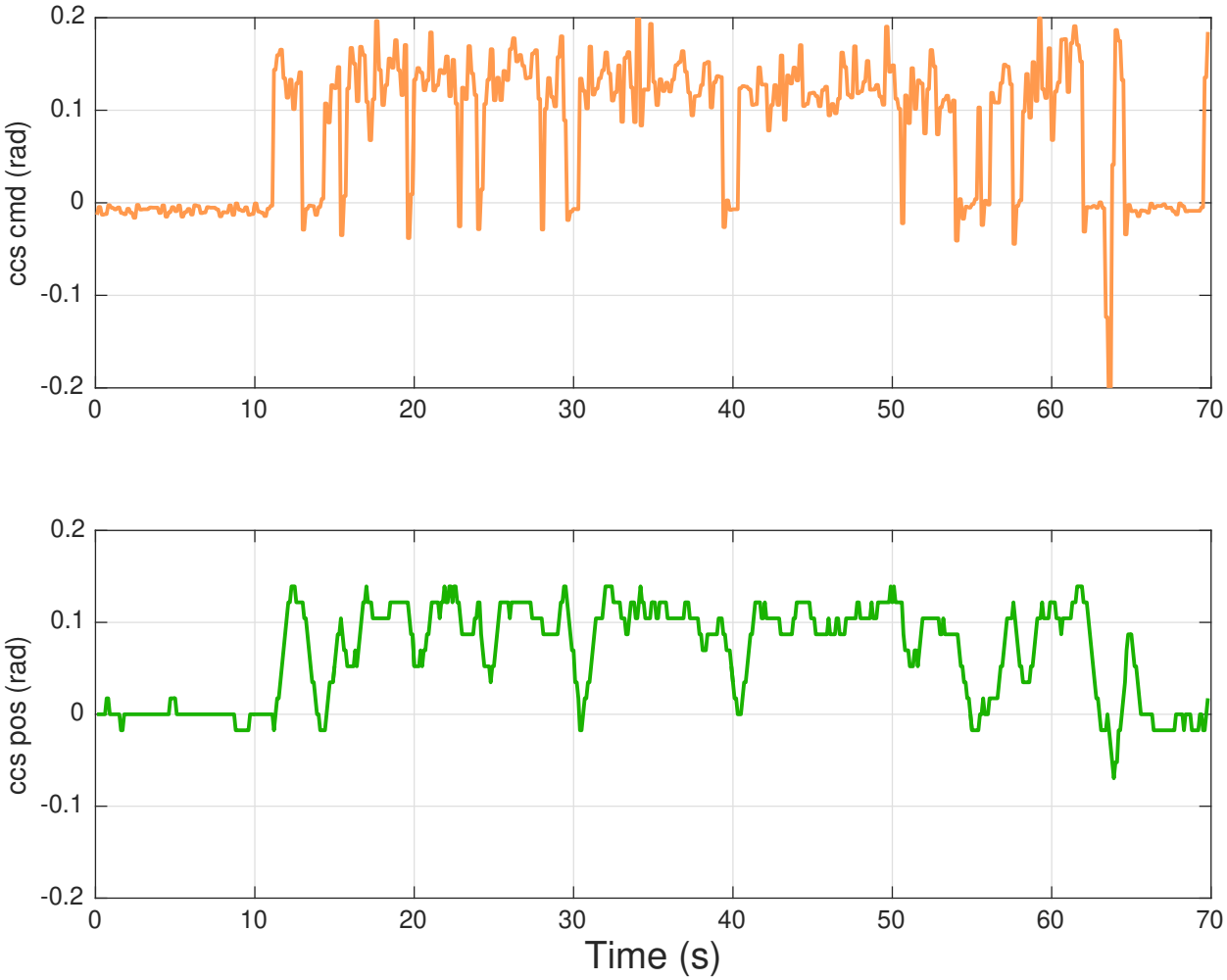

Figure 63: Clockwise circular maneuver - Camber control signals

4.2.3 Sinusoidal steering maneuver 1 with CCS enabled

In this experiment, the behaviour of the prototype vehicle across a sinusoidal steering maneuver with the CCS enabled is tested. As shown in Figure 64, the longitudinal velocity of the vehicle is almost constant and equals $8m/s$ in the in the entire time range presented. Moreover, the front wheels steering angle δ_F follows a sinusoidal steering profile with constant amplitude equals to 0.2 rad. The minus sign defines the clockwise steering. Just like in the previous experiments, the yaw rate $\dot{\psi}$ graph follows the curve shape of the steering angle δ_F, having a sinusoidal-like shape. The lateral acceleration a_y curve is similar to the yaw rate, with a maximum absolute value of 0.5g. As shown in Figure 65, the camber angle

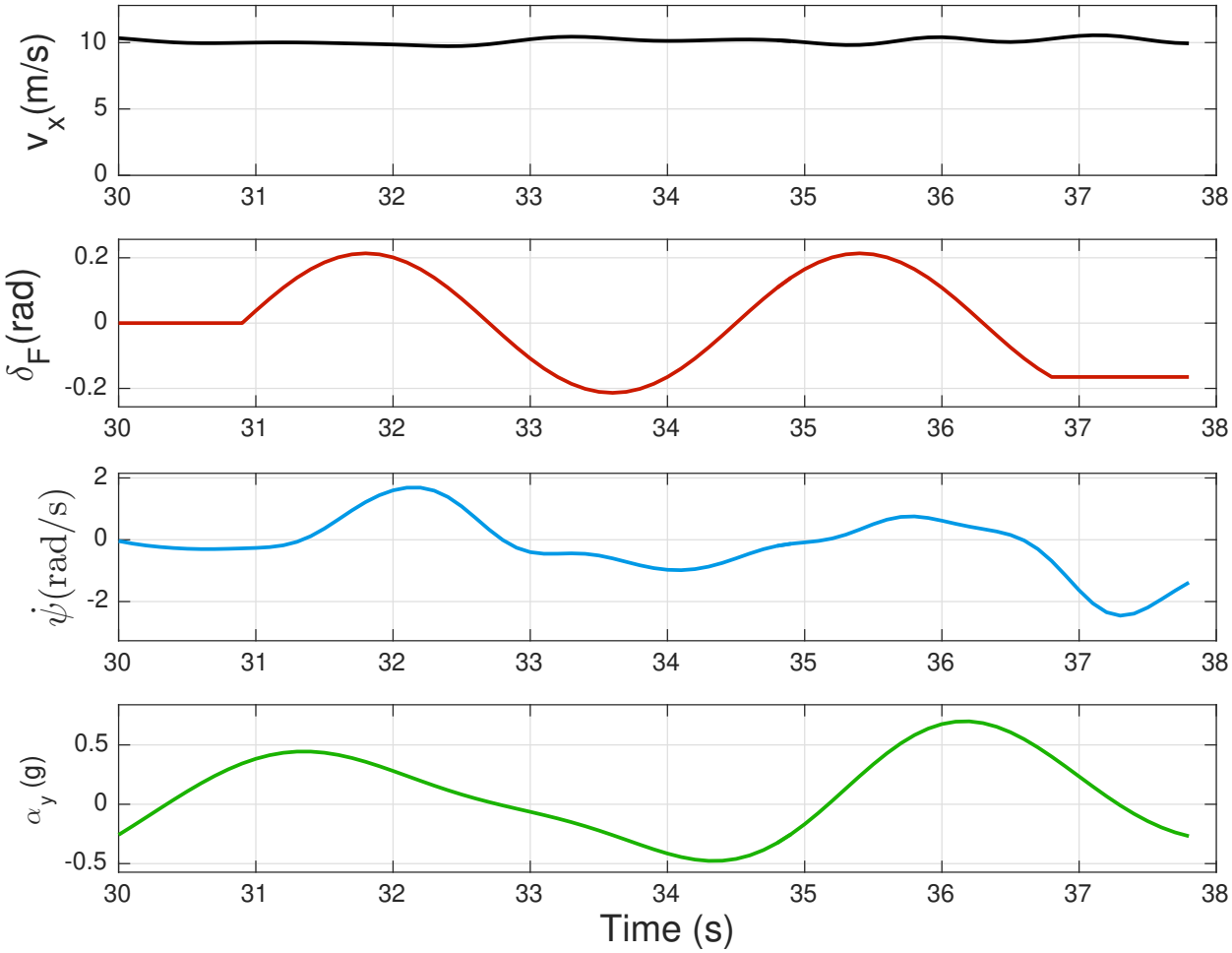

Figure 64: Sinusoidal maneuver (scaling factor 1.2) - Vehicle dynamics

was not adjusted a lot because of the low values of the yaw rate. Though, since the yaw rate curve is clear enough due to the sinusoidal steering angle, the CCS servo command and actual positioning does not contain any spikes.

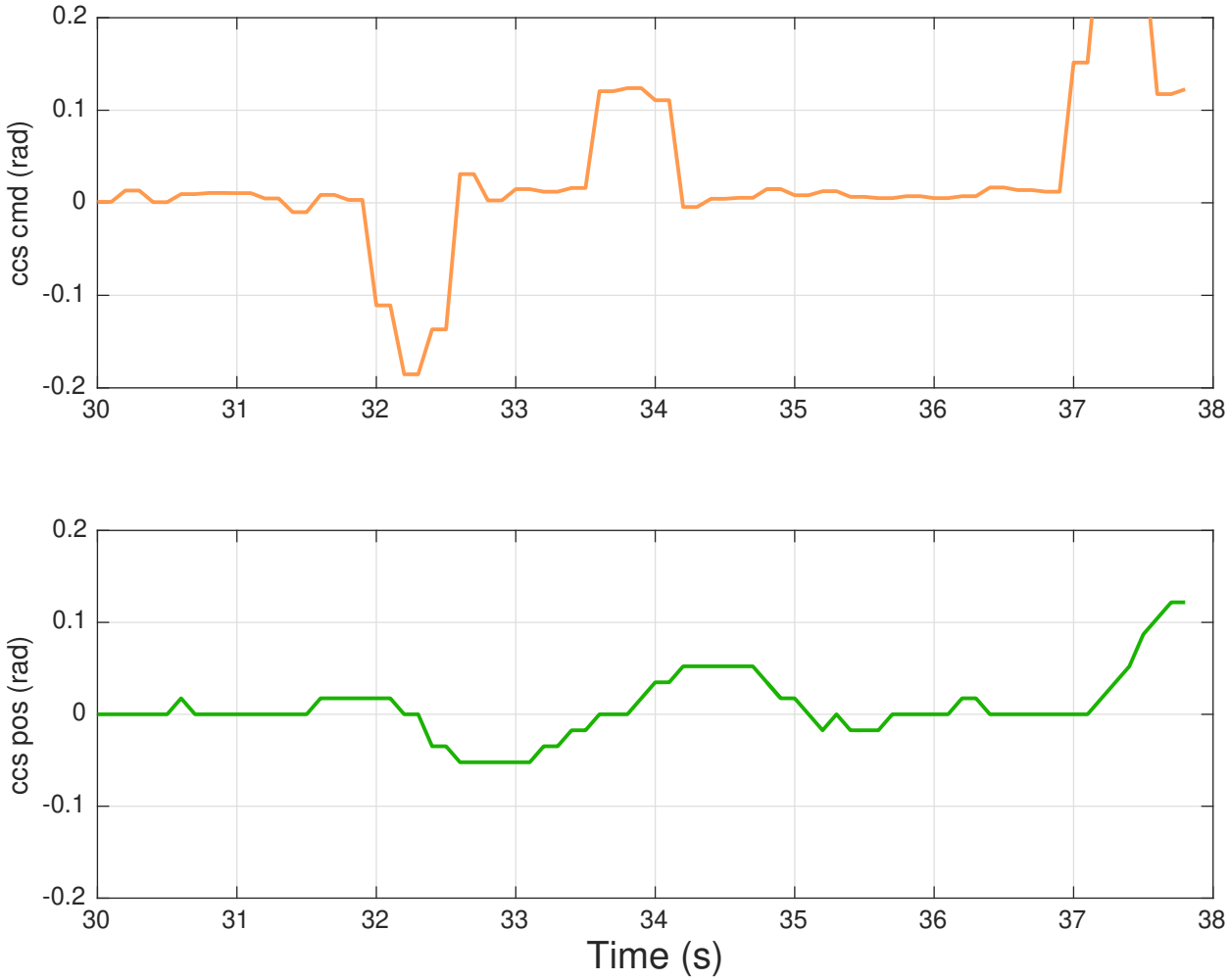

Figure 65: Sinusoidal maneuver (scaling factor 1.2) - Camber control signals

4.2.4 Sinusoidal steering maneuver 2 with CCS enabled

In this experiment, the behaviour of the prototype vehicle response with the CCS enabled is tested again on a sinusoidal steering input. As shown in Figure 66, the longitudinal velocity of the vehicle is almost constant and equals $8m/s$ in the in the entire time range presented. Moreover, the front wheels steering angle δ_F follows a sinusoidal steering profile with constant amplitude equals to 0.2 rad. In this case, not only the the yaw rate values are higher, but also the CCS algorithm was set with a higher scaling factor, resulting in a more effective camber angle control as shown in Figure 67.

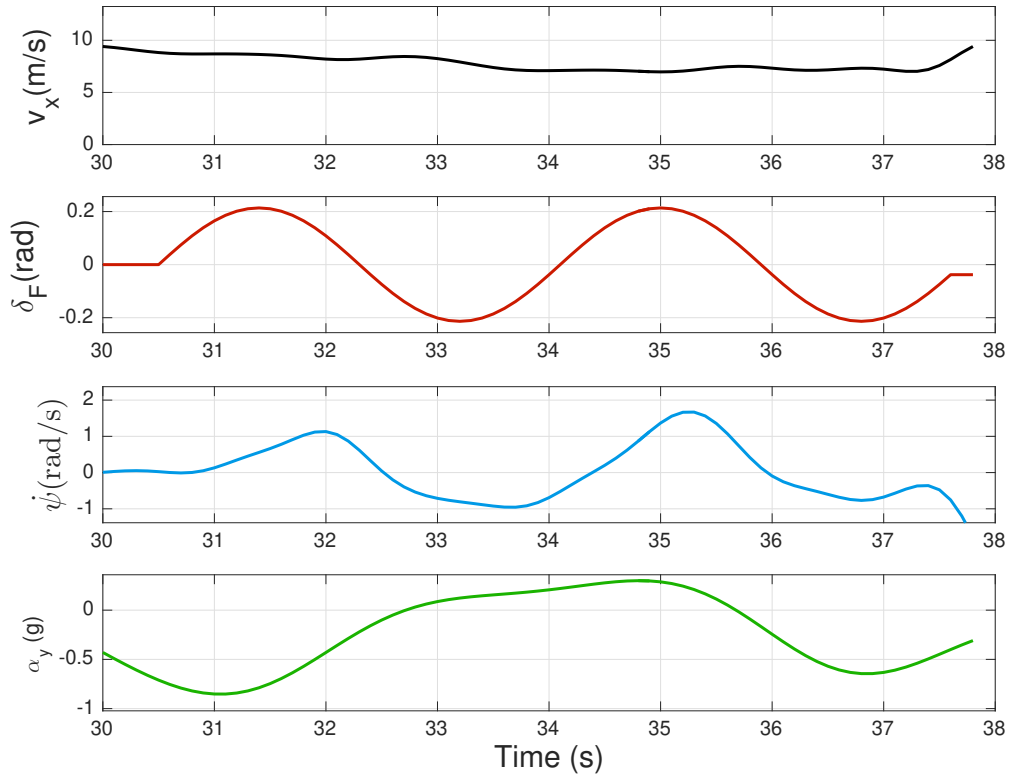

Figure 66: Sinusoidal maneuver (scaling factor 1.4) - Vehicle dynamics

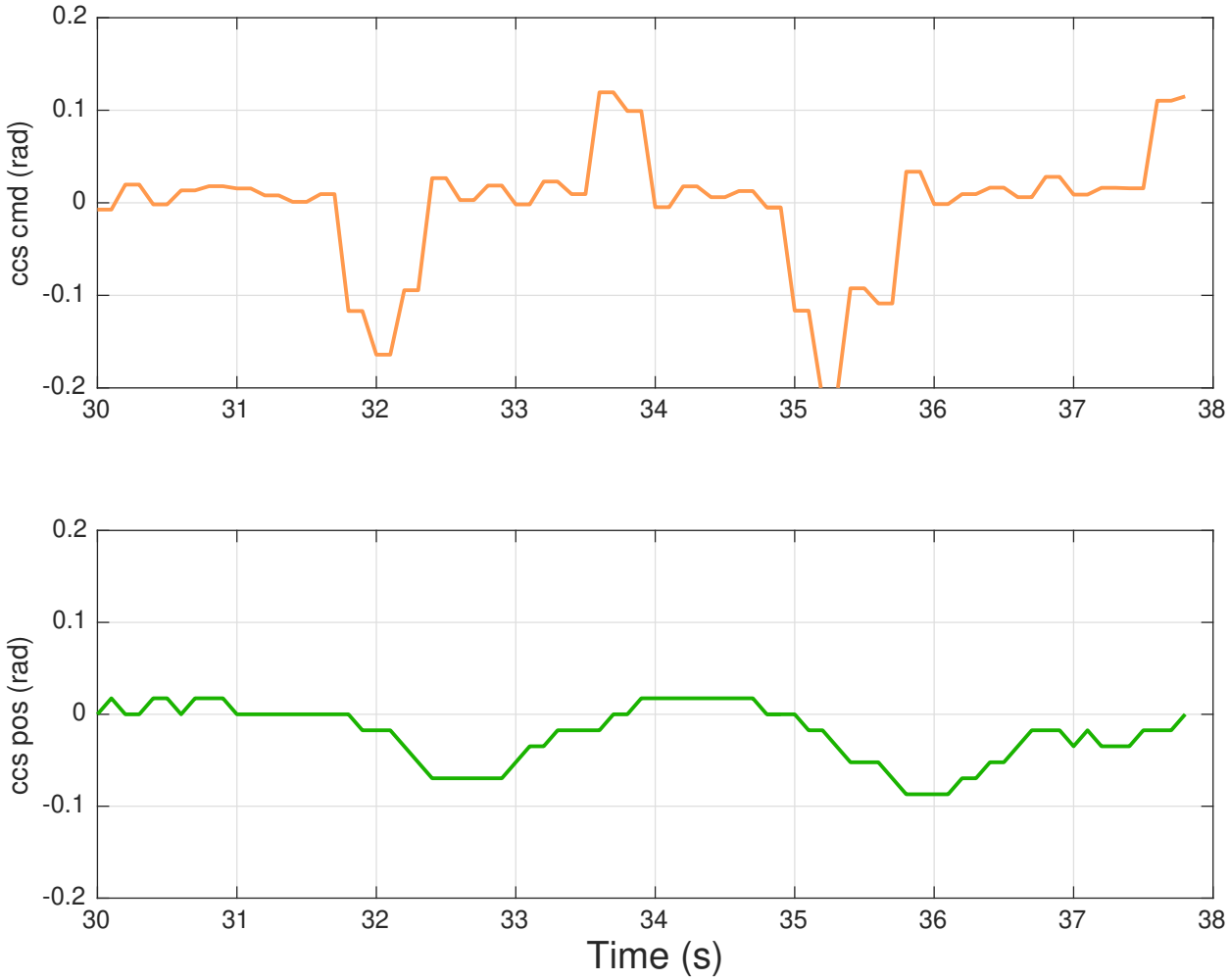

Figure 67: Sinusoidal maneuver (scaling factor 1.4) - Camber control signals

4.3 Comparison

The plots in Figures 68 and 69 present a comparison between the vehicle behaviour with the CCS disabled and the vehicle behaviour with the CCS enabled.

Figure 68 represents a counterclockwise circular maneuver for both cases (CCS enabled and CCS disabled). As shown, the longitudinal velocity of the vehicle is stabilized in the time interval between the 12^th and 58^th second. It is almost equal to $12m/s$ when the CCS is disabled and around $9m/s$ when the CCS is enabled. At the same time period, the steering angle of the wheels is constant and almost equal to 0.15rad for both cases. The yaw rate curve is similar for both experiments. The fourth graph represents the lateral acceleration and as it is observed the blue line (representing the enabled CCS) is slightly above the orange line (representing the disabled CCS). That means, higher lateral acceleration occured with the CCS enabled, even though the longitudinal velocity is lower than the case in which the CCS is disabled. Thus, the vehicle could potentially travel through a corner in a higher speed having the CCS enabled.

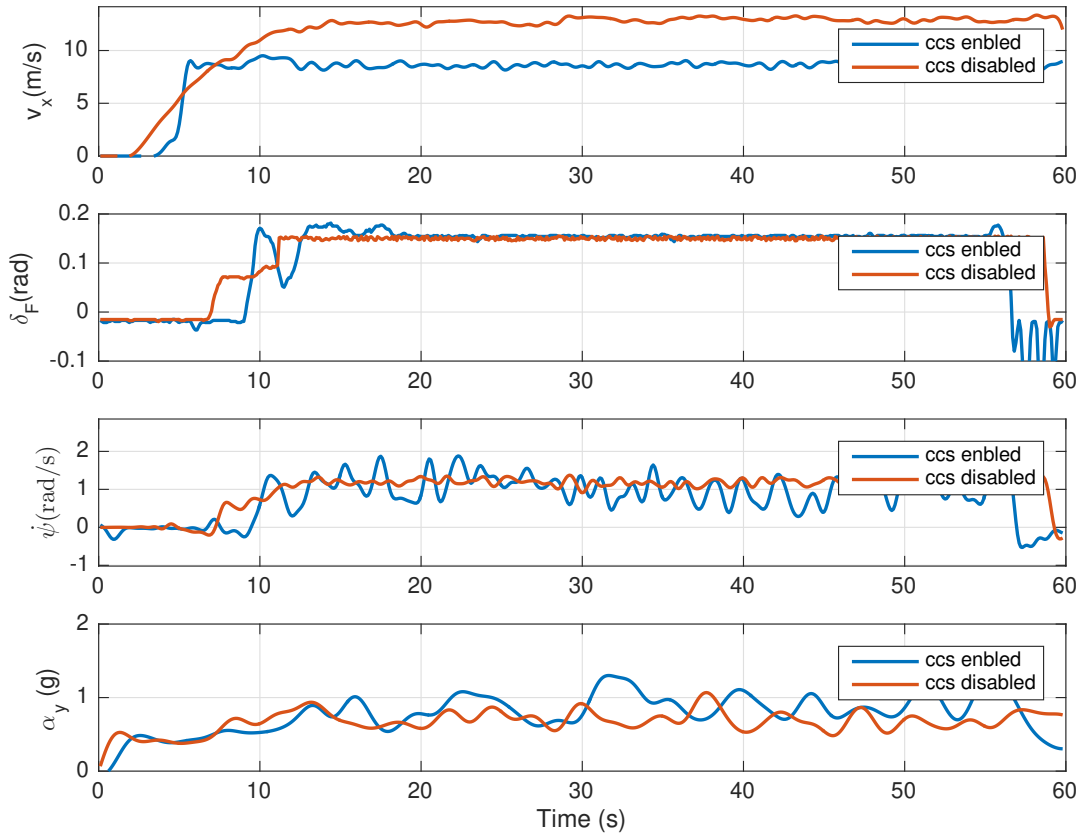

Figure 68: Left circular maneuver - Comparison CCS enbled - CCS disabled

Figure 68 represents a clockwise circular maneuver for both cases (CCS enabled and CCS disabled). As shown, the longitudinal velocity of the vehicle is stabilized in the time interval between the 20^th and 78^th second. It is almost equal to $14m/s$ when the CCS is disabled and around $10m/s$ when the CCS is enabled. At the same time period, the steering angle of the wheels is constant and almost equal to 0.12rad for both cases. The yaw rate curve is similar for both experiments. The fourth graph represents the lateral acceleration and as it is observed the blue line (representing the enabled CCS) is slightly below the orange line (representing the disabled CCS). That means higher lateral acceleration occured with the CCS enabled, even though the longitudinal velocity is lower than the case in which the CCS is disabled. Thus, the vehicle could potentially travel through a corner in a higher speed having the CCS enabled.

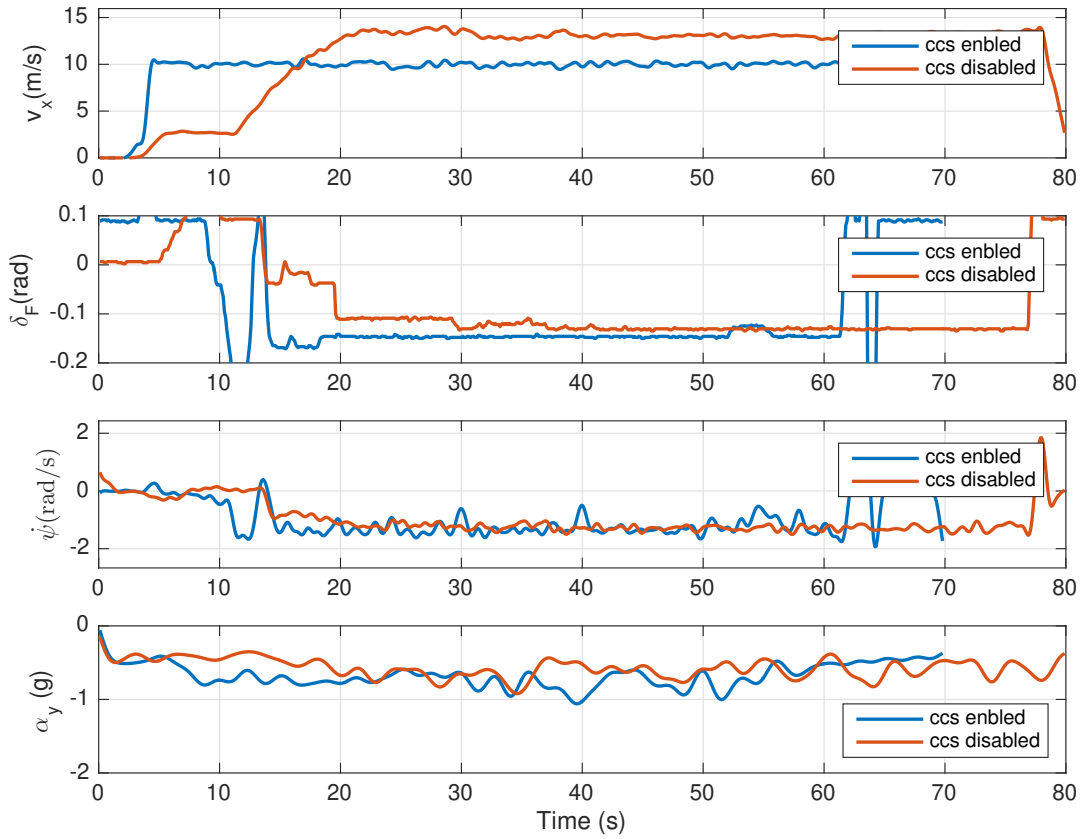

Figure 69: Right circular maneuver - Comparison CCS enbled - CCS disabled

5 Conclusion

Comparing the results from the circular maneuvers tests (Figures 68, 69), it is clear that the effects on the camber angle adjustment could be considered as benefit for the lateral behaviour of the vehicle. During both the clockwise and counterclockwise circular maneuvers, the lateral acceleration (α_y) is higher when the CCS is enabled, even though the vehicle travels with slightly lower longitudinal velocity. That means that the total grip of the vehicle was improved and the vehicle can travel through corners in higher speed without slipping.

The sinusoidal maneuver experimental results show that the proposed system does not provide any major improvement to the vehicle lateral acceleration. It was an expected outcome because this type of test was performed for the validation of the system from the perspective of the mechanism working quality. Thus, the sinusoidal signal was programmed to run in a high frequency and the vehicle had no time to acquire high lateral acceleration. In other words, the sinusoidal test was designed for a more optical validation of the control system behaviour.

Generally, the CCS improved the prototype vehicle behaviour more than expected. Additionally, it is proved that the yaw rate signal is an appropriate reference for the camber angle control algorithm. Potentially, such a system could be used not only for commercial and racing cars, but also for self driving cars improving their autonomous behaviour.

For future work, the implementation of a more sophisticated algorithm could be suggested. The use of H-infinity or MPC (Model Predictive Control) approach could offer more reliable results, suitable for more complicated maneuvers. Moreover, the CCS mechanism could be improved by developing a suitable pneumatic or hydraulic system. Finally, the proposed system could be more effective in combination with another active control system, like all wheel steering, active suspension etc.

References

[1] Mohammad Iman Mokhlespour Esfahani. "Optimization of Double Wishbone Suspension System with Variable Camber Angle by Hydraulic Mechanism". In: *International Journal of Mechanical and Mechatronics Engineering* 4.1 (2010).

[2] Thomas D. Gillespie. *Fundamentals of Vehicle Dynamics*. SAE International, 1992. ISBN: 978-1-56091-199-9.

[3] J. Happian-Smith. *An Introduction to Modern Vehicle Design*. Butterworth-Heinemann, 2001. ISBN: 9780750650441. URL: https://books.google.gr/books?id=36kg2DJiy7cC.

[4] SAE International. "Vehicle Dynamics Terminology". In: *SAE International* (2008). DOI: J670JAN2008.

[5] C. Kavitha et al. "Active camber and toe control strategy for the double wishbone suspension system". In: *Journal of King Saud University - Engineering Sciences* 31.4 (2019), pp. 375–384. ISSN: 1018-3639. DOI: https://doi.org/10.1016/j.jksues.2018.01.003. URL: http://www.sciencedirect.com/science/article/pii/S1018363917302799.

[6] MathWorks. *Matlab*. URL: https://www.mathworks.com/.

[7] Hans B. Pacejka. "Tire and Vehicle Dynamics (Third Edition)". In: ed. by Hans B. Pacejka. Third Edition. Oxford: Butterworth-Heinemann, 2012. ISBN: 978-0-08-097016-5. DOI: https://doi.org/10.1016/B978-0-08-097016-5.00001-2. URL: http://www.sciencedirect.com/science/article/pii/B9780080970165000012.

[8] Porsche. *Rear-axle steering*. URL: https://www.porsche.com/international/models/911/911-gt3-models/911-gt3/drive-chassis/rear-axle-steering/.

[9] Rajamani R. *Vehicle dynamics and control*. Springer, 2006. ISBN: 978-0-387-26396-0.

[10] William B. Ribbens. *Understanding Automotive Electronics*. Butterworth–Heinemann. ISBN: 0-7506-7008-8.

[11] Wolfgang Weiss. "Wheel Suspension with Automatic Camber Adjustment". US6,267,387B1. 2001.

[12] Anders Wikstrom. *Yaw Rate and Lateral Acceleration Sensor Plausibilisation in an Active Front Steering Vehicle*. 2006.

[13] Carlos Eduardo Guex Falcão Wilcker Neuwald Schinestzki Daniel Gustavo Schreiner. "Design of an automatic Drag Reduction System focusing on cooling for Formula SAE vehicle". In: *SAE International* (2016). DOI: 2016-36-0511.

[14] Douglas L Milliken William F Milliken. *Race car vehicle dynamics*. Warrendale, Pa. Society of Automotive Engineers, 1995. ISBN: 1560915269 9781560915263.

[15] Takahiko Yoshino and Hiromichi Nozaki. "About the Effect of Camber Control on Vehicle Dynamics". In: *SAE International* (2014). DOI: 10.4271/2014-01-2383.

6 Appendix

6.1 Simulation results

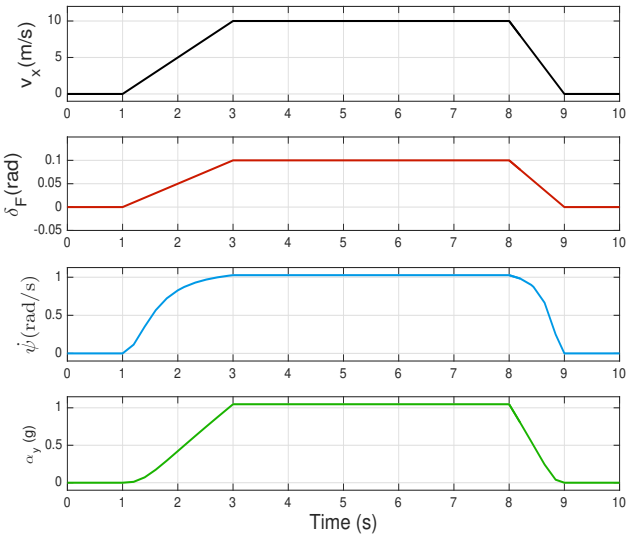

(a) Counterclockwise circular maneuver

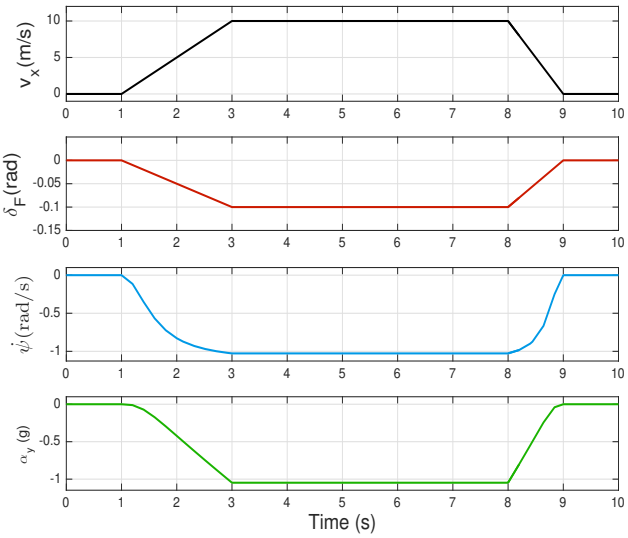

(b) clockwise circular maneuver

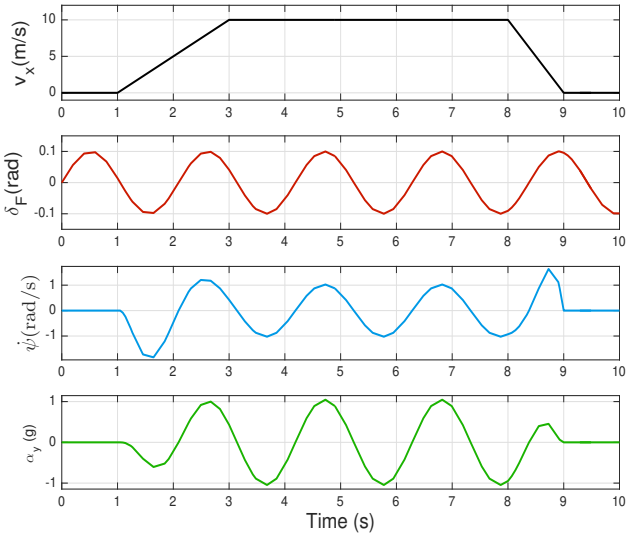

(c) Sinusoidal steering maneuver

Figure 70: CCS control signals - Scaling factor 0.0

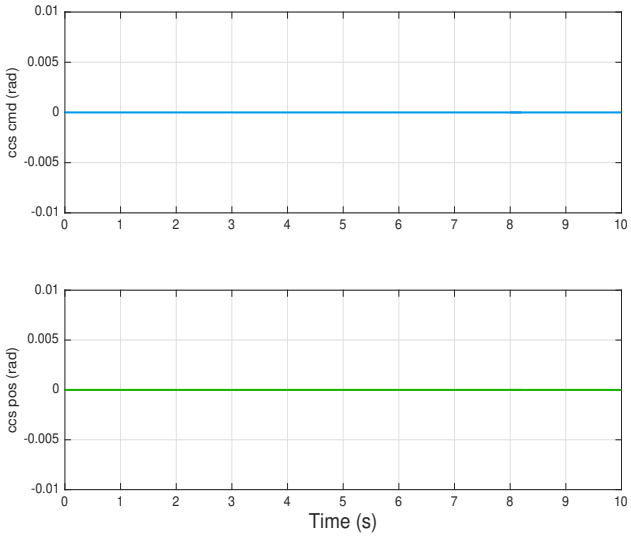

(a) Counterclockwise circular maneuver

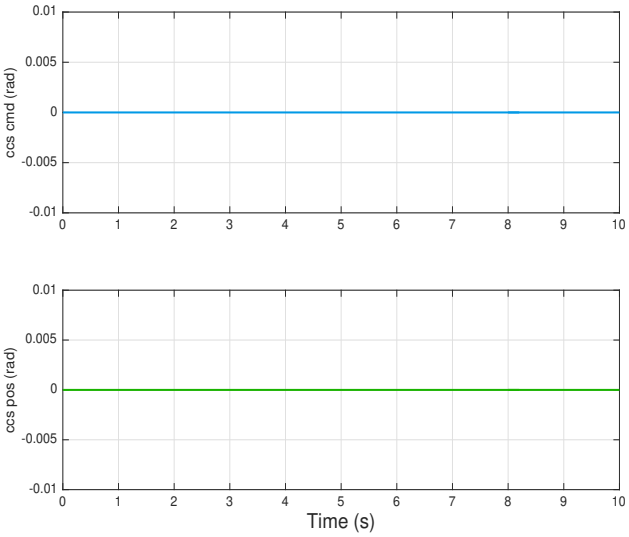

(b) clockwise circular maneuver

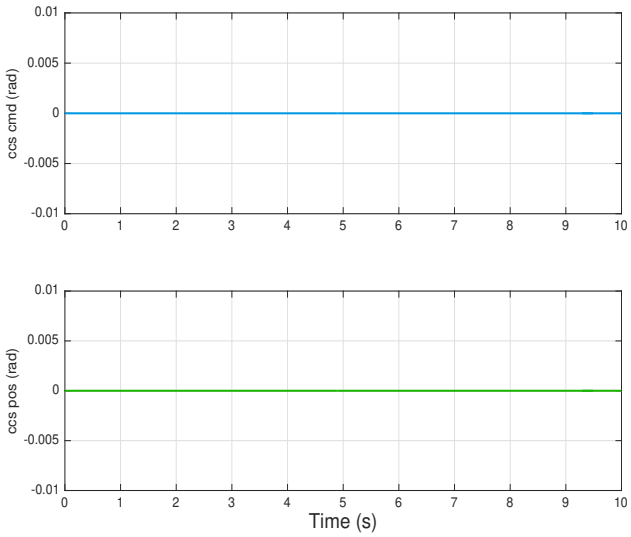

(c) Sinusoidal steering maneuver

Figure 71: CCS control signals - Scaling factor 0.0

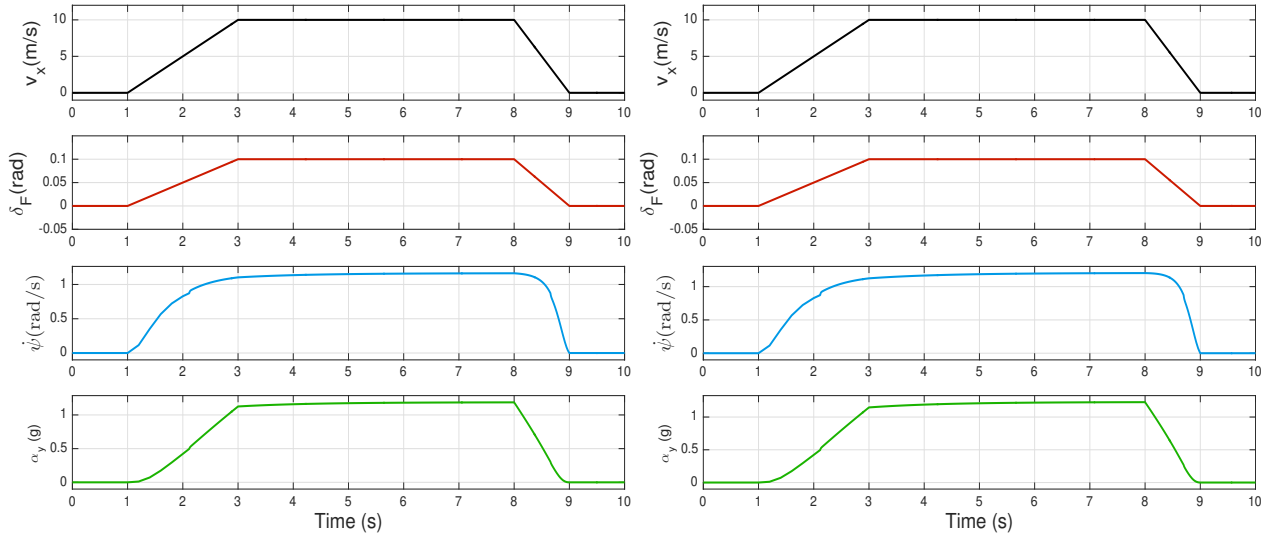

(a) Scaling Factor 0.08

(b) Scaling factor 0.1

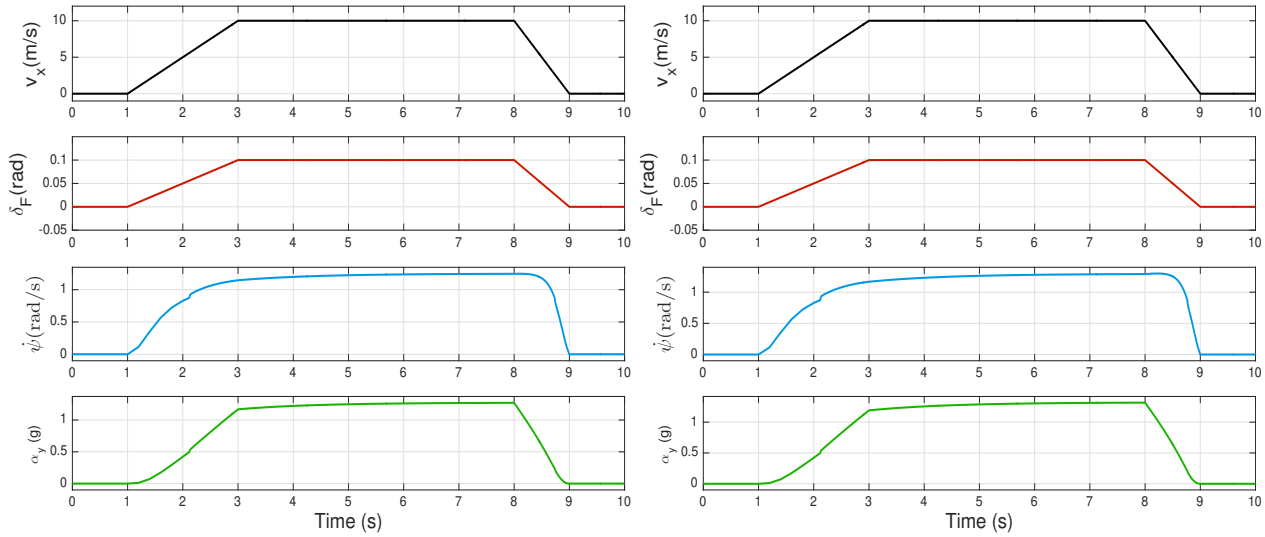

(c) Scaling factor 0.12

(d) Scaling factor 0.14

Figure 72: Counterclockwise circular maneuver simulation - Vehicle movement

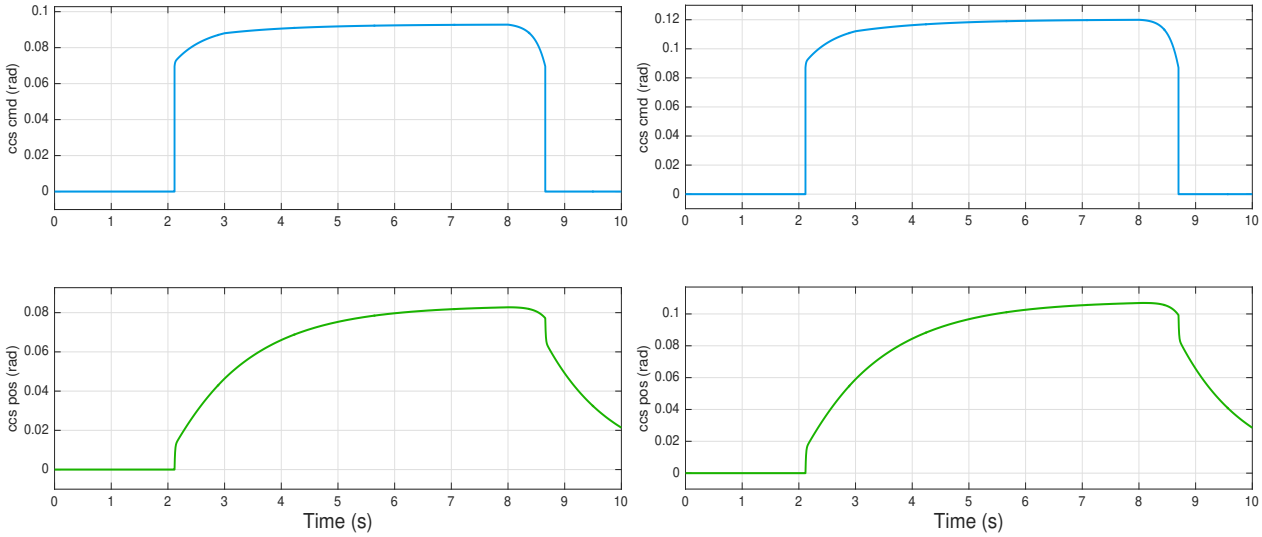

(a) Scaling Factor 0.08

(b) Scaling factor 0.1

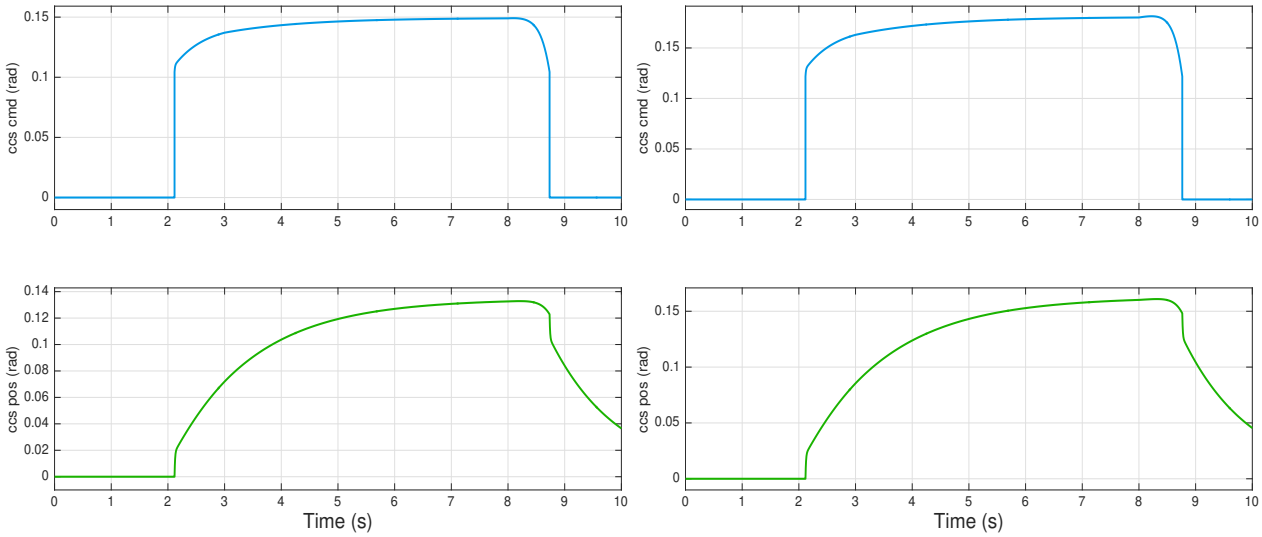

(c) Scaling factor 0.12

(d) Scaling factor 0.14

Figure 73: Counterclockwise circular maneuver simulation - CCS control signals

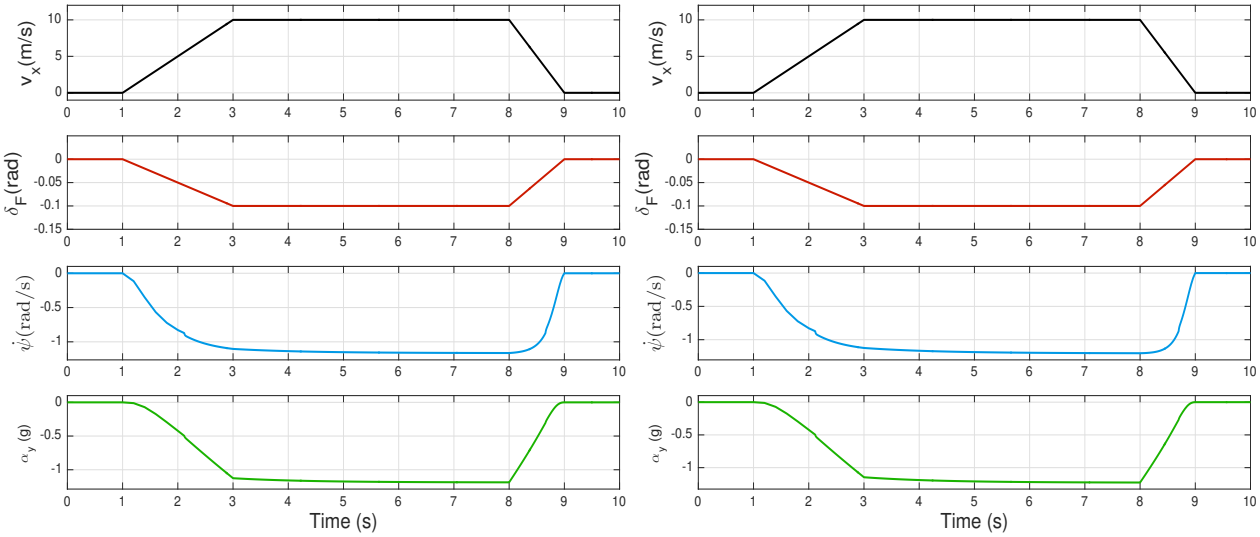

(a) Scaling Factor 0.08

(b) Scaling factor 0.1

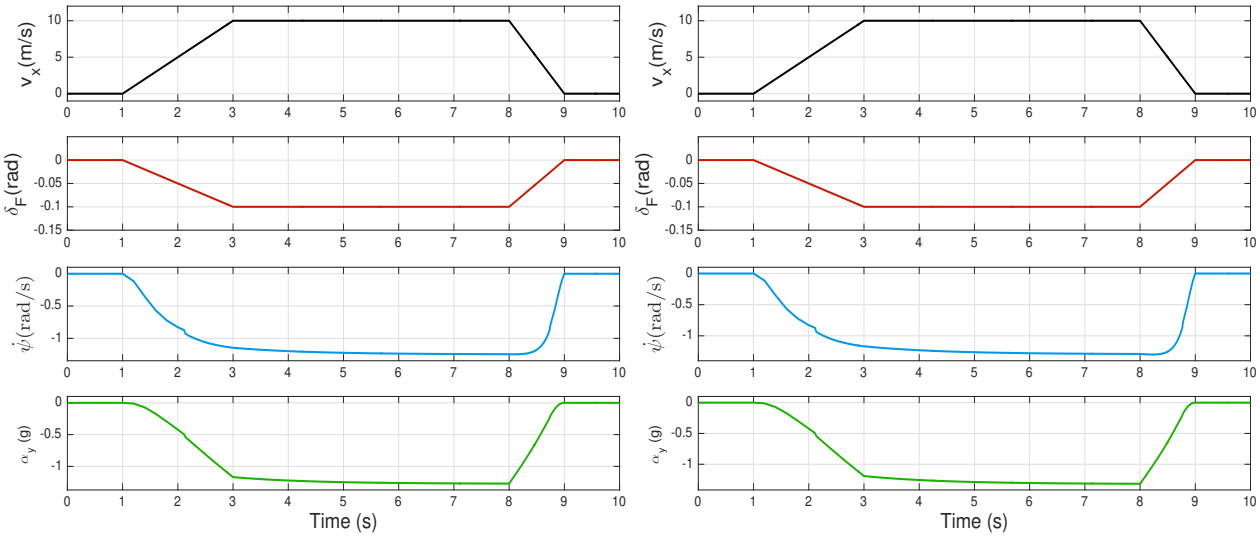

(c) Scaling factor 0.12

(d) Scaling factor 0.14

Figure 74: Clockwise circular maneuver simulation - Vehicle movement

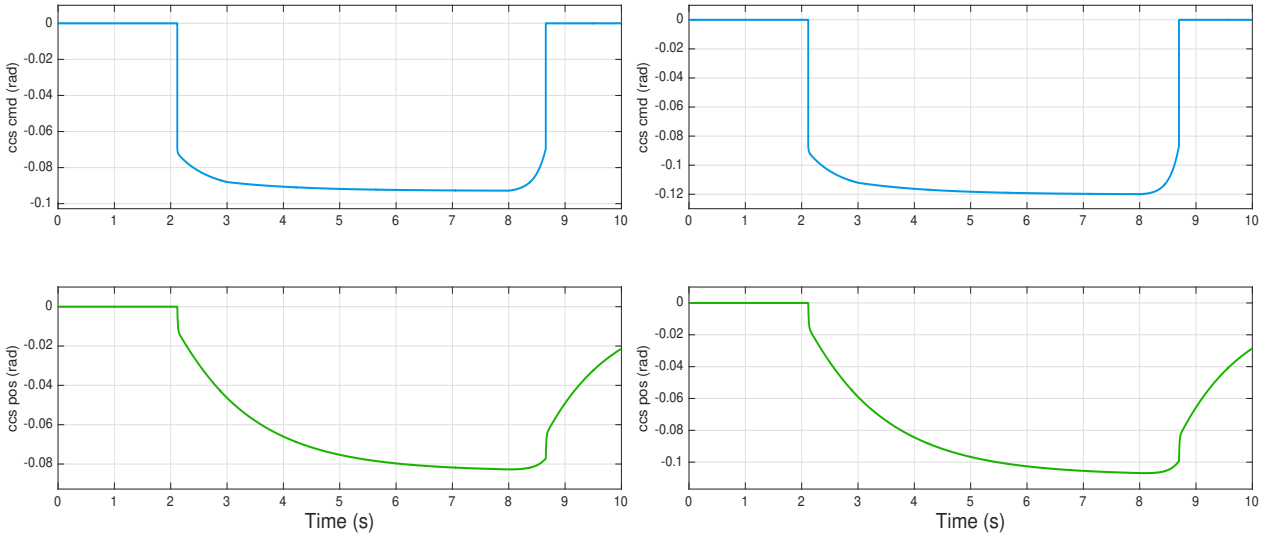

(a) Scaling Factor 0.08

(b) Scaling factor 0.1

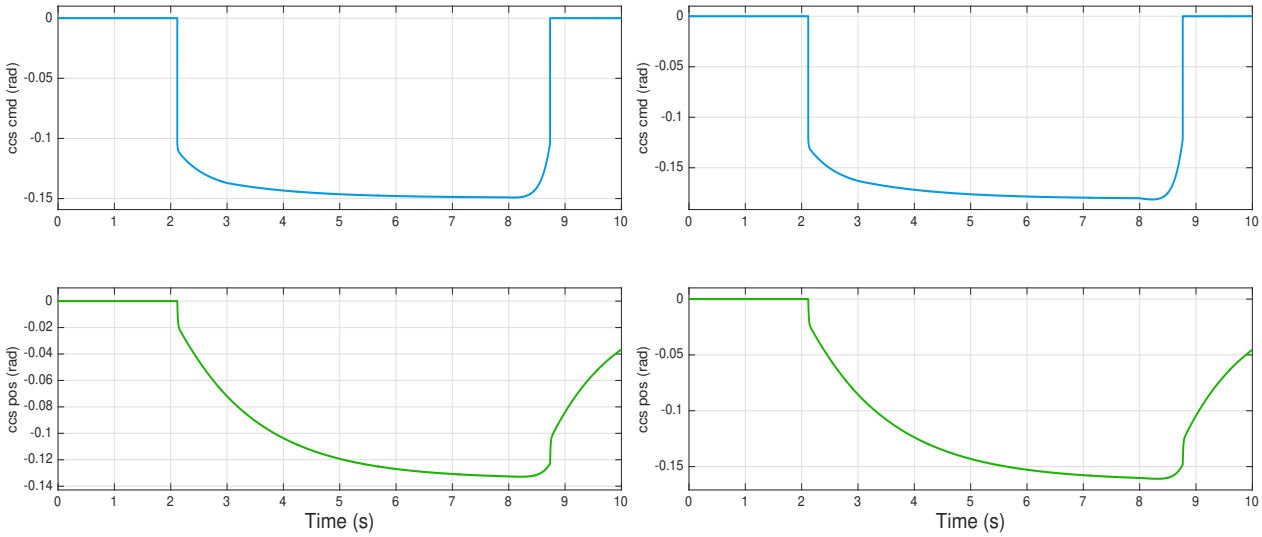

(c) Scaling factor 0.12

(d) Scaling factor 0.14

Figure 75: Clockwise circular maneuver simulation - CCS control signals

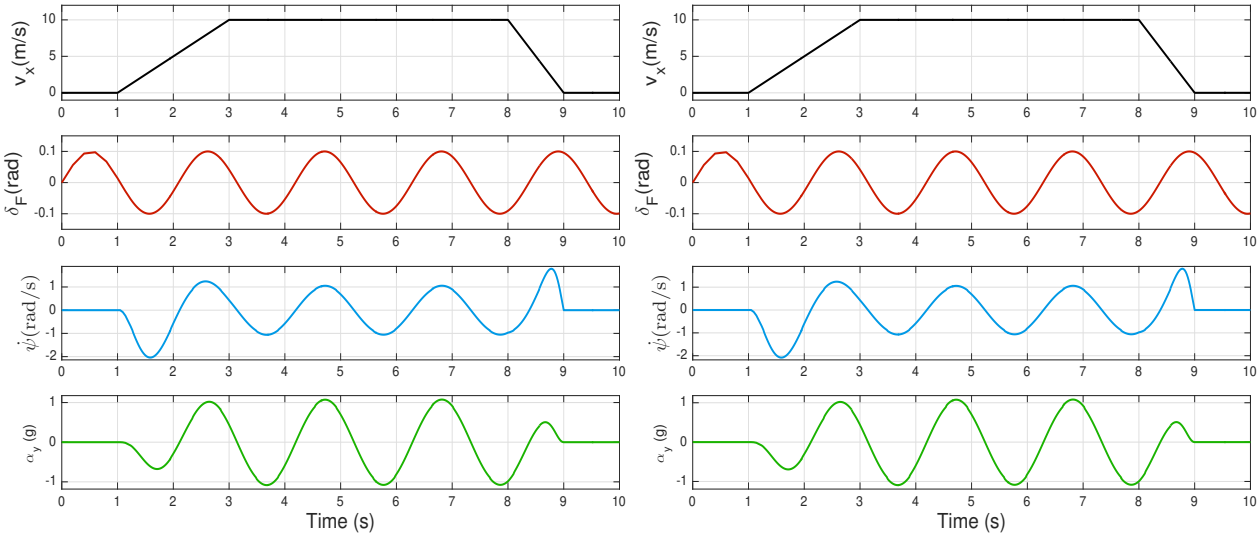

(a) Scaling Factor 0.08

(b) Scaling factor 0.1

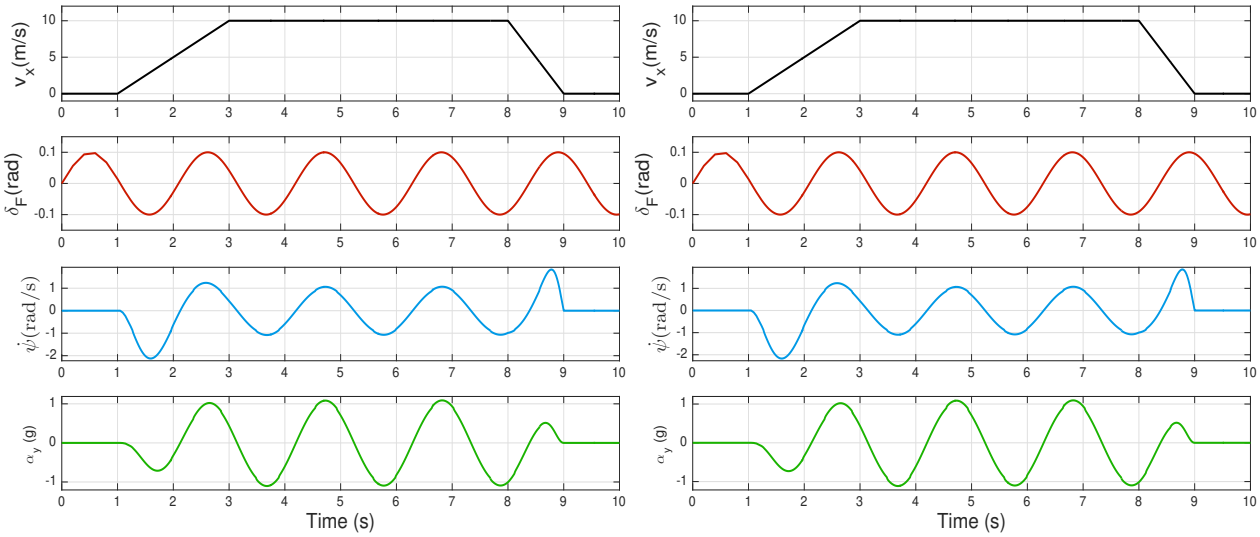

(c) Scaling factor 0.12

(d) Scaling factor 0.14

Figure 76: Sinusoidal steering maneuver simulation - Vehicle movement

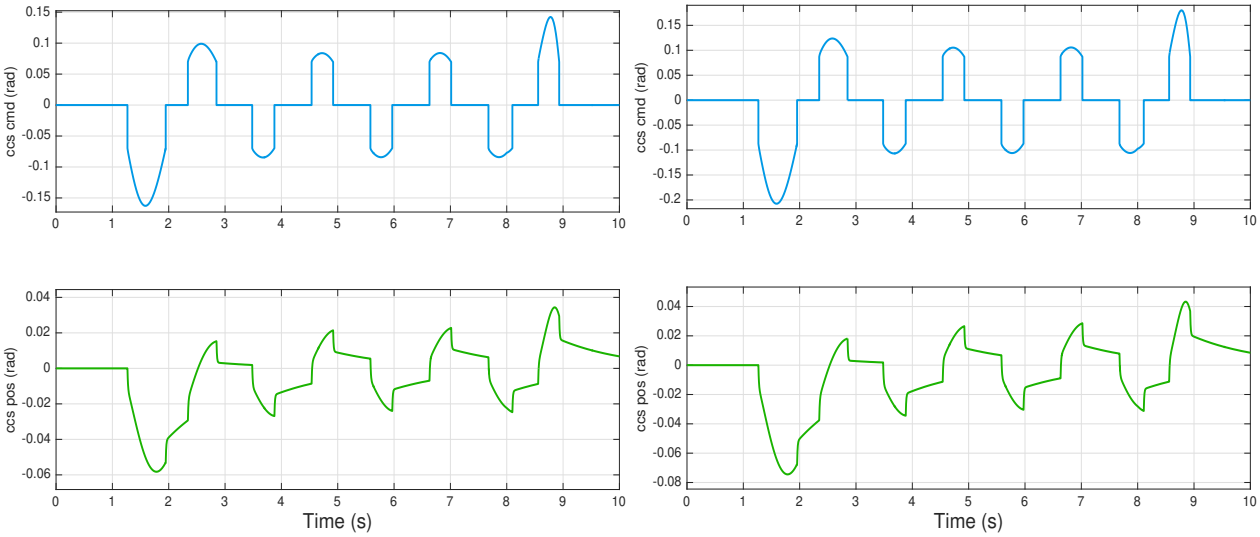

(a) Scaling Factor 0.08

(b) Scaling factor 0.1

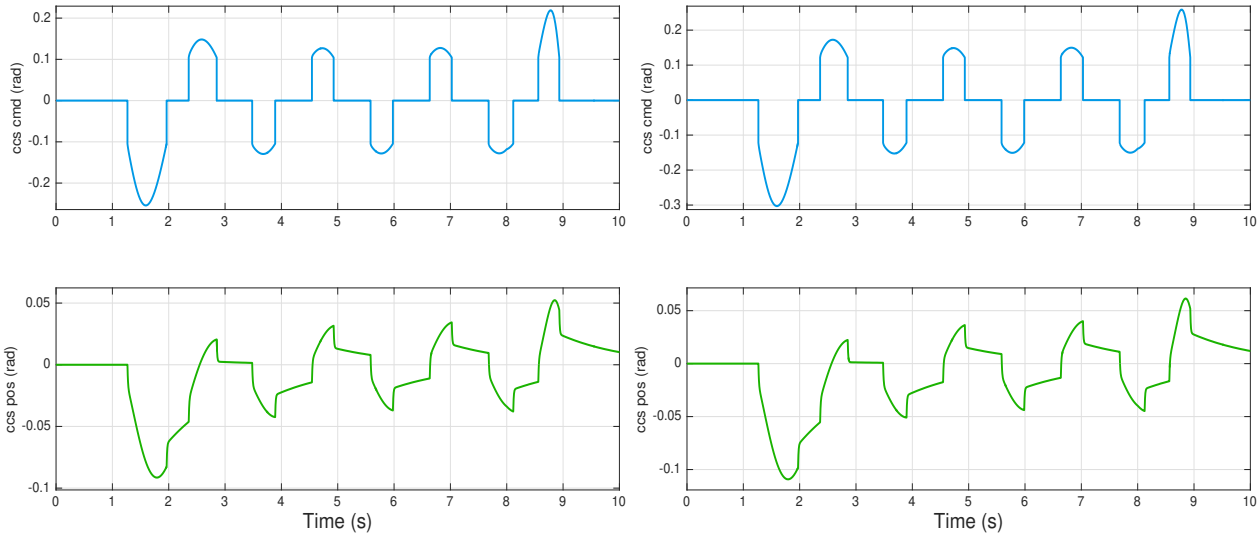

(c) Scaling factor 0.12

(d) Scaling factor 0.14

Figure 77: Clockwise circular maneuver simulation - CCS control signals

6.2 Prototype vehicle assembly

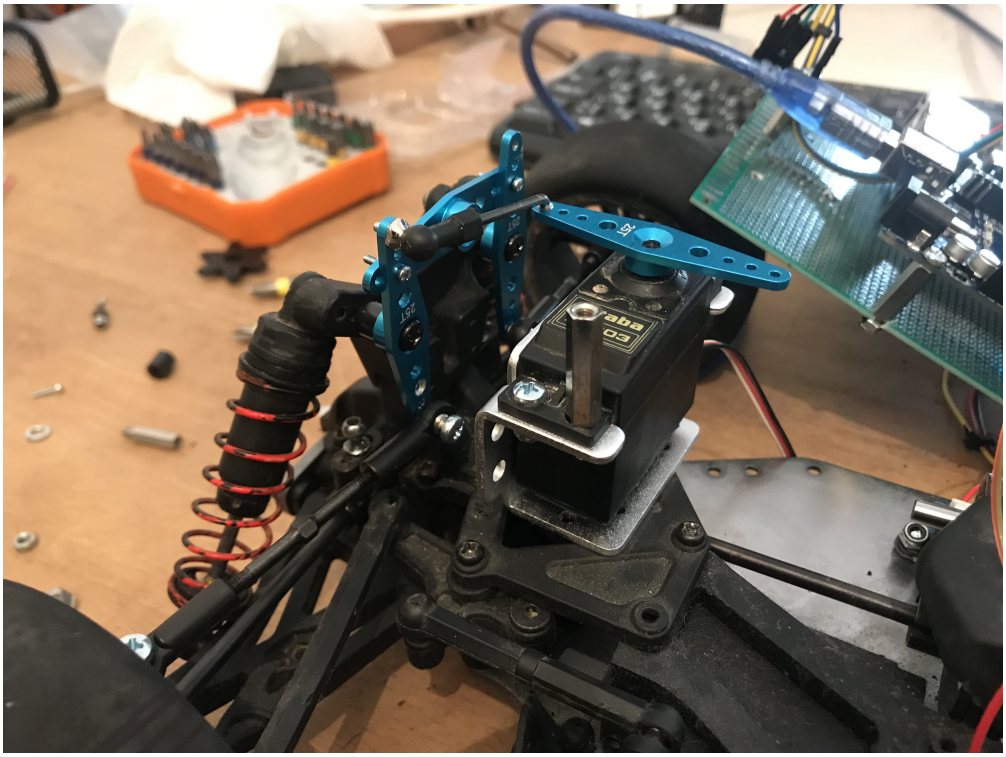

Figure 78: Side view of the CCS mechanism

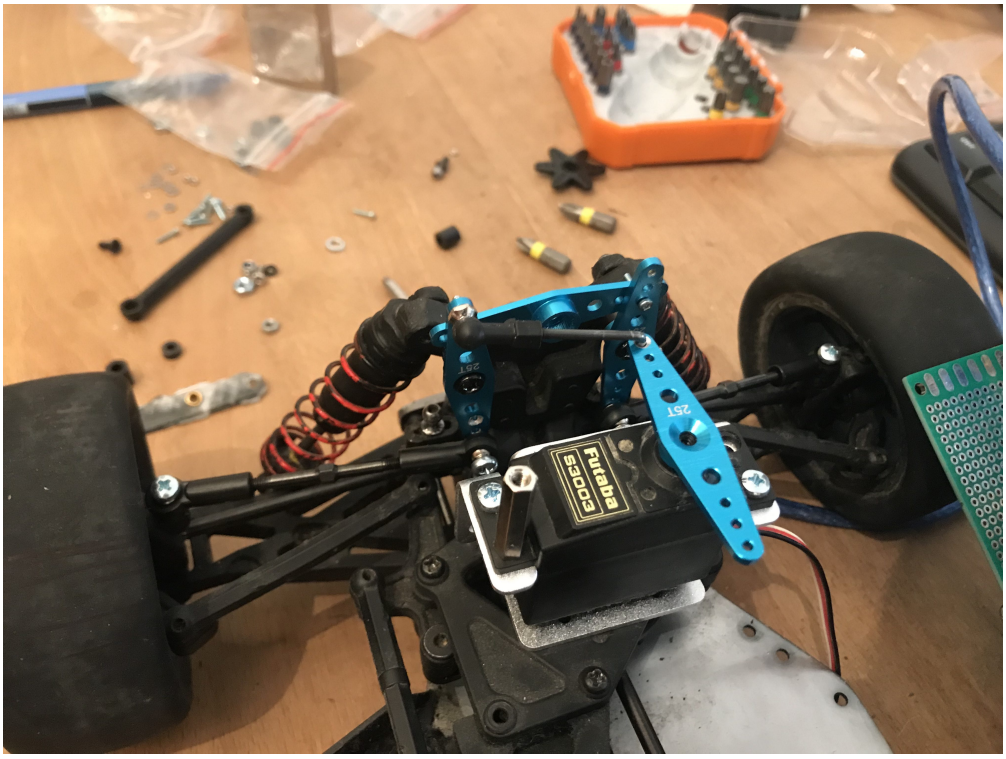

Figure 79: Rear view of the CCS mechanism

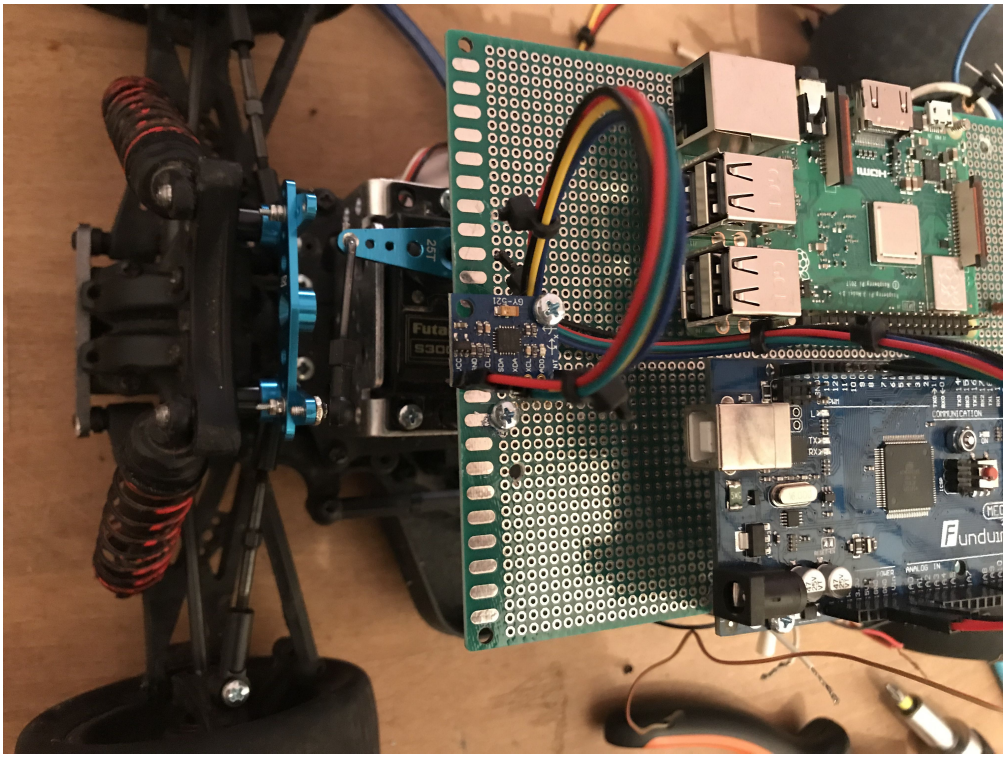

Figure 80: Top view of the CCS mechanism

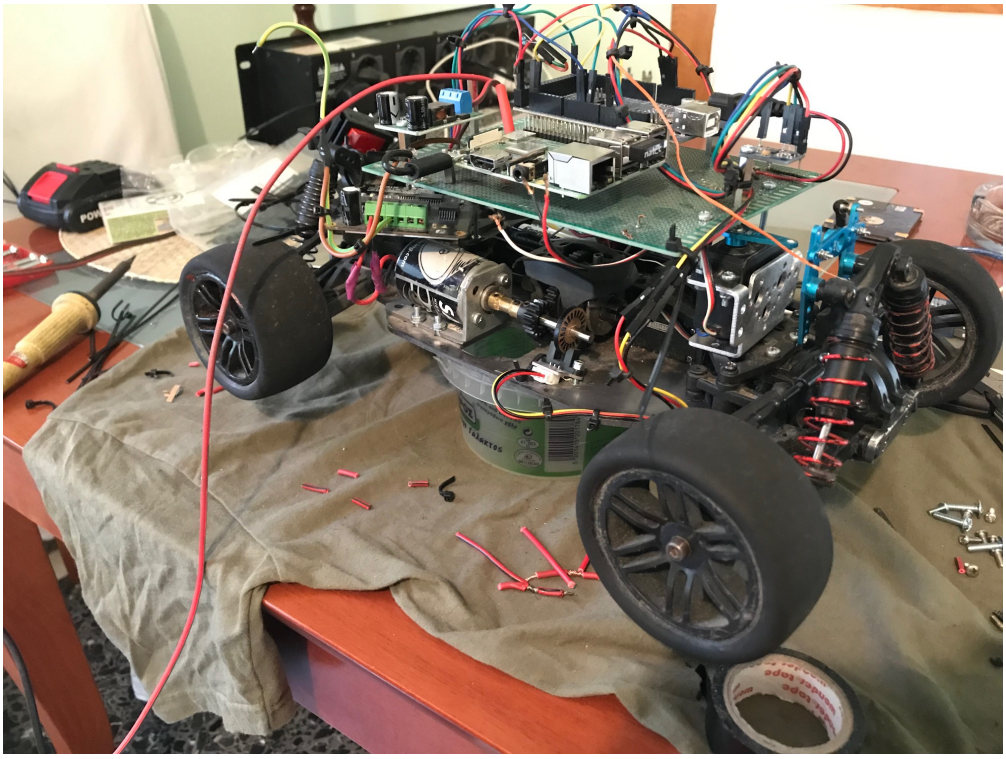

Figure 81: Preparation of the vehicle wiring harness

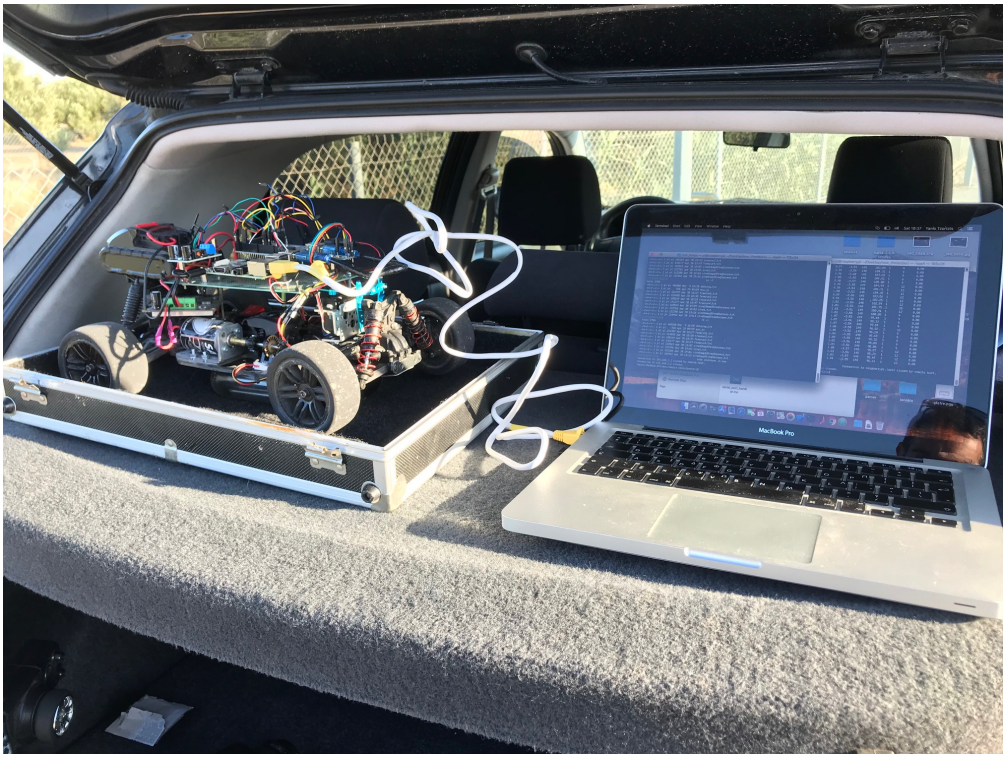

Figure 82: CCS configuration before testing

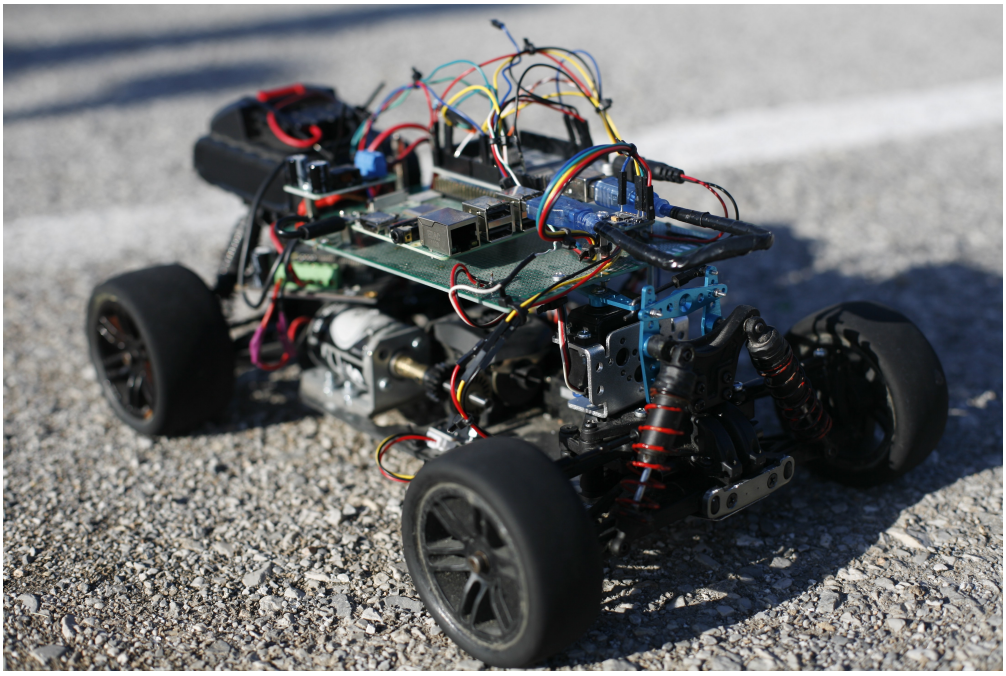

Figure 83: The prototype vehicle before testing